Sheffield Hallam University

A Sheffield Hallam University thesis

REFERENCE

Computer Modelling of Plastic Deformation and Fracture in Heterogeneous Systems.

Gavin Alan Buxton, MSci (Hons.)

A thesis submitted in partial fulfilment of the requirements

of Sheffield Hallam University for the degree of

Doctor of Philosophy

28 November, 2001

Materials Research Institute, Sheffield Hallam University

in collaboration with Rolls Royce Associates..
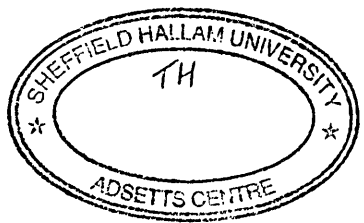
Abstract

The results from a computational investigation of plastic deformation and fracture in austenitic steel are presented. A lattice model representing the continuum mechanical behaviour in three-dimensions is developed. The model is shown to recover the governing equations for continuum elasticity theory and is extended to include plasticity through the localised reduction of elastic moduli, and the application of internal forcces in order to maintain stress continuity. The properties of the bonds constituting the lattice are varied in different regions in order to simulate multi-phase materials. The resulting system of equations retains its linearity and is, therefore, solvable using a conjugate gradient algorithm. Fracture is introduced through the iterative removal of bonds, where clusters of bonds normal to a potential fracture plane are considered.

The model gives reasonable agreement with theoretical predictions for the elastic fields generated by a spherical inclusion, although for small particle sizes the discretisation of the underlying lattice causes some departures from the predicted values. Results are presented for a spherical inclusion in a plastic matrix and are found to be in good agreement with predictions of Wilner [1].

The deformation and fracture of inclusions due to particles characteristically embedded in austenitic steel are considered. The deformation fields within spherical particles are found to depart from uniformity in the presence of plasticity in the matrix, and their decohesion is in accord with experimental expectations. The model accounts for the internal fracture characteristics of elongated manganese sulphide particles when orientated parallel to the tensile direction. The interaction between two iron carbide particles or two voids are also investigated, and found to be potentially detrimental.

Random voidal microstructures are simulated, with subsequent results analysed using Weibull statistical analysis. The maximum stress levels, with respect to the applied stress, are considered and the system size dependence is found to be characteristic of a Weibull distribution. The effects of varying the volume fraction of voids is observed to have a deleterious effect on both the strength and toughness of the simulations.

"...to investigate is to admit prejudice; that nobody has ever really investigated anything, but has always sought positively to prove or disprove something that was conceived of, or suspected, in advance."

Charles Fort.

"The trouble with computers, of course, is that they're very sophisticated idiots."

The Doctor.

Acknowledgements

Contents

Chapter 1

Intoduction.

The deformation and fracture processes within steels are particularly significant because of their importance in assessing the safety and reliability of engineering structures. They are also of academic interest. Material heterogeniety has a direct, and predominantly detrimental, influence on the deformation fields, damage initiation, and eventual failure of load bearing components. In order to elucidate the physics of crack initiation and propagation, in non-dilute heterogeneous systems, numerical methods are required. The principal objective of the research described in this thesis is the development of a quasi-static model of fracture in engineering steels, incorporating plasticity and allowing for interactions between particles, nucleated voids and crack growth.

The failure mechanisms in complex materials are invariably complicated, often involving a variety of processes over a wide range of length and time scales. On

the continuum mechanical length scale, analytical mathematical models are limited to the study of an isolated particle or a single non-propagating crack, often precluding plastic deformation. The investigation of increasingly complicated phenomena is becoming more accessible with computer simulations; i.e. elucidation of the dependence of macroscopic behaviour upon microstructural features, through micro-mechanical modelling.

In this thesis, a model is presented which, subsequent to validation with respect to theoretical and alternative numerical results, is shown to be capable of modelling the effects of constituents upon the deformation fields of an engineering steel. The subsequent damage accumulation is investigated, and the results are found to be consistent with experimental observations, whilst providing unique insights into the fracture mechanisms within engineering steels.

A review of the relevant research work which has been published is considered in chapters 2 and 3. The fracture behaviour of steels, and the influence of constituents, are reviewed in chapter 2, and the computational techniques employed in simulating deformation and fracture are reviewed in chapter3. In particular the use of Lattice Spring Models (LSMs) in the simulation of heterogeneous (generally two-dimensional elastically brittle) materials is surveyed in chapter 3; the development of a three-dimensional model incorporating plasticity and subsequent damage is presented in chapter 4.

The simulation of the inhomogeneity problem is described in chapter 5, where the results are compared to the theoretical analysis of Eshelby [2–4]. The incipient plas-

tic deformation in the matrix surrounding the inhomogeneity is investigated, with the results showing reference to alternative numerical techniques in the literature.

In chapter 6, the model is applied to the simulation of particulate systems, corresponding to an austenitic steel. The deformation and fracture processes associated with single inclusion systems are analysed; systems modelling the interaction between two inclusions are also considered. The micro-mechanical simulation of particulate systems, incorporating plasticity, allow the deleterious effects associated with microscopic constituents to be investigated and the Lattice Spring Model is shown to give results consistent with experimental observations.

In chapter 7, a statistical study is undertaken of the macroscopic response of a material through the direct simulation of underlying random microstructural features. The model appears to exhibit reasonable agreement with the expected theoretical size dependency, and the detrimental consequences of increasing the void volume fraction is observed.

The last chapter draws conclusions from the results presented, and comments on the potential developments that may further improve this avenue of research.

Chapter 2

Literature Review: Experimental.

2.1 Fracture.

Fracture can be defined as the failure of a body by the action of mechanical forces, and may incorporate a wide variety of phenomena. Brittle fracture is characterised by the relatively small amount of energy absorbed prior to rupture, and is associated with little or no preceding plastic deformation. The strength of a brittle material is characterised by its resistance to fracture, and can be quantitatively defined as the critical value of stress at which fracture occurs [5].

Ductile fracture involves the absorption of substantially greater levels of energy (generally involving large plastic deformations), and occurs in three stages: nucleation of internal cavities (often through the fracture of non-metallic inclusions or the decohesion of the inclusion-matrix interface); the growth of these cavities with continued

deformation; and finally their coalescence to produce material rupture [6, 7]. This mechanism is often referred to as fibrous fracture, dimpled rupture or microvoid coalescence, and can occur locally during brittle fracture.

2.1.1 Brittle Fracture.

Brittle fracture is considered to initiate at a stress concentrator, such as a notch or a pre-existing crack; fracture mechanics assumes that these flaws are large in comparison with the characteristic microstructure and therefore the medium is assumed to be a homogeneous continuum [8]. Griffith proposed that a crack will propagate when it is energetically favourable; the elastic energy released by the spreading of the crack in a thin plate, exceeding the surface energy gained by the creation of the crack [9].

In structural materials there are always some inelastic deformations around a crack front that would make the assumption of a linear elastic medium, with infinite stress at the crack tip, questionable, although an additional term may be added to account for dissipative energy at the crack tip. Griffith's criterion is valid if the plastic zone at the crack tip is very small compared with the crack size. It is then reasonable to assume that the energy flowing into the crack tip fracture zone comes from the elastic bulk of the material [8].

McMahon and Cohen [10] established that the cracking of cementite particles, located at ferrite grain boundaries, is a primary initiator of brittle fracture in ferritic

5

steel; although alternative materials may depend upon different statistical factors. As the volume of brittle material considered increases, the probability of finding larger sized flaws (e.g. statistically unfavourable particle distributions) in the structure increases, resulting in lower fracture stresses. Statistically this is often represented through the weakest link theory; the probability of failure in a chain consisting of a number of links, is based upon the proposition that the entire chain fails if any one of its parts fail [11].

The weakest link theory can be described mathematically by considering the probability of a random observation, X, having a value equal to or greater than some value x, being given by

$$P(X \leq x) = c(x) = 1 - \exp\left[-\Phi(x)\right] \tag{2.1}$$

where the function $\Phi(x)$ characterises the form of the distribution. This distribution can be used to describe the probability of failure, or more importantly the size dependency of failure. If P represents the probability of failure of a single link, the probability of nonfailure of a chain of n links, $(1 - P_n)$, is equivalent to the simultaneous nonfailure of all the links, $(1 - P)^n$. Which is given by

$$(1 - P)^n = \exp\left[-n\,\Phi(x)\right] \tag{2.2}$$

Therfore, the probability of failure of n links is of the form

$$P_n = 1 - \exp\left[-n\,\Phi(x)\right] \tag{2.3}$$

The function $\Phi(x)$ must be a positive, nondecreasing function and vanish at a given value, a, which is not necessarily zero; a simple function satisfying these conditions

is

$$\Phi(x) = \left(\frac{x-a}{b}\right)^m \tag{2.4}$$

and thus

$$c(x) = 1 - \exp\left[-n\left(\frac{x-a}{b}\right)^m\right] \tag{2.5}$$

This is the Weibull distribution, where b is the scale parameter, m is the Weibull modulus, a is the location parameter and n is the number of links (volumetric variation). The distribution function has no theoretical basis, but is considered applicable to a number of populations, finding particular popularity in describing the brittle failure of materials. An alternative statistical model, proposed by Ritchie, Knott and Rice [12], identifies significant distances ahead of the crack tip, where critical levels of stress may cause cleavage fracture to occur.

2.1.2 Ductile Fracture.

Ductile fracture in metals invariably involves plastic deformation as a result of the movement of dislocations along the slip planes of the crystalline lattice. Dislocations exist throughout the crystalline lattice in the form of low-density networks. The dislocation density is increased as a result of increasing the plastic straining, impeding further movement of dislocations and raising the effective yield stress [13]. During plastic deformation, voids are nucleated throughout the material; the growth and eventual coalescence of these voids results in material rupture.

The classic dull fibrous appearance in a low-carbon steel specimen can be seen in

7

figure 2.1 [13], which shows the typical 'cup and cone' fracture surface. As the magnification is increased the dimpled rupture appearance is observed, resulting from internal necking of the matrix between decohered carbide particles.
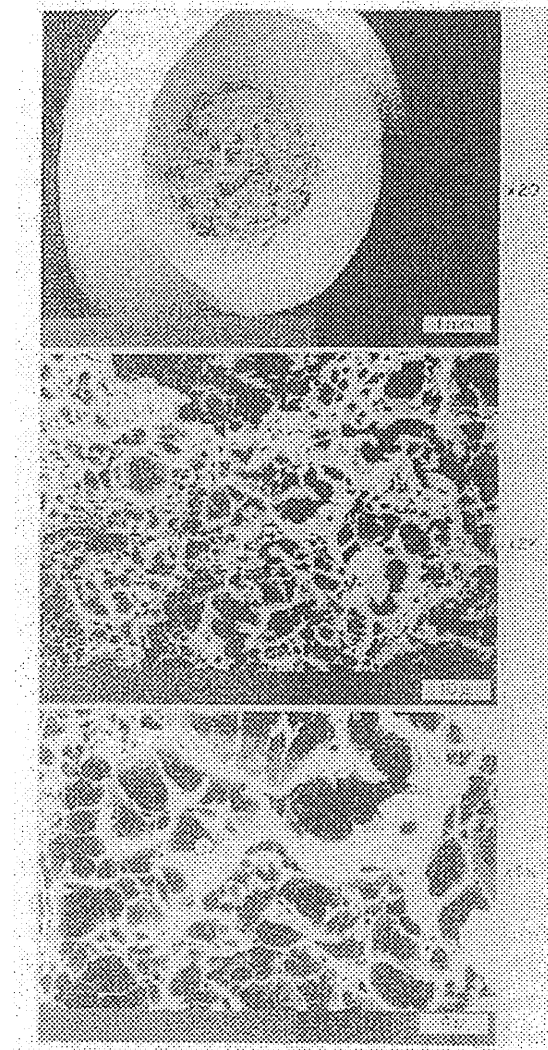
Figure 2.1: Varying magnifications of the ductile fracture surface of a low-carbon steel specimen taken from Thomason [13]. The fractographs (b) and (c) are increased magnifications of the area of fibrous fracture within the rectangular box in (a).

Void nucleation may be initiated at particles, blocked slip bands, grain boundary triple points or boundary irregularities [14], although non-particle related void nucleation is not as prevalent as particle related cavitation [7]. Particles can initiate

damage through interface decohesion or particle fracture; inclusions with large aspect ratios may undergo multiple internal fracturing, whilst spherical inclusions almost always nucleate voids by interfacial separation [15].

Tanaka *et al* [16] proposed a simple criterion for void nucleation by comparing the energy before and after cavitation. It was found that cavitation is energetically favourable at inclusions larger than $0.02 - 0.03\mu m$ (for various materials), almost upon yielding, but for larger particles decohesion occurs at a critical normal stress at the particle/matrix interface [13]. Dislocation loops are emitted from the interface in order to reduce the local shear stresses, resulting from the discontinuity in the elastic properties; reverse pile-ups are responsible for increasing interfacial stresses [17]. Discrete dislocation analysis is required for small particles, although when the dislocation spacing is much smaller than the particle size (generally considered to be diameters greater than a micron in size) continuum analysis of plastic deformation is applicable [13, 15].

Void nucleation is a continuous process with increasing strain; it is generally observed that larger particles decohere or fracture at lower stresses and strains, than smaller particles [6]. Argon *et al* [15] described the detrimental effect of increasing the particle size, even for a constant global volume fraction, resulting from particle interactions in regions of locally increased volume fraction. Cox and Low [18] explained such findings in terms of the variability in fracture strength due to statistically distributed internal flaws.

The second stage of ductile fracture is the growth of voids, be they already present in

9

the material or nucleated at particles. A triaxial stress state accelerates void growth, due to the imposition of surface tractions on the void surface [6]. Stresses normal to the free surfaces of the void must be zero, increasing the maximum shear stresses near the surface of a void and resulting in increased plastic deformation. Increased triaxiality throughout the matrix increases the longitudinal stress required to cause plastic flow, resulting in intense deformation around the voids and enhanced void growth [18]. The continuum analyses of McClintock [19] and Rice and Tracey [20], found an exponential dependence of void growth rate with stress triaxiality, for a long cylindrical void and a spherical void respectively. Experimental verification of theoretical analysis is difficult, due to the impracticalities in measuring the void size as a function of strain [21].

Void coalescence is the final and most difficult stage of ductile fracture to experimentally investigate; void initiation and growth are stable processes, which tend to progress gradually, whereas void coalescence is a catastrophic event which occurs rapidly [22]. There are three basic modes of void coalescence (see figure 2.2), depending upon the stress state within the material; normal rupture, shear rupture and tearing [23]. The dimples on the fracture surfaces are either circular (normal), elongated in opposite directions (shear), or elongated in the same direction (tearing); tearing is most likely to occur in a notched specimen.

The plastic strain is a maximum at an angle of 45° with the prospective crack plane, and voids are nucleated in areas of high plastic strain. Ductile fracture therefore propagates along alternative shear planes, through microvoid coalescence, following
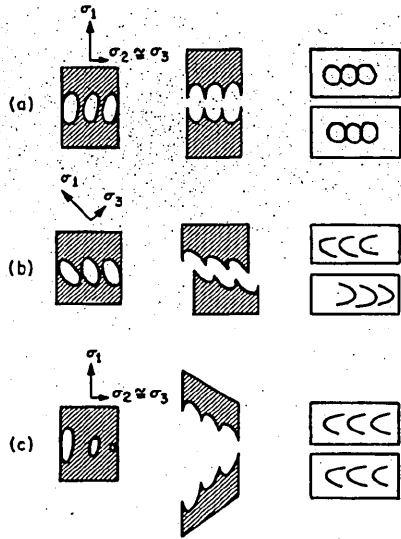
Figure 2.2: The three basic modes for the coalescence of voids, depicting the material stressed almost to rupture (right), local rupture (centre), and the directional sense of dimples on the rupture surface, taken from Beachem [23]. The modes are a) normal rupture, b) shear rupture, and c) tearing.

a zigzag course in a continuous manner. This phenomena produces periodic ridges and valleys, on what is an otherwise, macroscopically flat fracture surface [24]. This is especially the case in materials exhibiting low strain-hardening and high yield stress [25] and two-dimensional problems [26].

2.2 Steel and Associated Constituent Properties.

2.2.1 Introduction.

Steel is a generic term for materials with a large range of complex compositions, but is essentially an alloy of iron and carbon containing up to roughly 2.0% carbon. As the carbon content of a steel increases so does its hardness; iron carbide, a hard substance, is precipitated from the steel upon cooling due to the difference in its

solubility in high temperature FCC (2.0% C) and low temperature BCC (0.02% C) iron phases. The carbon content of ferrite (Fe and less than 0.02% C) can greatly influence the mechanical properties by opposing the movement of dislocations [27]. Other elements can be added (i.e. nickel, chromium and molybdenum) to the steel in order to vary the mechanical properties further or introduce new properties (such as corrosion resistance), although the microstructure exerts an appreciable influence, especially the presence of second-phase particulates.

2.2.2   Particles.

Steels may contain a large variety of particles, such as carbides, sulphides and oxides. The detrimental effect of particle volume fraction in copper is shown in figure 2.3 [13], although other factors such as shape, orientation with repect to the tensile direction, and interfacial strength, can be influential [7]. Larger particles may be in a damaged state (partial debonding or internal cracking) subsequent to production processes [13].

Differential thermal contraction between particulates and matrix can result in tesselated stresses, as the steel is cooled to operational temperatures. Brooksbank [28] investigated the detrimental effects of particulates, with lower expansion coefficients than the matrix, upon steel and found that alumina particles are the most deleterious; aluminates and titanium nitride particles are also damaging, whilst oxides were found to exert a negligible effect. Manganese sulphides are unusual in having a greater expansion coefficient than the steel matrix, and therefore voids may be
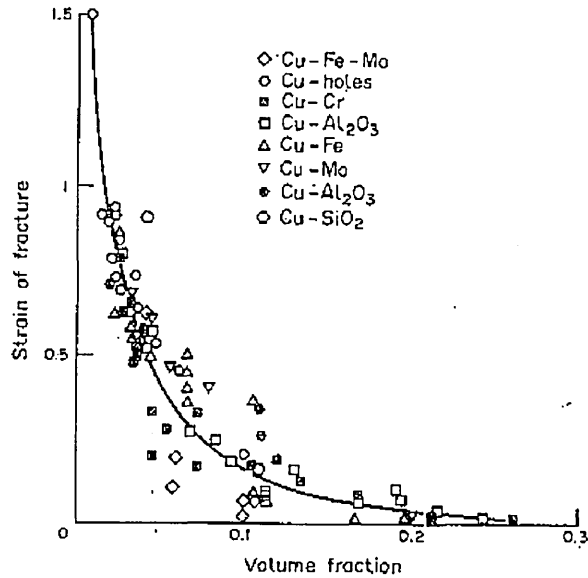
Figure 2.3: The detrimental effect of particle, or void, volume fraction in copper on the true tensile strain at fracture; taken from Thomason [13].

created around such inclusions. Equilibrium occurs at high temperatures during processing, and therefore the MnS particle is expected to shrink to a greater extent than the steel matrix upon cooling to operational temperatures. That said, for a particulate system to be susceptible to such an effect, the interfacial strength would have to be particularly weak [22].

Iron carbide particles (Fe_3C) are a source of fracture, either through internal fracture of the particle or interfacial decohesion. Internal fracture is favoured in the lower shelf region, and in high strength and low toughness steels [10], where larger particles are also more likely to fracture [6]. The elastic properties of iron carbide particles are $E = 268GPa$ (Young's modulus) and $\nu = 0.3$ (Poisson's ratio) [14]. Jun et al [29] calculated the fracture strength of spherical carbide particles in steel, based on an

energy balance condition, to be 2027 MPa. Jun [30] has also estimated the interfacial decohesion strength to be 1024 MPa, although other authors have obtained values varying between 950 and 1800 MPa [31].

Manganese sulphides (MnS) are one of the most common sources for void nucleation in low-alloy steels [6]. During the process of hot rolling, MnS in steel can be elongated by plastic deformation [32]. Longitudinal (to working) tensile specimens are more likely to fail by cracking across the particle perpendicular to the tensile direction, whilst transverse tensile specimens have a propensity to decohere from the matrix [33]. The toughness and ductility are greater in the direction of working than in the direction transverse to working; therefore particles aligned perpendicular to the tensile axis are considered more detrimental [22]. The aspect ratio can vary greatly [33], but the particles are generally several tens of microns long and several microns in the other dimensions [34].

The Young's modulus of MnS is 137 GPa [35], but plastic deformation has been observed; the slip planes in the ferrite alter direction to coincide with the slip planes in the inclusion, indicating the greater ability for dislocations to cross-glide in metals than in ionic solids, as can be seen in figure 2.4 [32]. It is this limit in the particles ductility which allows internal particle fracture to occur when the particles are orientated in the tensile direction. The ferrite-MnS interface is generally considered weak, although this is not necesarily the case [36]. Beremin *et al* [37] estimated the interfacial strength, in the transverse direction, to be 810 +/- 50 MPa and the fracture strength, in the longitudinal direction, to be 1120 +/- 60 MPa. This was
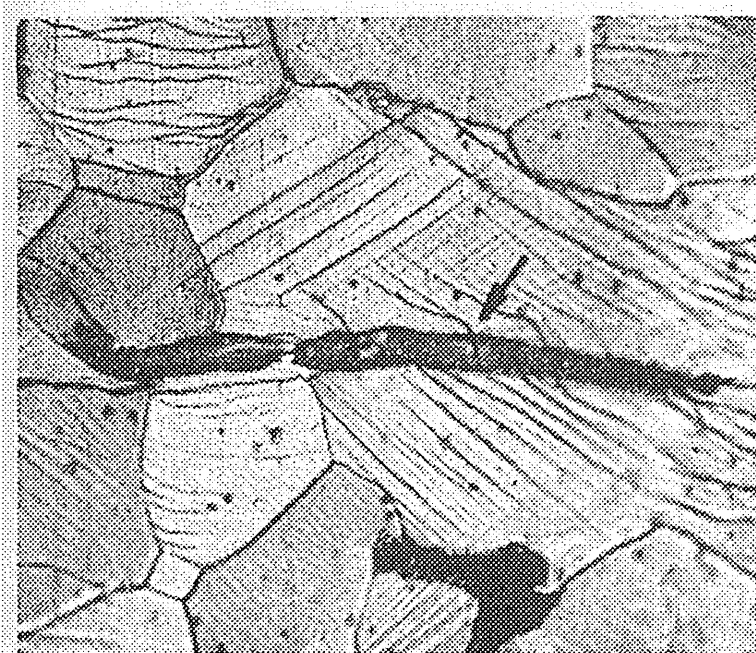
Figure 2.4: Slip on the external surface of a steel containing a MnS particle, taken from Wood and Van Vlack [32]. Slip occured in both the ferrite and MnS phases, although the greater ductility of the ferrite is exhibited through the redirection of slip planes to coincide with the slip planes in the MnS particle. The coherent slip, between the matrix and particle, is indicated by the arrow and the dark region in the centre of the figure is the MnS particle.

calculated through the application of an elastic analytical theory to a plastically deforming matrix, identifying plastic equivalent elastic constants, and is therefore dubious.

2.2.3 Void Sheet Coalescence.

In a material consisting of a dual population of particulates, a primary population (such as MnS) and a secondary population (such as Fe_3C), void sheet coalescence may occur [18]. The primary population has the controlling influence on the conditions for incipient ductile fracture. As the voids initiated at the primary particles

grow, localised internal necking between these voids will produce bands of intense additional plastic strain impinging on the secondary population of particles. Coalescence will subsequently occur by secondary void formation in these bands [6]. Both these bands and, ultimately, the fracture path develop at 45° to the tensile direction [18]. A typical void sheet coalescence fracture surface, taken from Cox
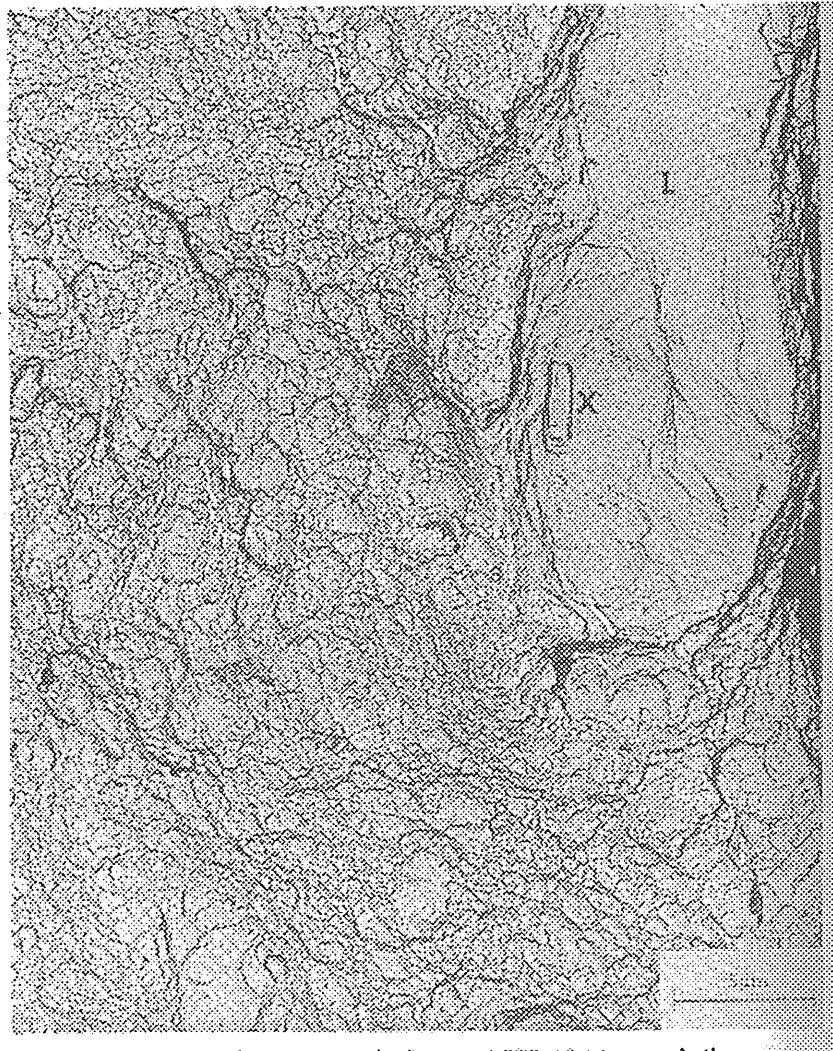
Figure 2.5: Electron fractograph from AISI4340 steel, taken from [18]: large dimple indicated by L, nucleating MnS particle indicated by X.

and Low [18], is shown in figure 2.5. This depicts a large dimple, resulting from the decohesion of a MnS particle, and the subsequent void growth. Smaller dimples,

16

produced during the coalescence of larger voids, are a consequence of the ductile

fracture of surrounding regions, which are populated with Fe_3C particles.

Chapter 3

Literature Review: Numerical Modelling.

3.1 Introduction.

Computer simulations are a valuable technique for elucidating the fundamental physics associated with deformation and fracture processes, and revealing insights which cannot be obtained from experimentation. Computational modelling enables the variation of constituent properties to be investigated, without the arduous task of additional materials specification and production. The length scales over which fracture processes are discerned varies from the atomistic to the continuum, and the choice of model reflects the phenomena studied.

The investigation of fracture in steels, and many other materials, requires an under-

standing of the micromechanical response of heterogeneous systems. Macroscopic deformation and fracture properties can be related to the materials microstructural features (e.g. grain size, second phase particle characteristics and volume fraction), and homogenised characteristics of the heterogeneous material can be obtained and subsequently applied in continuum models. Alternatively, micromechanical simulations can ascertain the spatio-cooperative dependence of microcracking in heterogeneous materials upon local strength and toughness variations.

In this chapter a brief review of models addressing the simulation of fracture is presented. The fundamental fracture process is initiated at the atomic level, and a review of such techniques is given. Micromechanical modelling is usually achieved through the application of continuum based theories to the simulation of microstructural phenomena, and a review of models incorporating this approach is also presented, including a review of Eshelby's inhomogeneity problem, Finite Element Methods and Lattice Spring Models.

3.2   Atomistic simulations of fracture.

Atomistic simulations predict the behaviour of a given number of atoms, governed by their mutual interactions, where either the atomic motion is simulated, or the equilibrium atomic configuration is obtained as a function of applied stress. Atomistic simulations are defined by the interactive nature of the atomic structure; either ab-initio electronic-structure calculations or classical inter-particle potentials. Ab-initio

calculations provide a quantum mechanical description of the atomic interaction, allowing for strongly environment-dependent characteristics [38]. A less computationally demanding quantum mechanical representation can be achieved through tight-binding formulations (a semi-empirical electronic structure description of matter) [39], although in fracture simulations empirical interaction potentials are more common.

Systems governed by empirical interaction potentials are computationally less expensive than those employing quantum mechanical methods. If only pairwise interactive potentials are assumed, the energy of a collection of atoms can be written in the form,

$$E = \frac{1}{2} \sum_{ij} U_{ij}(\mathbf{r}_{ij}) \qquad (3.1)$$

were U_{ij} describes the dependence of the interaction energy between the atom pair i and j, upon the relative displacement vector $\mathbf{r}_{ij}$. The simplest pairwise potential is harmonic in nature, producing linear force interactions [40], although many others exist. The Lennard-Jones 12:6 potential, originally derived for the Van der Waals interactions of an inert gas [41], is widely used for atomic systems in computational physics, possessing an interaction potential of the form

$$U_{ij}(\mathbf{r}_{ij}) = \epsilon_o \left[\left(\frac{d}{\mathbf{r}_{ij}} \right)^{12} - 2 \left(\frac{d}{\mathbf{r}_{ij}} \right)^6 \right] \qquad (3.2)$$

where d is the equilibrium inter-atomic spacing and ϵ_0 is the energy well depth.

Reasonable results have been obtained, in condense matter physics, using pairwise potentials, the resultant elastic constants satisfying the Cauchy relations [42] (assuming every atom occupies a centre of symmetry). Since there is a Cauchy discrepancy

in some materials, such potentials present an elastic deficiency [43]. Attempts to rectify this problem lead to many-body potentials being considered, such as a volume dependent term [44]. Arbitrary many-body potentials, may lead to ambiguities when considering fracture surfaces; e.g. volume is indefinable. A more physically meaningful potential includes an additional term, $F(\rho_i)$, defined as the energy required to place a particle i in an electron gas of density ρ_i, in conjunction with the usual pair potential [45, 46]

$$E = \sum_i F(\rho_i) + \frac{1}{2} \sum_{ij} U_{ij}(\mathbf{r}_{ij}) \qquad (3.3)$$

This is defined as the Embedded Atom Method (EAM), and has been modified to include additional angular terms [47]. It should be noted that whilst empirical interatomic potentials are fitted to bulk properties (and reproduce those properties well), the atomic coordination at the crack tip differs substantially from the bulk environment, and therefore the applicability of empirical interatomic potentials to the simulation of fracture is questionable.

Atomistic simulations are computationally expensive, but in order to increase the simulation scope the crack tip may be modelled using a different approach from those used in the bulk. A quantum mechanical description of the crack tip is thought to be necessary fully to capture the bond breaking phenomena, and the subsequent reconstructions of the internal surfaces of the crack [48]. Therefore simulations consisting of a crack tip described by either ab initio calculations or tight-binding formulations, an intermediate outer shell described using empirical interatomic potentials and an outermost region of linear elasticity are becoming increasingly popular [48–50].

The competition between dislocation generation and crack advancement [51], lattice trapping phenomena [48] and rapid brittle fracture [49] are computationally accessible problems with atomistic simulations, but the micromechanical length scales of interest in this study are intractable.

3.3 Inhomogeneity problem.

The microstructural constituents of interest, within the present study, are second-phase particles and nucleated voids. Eshelby [2–4] modelled inclusions by deriving an analytical method for calculating the perturbations in an elastic medium when a region within it underwent a change in form (transformation field), which would be uniform if the surrounding material were absent. This is known as the transformation problem, and solutions for the elastic field both in the matrix and in the inclusion were obtained. The inhomogeneity problem is mathematically identical and was studied for an isolated ellipsoidal inhomogeneity (a region of differing elastic constants) is embedded in an infinite isotropic elastic solid. Incorporation of plastic flow, through the application of a uniform plastic stress-free transformation strain, has been attempted [52]; such approaches incorrectly assume a uniform elastic field within the particle. In order correctly to extend Eshelby's analytical work to include plastic deformation an integral equation approach has been adopted, requiring an iterative solution [53,54]. The integral equation approach assumes a uniform elastic stress field at infinity and is, therefore, only applicable to dilute heterogeneous systems were there is negligible particulate interaction; assuming elastic deformation at

infinity, limits the analysis to the incipient stages of plastic development. An elastic spherical inclusion in an infinite elastic-plastic matrix was investigated by Wilner [1] using a variational method. Wilner established a general solution for axisymmetric deformation of elastic prolate spheroidal regions. This solution is then employed to represent the field within the particle as well as to suggest the form of a trial field to be used in the elastic-plastic matrix. For a given trial field in the exterior domain, the displacements on the boundary of the inclusion can be determined and corresponding (exact) field within the particle can be evaluated from the general solution. In this way the accuracy of the numerical scheme is dependent only upon the trial field within the matrix, and since the representation for the solution within the matrix is complete and contains as a special case the solution for an elastic matrix, an accurate solution to the boundary value problem can be achieved In order to investigate complex phenomena, more complicated computational methods are required.

Comparisons between the analytical results of Eshelby and results obtained from LSM simulations are made in chapter 5, and therefore a review of Eshelby's inhomogeneity problem and the necessary formulae for obtaining the elastic fields due to the deformation of a system containing a spherical inhomogeneity are now summarised.

In the present notation repeated suffixes are to be repeated over axes x, y, z and suffices following a comma denote differentiation with respect to the cartesian coordinates. It is convenient to use $f = f_{ii}$ and $f'_{ij} = f_{ij} - \frac{1}{3}f_{kk}\delta ij$, to denote the scalar

and deviatoric components of the second order tensors in the following analysis. In this way, the components of the transformation strain field (u^T) can be related to the applied far field strain (u^A) using

$$u^T = Au^A \qquad u'^T_{ij} = Bu'^A_{ij} \qquad (3.4)$$

where the values of A and B are given by the relations

$$A = \frac{K_p - K_m}{(K_m - K_p)\alpha - K_m} \qquad B = \frac{\mu_p - \mu_m}{(\mu_m - \mu_p)\beta - \mu_m} \qquad (3.5)$$

The subscripts p and m denote paticle and matrix characteristics respectively, and K and μ are the bulk and shear modulus respectively. The constants α and β are defined in terms of the Poisson's ratio of the matrix

$$\alpha = \frac{1}{3}\frac{1 + \nu_m}{1 - \nu_m} \qquad \beta = \frac{2}{15}\frac{4 - 5\nu_m}{1 - \nu_m} \qquad (3.6)$$

The external constraint displacement field can now be derived in terms of the transformation strain field using the expression

$$u_i^C = \frac{u_{jk}^T \Psi_{,ijk}}{8\pi(1 - \nu_p)} - \frac{u_{ik}^T \Phi_{,k}}{2\pi} - \frac{\nu_p u^T \Phi_{,i}}{4\pi(1 - \nu_p)} \qquad (3.7)$$

where Φ is the harmonic potential and Ψ is the biharmonic potential. In the case of a sphere, of radius a, these are given in terms of the distance from the centre of the inclusion r by

$$\Phi = \frac{4}{3}\pi\frac{a^3}{r} \qquad \Psi = \frac{4}{3}\pi a^4\left(\frac{a}{5r} + \frac{r}{a}\right) \qquad (3.8)$$

The external constraint field can therefore be obtained from the standard definition of the strain tensor. The internal constraint field is constant, due to the uniform applied field and can be obtained directly from the transformation field

$$u^C = \alpha u^T \qquad u'^C_{ij} = \beta u'^T_{ij} \qquad (3.9)$$

24

The strain field throughout the system is of the form, $u_{ij} = u_{ij}^A + u_{ij}^C$; the stress tensor can further be derived form the strain tensor using the standard relation.

3.4 Finite Element Method.

The Finite Element Method (FEM) is the dominant continuum discretisation technique employed in micromechanical modelling; the displacement field over the entire body is replaced by a collection of elements with individual displacement fields of reduced complexity. The elements throughout the model are connected at nodes, each of which possessing the necessary degrees of freedom, in terms of which the constitutive response of each element is expressed. The system is subject to appropriate boundary conditions and the resultant equations of equilibrium solved.

3.4.1 Particles.

FEM micromechanical simulations generally employ unit cell methodology or an axisymmetric approach; these models possess translational and reflective symmetry respectively. Utilising both unit cell and axisymmetric systems, Christman et al [55] and Llorca et al [56] have investigated SiC ceramic whisker- and particle-reinforced aluminium composites. The effect of clustering was addressed through the systematic displacement of reinforcement position from the uniformly distributed configuration in axisymmetric simulations. Llorca et al simulated damage initiation, although due to the nature of the boundary conditions, the particulate distribution

and initiated damage were translationally repeated in an infinite array.

Hom and McMeeking [57] employed a unit cell simulation of a cubic array of rigid spheres in a elastic-perfect plastic matrix (no hardening), but acknowledged that the simulation was unrealistic as real particles are not spherical, of uniform size, or regularly arranged.

Xu et al [58] simulated the deformation of an array of particles in a plastically deforming matrix, using an axisymmetric FEM formulation. The stress gathering capability of the particle (defined as the ratio of the axial stress within the particle to the far field value) was initially reduced at the onset of plastic deformation due to localised plastic relaxation around the particle. Subsequent to strain hardening effects, the overall response of the matrix becomes more pliant, resulting in large stress concentrations and increasing the stress gathering capability.

The stress field associated with cubic particles was found by Watt et al [59] to be higher than that for spherical particles. Similarly to the approach of Llorca et al [56], the particles were displaced towards axisymetric boundaries in order to investigate clustering effects.

A regular distribution of three clustered particles in an infinite system was modelled using an axisymetric system by Thomson et al [60]. A repeated pattern of particles allowed clustering effects to be considered, whilst particle decohesion was accounted for through the use of a traction-separation relation similar to Needleman [61]. Simulations addressing significantly larger collections of particles were

performed by Gusev et al [62], in which a periodic elastic system, containing up to sixty four spherical particles, was used to calculate the overall elastic constants. Recently a similar multi-particle system has been considered by Böhm [63], inwhich systems containing twenty particles where deformed ($\approx 1\%$ strain) and the matrix exhibited plasticity.

The inherent anisotropy of three-dimensional unit cells, and the inability to address large scale fracture, limits the applicability of such models in simulating the stress transfer and damage accumulation in heterogeneous systems. The number of particles that can be simulated is limited by the computational expense of the FEM technique, and so simulation sizes of the order of representative volume elements are currently unobtainable in damaged systems or systems exhibiting plasticity [63].

3.4.2   Fracture.

The element elimination technique is a prevalent method in the simulation of fracture in FEMs; the stress carrying capability of an element is removed as a consequence of fulfilling the adopted failure criteria [64]. Element removal confines the fracture zone size to that of the FE grid.

A large number of fracture criteria exist, such as the criticality of plastic strain, Von Mises stress, hydrostatic stress, stress triaxiality, and various combinations of these parameters [65]. Gurson [66] and later Tvergaard et al [67] developed a widely used constitutive relation for dilatent plasticity which describes ductile void growth

27

within a confined cell, exhibiting the resultant reduction in stiffness and its eventual inability to carry stress. Considering each element to contain a single void, the effects of ductile fracture were accounted for [68], but clustering effects were ignored.

Computational damage mechanics and the local approach to fracture take into consideration material damage through stiffness degradation [69]. Here, the voids and micro-cracks are considered homogenised with respect to the size of the element, and the nature of the damage which causes the reduction in stiffness is disregarded. Investigation of stable crack growth prior to unstable cleavage has been achieved through the coupling of Weibull statistics and a model derived from the Gurson-Tvergaard potential [70]. In this approach the probability of an element failing is made to depend upon the competition between two criteria; it proved possible to tune these to yield the desired macroscopic effects.

The choice of fracture criteria appears to be a matter of predilection or of trial and error; crack growth cannot be explained purely in terms of averaged quantities and an understanding of the fracture process must be based on the relationship between material damage and inhomogeneities.

Ghosh et al [71] developed the concept of hybrid finite elements which represent basic structural elements which contain one second phase constituent, either a particle or a void; the particle is considered either to crack completely or debond instantaneously as crack propagation within a particle is unobtainable.

The ductile process from initial debonding to complete separation and subsequent

void growth has been simulated using a cohesive zone model by Needleman [61]. Hence the interface is assigned an independent constitutive relation which, for increasing interfacial separation, requires a tractive force to go through a maximum value before diminishing to zero, allowing debonding to be incorporated.

One of the major limitations to FEM simulations of fracture is the mesh modification which is thought to be necessary in modelling crack propagation. The use of multi-phase elements can alleviate the need for mesh regeneration. In this approach, different phase properties are assigned to different integration points in the elements, removing the mesh dependence of phase boundaries [64]. The sharp transition in phase properties at element boundaries is however substituted with steep gradients between integration points, resulting in a loss of geometrical definition [65].

3.5   Lattice Spring Models.

This section reviews lattice spring models; a method of discretising continuum elastic media in the simulation of deformation and fracture. A lattice spring model consists of a two-dimensional or three-dimensional network of mathematical interactive elements, which can be either one-dimensional springs or solid beams. Gradual changes in the boundary conditions, such as the incremental application of uniform stress or strain fields, drive the system. Through the localised variation of elastic properties for different elements, the effects of microstructural defects and features can be studied. Lattice spring models are particularly useful for elucidating the

physics of stress transfer and stress field redistribution in systems, incorporating inhomogeneities and damage accumulation, the latter being simulated through element removal. Subsequent to crack evolution (removal of an element) the system is relaxed to its minimum energy configuration, allowing stress redistribution from a removed element to the remaining bonds in the system, and the criterion for further element removal is re-applied. Due to the re-equilibriation of the system during crack propagation, these models are inclined towards the simulation of quasi-static fracture; although some workers have studied the dynamics of fracture [72].

3.5.1 Lattice Models of Elasticity.

Lattice models of elasticity were first conceived as a structural engineering technique for use in understanding systems unsolvable using pure mathematical analysis [73]; computational capabilities have recently allowed systems of increasing size and complexity to be simulated. The different formulations of lattice spring models can be categorised by the kind of Hamiltonian associated with nodal interactions.

Scalar models can be viewed as an electrical equivalent, and are often referred to as fuse network models [74,75]. The equations of equilibrium are similiar to mechanical laws of elasticity, except that they are scalar as opposed to vectorial, the system being solved as a set of equations similiar to Kirchoff's law (where one-dimensional force is comparable to current, one-dimensional displacement to voltage and stiffness to conductance) [76,77]. Such systems have been used extensively in the study of avalanche phenomena and scaling laws in fracture [78–80]. Conceptually and nu-

merically such systems are simpler to implement than other lattice spring networks, but due to the scalar nature of these systems, the Poisson's ratio is fixed at zero. These models may be of interest, per se, to statistical physicists, but they are of limited application in the study of real materials and therefore of limited value to material scientists.

Hookean spring models are networks of springs which obey Hookes law. In order to achieve elastic isotropy (and a Poisson's ratio greater than zero), triangular networks of nearest neighbour interactions or square networks of both nearest and next-nearest neighbour interactions are usually considered [81–85]. The Hamiltonian for such a system consists of central force interactions, and is rotationally invariant [86],

$$H = \frac{1}{2} \sum_{ij} k_{ij} [(\mathbf{u}_i - \mathbf{u}_j) \cdot \hat{\mathbf{r}}_{ij}]^2 \qquad (3.10)$$

in which k_{ij} is the central force constant between nodes i and j, $\mathbf{u}_i$ is the vectorial displacement of node i, and $\hat{\mathbf{r}}_{ij}$ is the unit vector connecting nodes i and j. The Poisson's ratio obtained in such systems is generally limited by the geometry (typically its value is a third in two-dimensional systems and a quarter in three-dimensional systems), although it can be varied in two-dimensional systems through the construction of a triangular lattice from the superimposition of three hexagonal (and isotropic) lattices [87,88]. In such systems the Poisson's ratio can be varied between a third and one, although the effect this has on localised stresses in heterogeneous systems is unknown.

Hookean spring models have been used to investigate diluted systems [83,89], particulate composites [88,90], and recently a three-dimensional Hookean spring model

31

has found applicability in the simulation of human trabecular bone [91,92]. Despite this utility, Hookean spring models are incapable of possessing a varying Poisson's ratio in three-dimensions, and simulations involving triangular systems have led to spurious fracture characteristics [89]. The latter is a result of bonds parallel to the applied force being initially removed and the remaining bonds along the crack path undergoing artificial shearing in order to align with the applied force [93]; rotation of bonds in a Hookean spring model are not energetically penalised in any way.

In order to penalise the free rotation of bonds from their initial orientation a Born spring model can be employed [82,94]; this is a macroscopic equivalent of the Born-Huang model for microscopic elasticity [42]. The Hamiltonian takes into consideration the lack of rotational freedom through the introduction of a non-central force constant, c_{ij}, between nodes i and j [95],

$$H = \frac{1}{2}\sum_{ij}(k_{ij} - c_{ij})[(\mathbf{u}_i - \mathbf{u}_j) \cdot \hat{\mathbf{r}}_{ij}]^2 + \frac{1}{2}\sum_{ij}c_{ij}(\mathbf{u}_i - \mathbf{u}_j)^2. \qquad (3.11)$$

Rotation of this system from the networks original orientation results in a restoring force, although the configuration is otherwise unchanged. This lack of rotational invariance is considered negligable for small displacements [82], for which this model can be shown to be equivalent to the mathematical theory of an isotropic elastic continuum [96]. This model allows reasonable crack morphology to be obtained [82] and has been used to investigate two-dimensional and three-dimensional fracture surfaces [97,98].

An alternative to the Born model, which also employs a non-central force constant, is the Kirkwood-Keating spring model. Keating proposed an alternative to the Born

model of atomic interaction, to avoid the anomolous dependence of the bulk modulus on the non-central force constant; under hydrostatic pressure only the interatomic distances should change, all angles remain constant [99]. Kirkwood had earlier introduced an angular term into the Hamiltonian for a chain segment of N atoms,

$$H = \frac{k}{2}\sum_{n=2}^{N}(\Delta r_n)^2 + \frac{ca^2}{2}\sum_{n=2}^{N-1}(\Delta \alpha_n)^2 \tag{3.12}$$

where Δr_n is the extension of a chain segment, and $\Delta \alpha_n$ is the variation in the angle (therefore introducing a three-body term) between two chain segments from the initial equilibrium configuration [100]. A number of lattice spring models have utilised this hamiltonian [101–103]. The three-body term accounting for the angular variation, is often written as the deviation of the cosine of the angle from equilibrium [93, 104, 105],

$$H = \frac{k}{2}\sum_{ij}(\mathbf{r}_{ij} - \mathbf{r}_o)^2 + \frac{c}{2}\sum_{ijk}(cos\theta_{ijk} - cos\theta_o)^2. \tag{3.13}$$

The natural extension of this model to three dimensions can be achieved in a number of different ways; Arbabi et al [106, 107] maintained a similiar Hamiltonian to that employed by Kirkwood, whilst Chen et al [108] adopted a more computationally expensive hamiltonian which involved a four-body interaction corresponding to torsion angles in the system. It is also not clear if the nonlinearity introduced through the angular terms, when linearised for subsequent solution, offer any advantage over the Born model. The Kirkwood-Keating formulation is rotationally invariant and therefore preferred, but perhaps the implementation is more equivalent to the iterative rotation of equilibrium orientation in a Born model, in which case the additional computational expense is unwarranted.

Elasticity can also be simulated through beam models, consisting of nodes connected by solid structural elements which can incorporate normal and shearing forces [109, 110]. This requires each node to possess three degrees of freedom in two dimensions (two displacement and one rotational), and six degrees of freedom in three dimensions (three displacement and three rotational). The forces and moments within the system arise through the interactions between these parameters. Investigation of fracture in concrete structures have led to good comparisons with experimental data [111, 112].

A variety of beam models which include random geometry, known as rigid-body-spring networks, partition the system into an assembly of rigid convex polygons connected along their boundaries through discrete springs positioned midway along each segment. In a regular square lattice this is equivalent to a standard beam model [113]. Such models are capable of combining the ability to model a uniform strain field (unabtainable with general random geometry beam models), and be isotropic with respect to potential cracking directions (problematic in regular lattices) [113, 114].

In order to simulate the fracture of thin layers of a material supported by a substrate, surface cracking models have emerged, consisting of two-dimensional lattice spring models with appropriate boundary conditions. These boundary conditions involve elastic connections with either fixed points [115] (rigid substrates) or points which are displaced [116] (deformable substrates). Such models are ideally suited to the studies of such systems as thin films of paint on varying surfaces, desicated fracture

and layers of rock in the earth's crust [117]. In systems where short range correlations are dominant, a minimal fracture model has emerged where non-broken nearest neighbour bonds of the just removed bond are damaged [118]. It is assumed that local friction between the surface and the substrate is the only source of stress and that the surface is incapable of long range stress relaxation; therefore the system does not require driving boundary conditions or system re-equilibriation.

3.5.2 Damage Accumulation.

In order to simulate fracture in lattice spring models bonds are removed and therefore a criterion for removing bonds must be conceived. In scalar models the criterion is invariably a critical force, or current, within a bond which dictates its removal; in other models such deterministic criticality is also common. The given elastic state of a bond induces breakage through either critical strain [83], stress [82], or energy [102]. It has been argued that an energy criterion is advantageous due to its generality, allowing contributions from both tensile and shear deformation [93].

At each iteration, prior to minimisation of the system to its lowest energy configuration, either a single bond or multiple bonds can be removed [82]; the latter implying that the fracture process can occur in short enough bursts that stress relaxation has not transpired. The distinction between breaking a single bond or multiple bonds is the size of the meso-scopic portion that is removed prior to stress relaxation in the material, and must have direct implications on the discretised quasi-static nature of the model. It has also been observed that large steps in the driving boundary

conditions can result in too many bonds breaking in a given iteration, obscuring crack formation and propagation [108].

Jagota [119] envisioned separate energy criteria for bond removal, depending on whether such removal was contributing to crack tip propagation, or constituted the nucleation of an isolated crack. Dual breaking criteria seem physically unrealistic, but using the same criteria for all areas of the simulation was reported to lead to very low values of critical nucleation stresses. It was observed, in simulations containing a single breaking criterion, that fracture was biased away from the crack tip when heterogeneities were present; it is not stated why such behaviour is considered unreasonable. The identification of 'crack tip' bonds is problematic as bonds in the wake of a crack, adjacent to a void or constituting a blunt crack are indeterminate. Despite this, it is argued in [119] that in order to properly establish both fracture toughness and nucleation criteria there is no alternative.

The removal of bonds can be considered as a random process, often employing a kinetic rupture criterion based on the absolute reaction rate theory of Eyring [115, 120, 121]. Considering bond failure as a chemical process, the rate of chemical reactions can be extended to material breakdown, and the average time required for this failure to occur can be obtained [122, 123], therefore introducing chronology into the system (quantitative agreement with real system is either fortuitous or is a result of tuning the simulation parameters [115]) . The use of stochastic breaking criteria can lead to substantial damage being sustained in the material, prior to a major crack occurring.

The bonds in the system are meso-scopic representations of the material, and can therefore be considered as damaged prior to failure. The gradual accumulation of damage is assumed to occur over a number of iterations, until the damage associated with an element reaches a threshold value [115]; this may be accompanied by a reduction in the elastic moduli of the elements [124].

3.5.3 Randomisation.

In a regular lattice devoid of randomisation the fracture path is dictated, not exclusively by the direction of applied stress, but also by the geometry of the lattice used by the spring network [93]; in a triangular lattice the crack propagates at a direction which is not perpendicular to the tensile direction [89, 119]. It is this anisotropy, present in the regularly discretised lattice, which necessitates the need for randomisation in the system. It is also, as a consequence of quenched disorder in real materials, that randomisation may be desirable in simulations.

Isotropy, with respect to potential fracture paths, can be obtained through the replacement of a regular lattice with an orientationally randomised lattice. This can be achieved through randomly displacing the original positions of the nodes prior to simulation [119]; application of random internal force at nodal sites will have a similiar effect [76]. Random lattices can also be obtained through the use of Voronoi diagrams [110], or grown by adding flexible fibres onto a growing deposit [125].

A simpler method of introducing randomisation into lattice spring models is through

37

the distribution of elastic moduli or failure thresholds [84]. The randomisation of elastic moduli results in localised deviations from isotropic behaviour, which can result in stress concentrations in directions away from the geometrically preferred potential crack path. Failure thresholds can be assigned through Weibull, normal or power-law distributions (no distinction between the exact statistical distribution and global behaviour is apparent [79, 116]) which potentially increases the fracture toughness in the preferential direction and decreases the fracture toughness in alternative directions.

The anisotropy of a regular lattice in fracture may not be important if the crack path becomes dominated by localised stress concentrations as a result of randomly distributed 'micro-cracks' (diluted systems) [83, 89], or inhomogeneities [126, 127]. The requirement that randomisation be incorporated into the simulation of homogeneous materials may not be as important in the simulation of heterogeneous materials.

3.5.4 Inelastic Effects.

The introduction of plasticity into lattice spring models is usually through the introduction of residual stresses upon bond failure [128]. Such behaviour is naturally suited to scalar models, where upon reaching a threshold level, the force is maintained as a constant value [129]. Similar systems have been proposed in which the elastic moduli is reduced [96] and the equilibrium lengths of the bonds are increased [130, 131]. Visco-elastic effects have been considered through the introduction of an element which consists of a dashpot in series with a spring [132]; this also

has the effect of introducing a variable bond length into the system. Introducing plasticity, through one-dimensional bond effects, results in anisotropic deformation and a lack of volumetric conservation. In order to rectify this problem a novel method is introduced in section 4.2, in which the plastic deformation is introduced locally at the lattice nodes; this produces a plastic deformation which is isotropic, but not volume conserving.

3.5.5 Particles.

The majority of particulate simulations have been two-dimensional investigations of circular [133–137] and fibre [138, 139] inclusions, although a spherical particle has been investigated in a three-dimensional simulation [140]. The regularity of LSM networks can result in stress anomalies along the particle surface [135]; potentially alleviated through the introduction of interfacial bonds whose characteristics are apportioned according to the weighting of the partial lengths of the bond that straddles the respective domains [137, 141].

3.5.6 Dynamic Effects.

Quasi-static LSMs are assumed to be fracturing under adiabatic conditions; the stress field is locally equilibrated at each iteration, therefore the model involves no time scale, but a sequence of equilibrium states. Dynamical features can be included through the association of mass with nodal points [142], the interaction be-

tween which involves dissipative viscoelastic properties [143]. The propagation and instability of a crack is severely influenced by such viscous effects, and in materials which exhibit rapid fracture processes dynamical effects are significant.

3.6 Conclusions.

Atomistic simulations can provide invaluable information regarding the onset of fracture, especially the competition between dislocation emmision and crack advancement, but is incapable of providing micromechanical insights. The FEM is a powerful technique for simulating deformation and fracture, but computational limitations restrict the system sizes that can be achieved, and hence the number of interacting particles considered.

The Boundary Element Method (BEM) [144] and the Element-Free Galerkin (EFG) method [145] are alternative, though less established, computational techniques which may be applicable to micro-mechanics. The BEM involves the solution of linear boundary value problems with known green's function solutions; the technique is expensive, the resulting linear system is dense, unbanded and often non-symmetric, and nonlinear constitutive relations are problematic [146]. The EFG method is a gridless technique for the solution of partial differential equations which employ moving least square interpolants [145]. The nature of the EFG method requires the solution of a system of equations similar to FEMs, and therefore the computational expense is expected to be similar.

The LSM, whilst not fully capturing the geometric definition of the particles or crack surface with the same precision as other micromechanical techniques, provides an opportunity for investigating stress transfer in multiple particulate systems incorporating substantial damage accumulation.

Chapter 4

The Model.

The model, used in the study undertaken in subsequent chapters of this thesis, consists of the discretisation of space into regularly spaced points (nodes), whose interactions can be manipulated to allow the emergence of continuum mechanical behaviour for a given material specification. In the present notation repeated suffixes are to be repeated over axes x, y, z and suffices following a comma denote differentiation with respect to the cartesian coordinates.

4.1 Elasticity

The elastic model is taken from the two-dimensional work previously undertaken at SHU [96]. The material is represented by an array of 'springs' which occupy the nearest and next nearest neighbour bonds of a simple cubic lattice (see Figure 4.1).

The energy associated with a node m in the lattice is taken to be of the form,

$$E_m = \frac{1}{2} \sum_n (\mathbf{u}_m - \mathbf{u}_n).\mathbf{M}_{mn}.(\mathbf{u}_m - \mathbf{u}_n) \qquad (4.1)$$

where the summation is over all the neighbouring nodes, n, attached to m by a spring, $\mathbf{u}_m$ is the displacement of node m, and $\mathbf{M}_{mn}$ is a symmetric matrix which introduces the elastic properties of the springs. It is shown in the subsequent parts of this section that this system of springs obeys, to first order in the displacement, the equations of continuum elastic theory for an isotropic elastic medium whose elastic constants can be determined in terms of the elements of the matrices $\mathbf{M}_{mn}$.
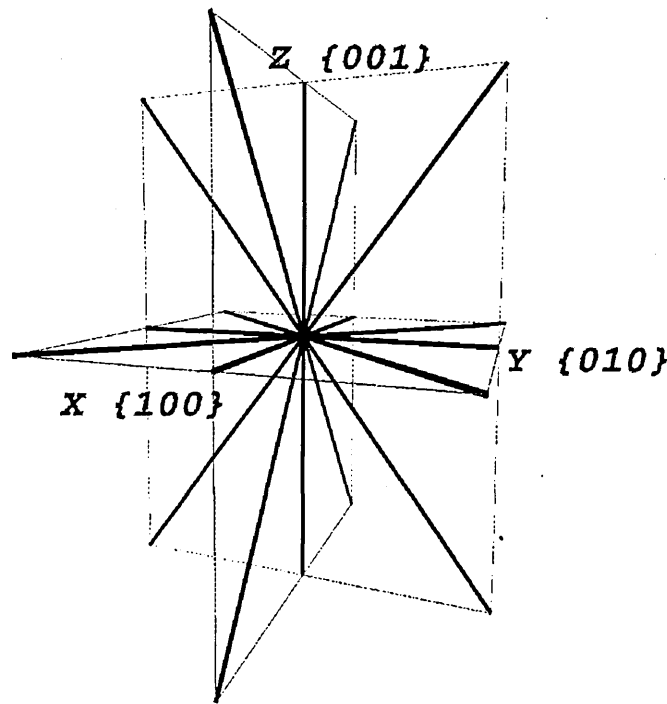
Figure 4.1: Interconnectivity of the lattice spring model is depicted; nearest {100} and next-nearest {110} neighbour spring interactions are considered.

The harmonic form of the energy (4.1) results in forces which are linearly dependent

upon the displacement of the nodes and the resulting set of sparse linear equations are solved by a conjugate gradient method to find the equilibrium configuration which corresponds to no net force at each node. The response of the system is determined by iteratively increasing the applied forces at the boundary nodes and determining the equilibrium state of the springs.

4.1.1   Form of the spring matrices

It is assumed that the matrix associated with the spring in the [100] direction is of the form

$$\mathbf{M}_{[100]} = \begin{pmatrix} k_1 & 0 & 0 \\ 0 & c_1 & 0 \\ 0 & 0 & c_1 \end{pmatrix} \tag{4.2}$$

In this matrix, k_1 and c_1 correspond, respectively, to the central and non-central force constants. Matrices corresponding to the springs in the equivalent symmetry directions are constructed by a similarity transformation of the form, $\mathbf{M}' = \mathbf{R}.\mathbf{M}.\mathbf{R}^T$, where $\mathbf{R}$ is the rotation matrix which rotates a vector in the [100] direction into the required direction. In addition, the matrices corresponding to the set of directions $\{110\}$ have the force constants (k_1, c_1) replaced by (k_2, c_2). Hence, for example, the matrix corresponding to the [110] direction is

$$\mathbf{M}_{[110]} = \begin{pmatrix} \frac{1}{2}(k_2 + c_2) & \frac{1}{2}(k_2 - c_2) & 0 \\ \frac{1}{2}(k_2 - c_2) & \frac{1}{2}(k_2 + c_2) & 0 \\ 0 & 0 & c_2 \end{pmatrix} \tag{4.3}$$

In the following analysis a homogeneous material is considered in which only the force constants (k_1, k_2, c_1, c_2) are used. It is now shown how these constants may be chosen in order to recover an isotropic elastic medium.

4.1.2 Free energy

In order to represent the elastic properties of a medium which is characterised by the spring model described above, the free energy normally associated with an elastic medium was previously generalised [147] to include contributions from an anti-symmetric strain tensor because the model is not rotationally invariant [96]. This arises because the bond bending terms give rise to an energy which depends upon the absolute orientation of the bonds. The problem may be avoided [104] by expressing the energy in a form which depends only upon the angles between the bonds rather than the absolute orientation, as is used in equation (4.1). However this latter approach requires solution of a significantly more complex set of equations and becomes computationally prohibitive when fracture in heterogeneous materials in the presence of plasticity is considered.

The most general quadratic form of the free energy of an elastic continuum which is not rotationally invariant may be written in the form

$$A = \frac{1}{2}\lambda_{iklm}u_{ik}u_{lm} + \frac{1}{2}\gamma_{iklm}\omega_{ik}\omega_{lm} + \frac{1}{2}\eta_{iklm}\omega_{ik}u_{lm} \qquad (4.4)$$

where u_{ik} is the symmetric strain tensor, ω_{ik} is the anti-symmetric strain tensor and the three tensors $\lambda_{iklm}, \gamma_{iklm}$ and η_{iklm} are material parameters. For a three

dimensional system with simple cubic symmetry, it is possible to show that this equation reduces to

$$A = \frac{\lambda_{xxxx}}{2}(u_{xx}^2 + u_{yy}^2 + u_{zz}^2) + \lambda_{xxyy}(u_{xx}u_{yy} + u_{yy}u_{zz} + u_{zz}u_{xx})$$

$$+ 2\lambda_{xyxy}(u_{xy}^2 + u_{yz}^2 + u_{zx}^2) + 2\gamma_{xyxy}(\omega_{xy}^2 + \omega_{yz}^2 + \omega_{zx}^2) \qquad (4.5)$$

where the term pre-multiplied by γ_{xyxy} introduces anti-symmetric contributions to the stress tensor. Extending standard arguments, [147], it can be shown that

$$dA = -SdT + \sigma_{ik}^S du_{ik} + \sigma_{ik}^A d\omega_{ik} \qquad (4.6)$$

where S is entropy, T is temperature, the superscripts S and A refer to symmetric and anti-symmetric tensors, andthe stress tensor is given by, $\sigma_{ik} = \sigma_{ik}^S + \sigma_{ik}^A$ with the symmetric and anti-symmetric contributions being given from equation (4.6) by

$$\sigma_{ik}^S = \left(\frac{\partial A}{\partial u_{ik}}\right)_T \qquad \sigma_{ik}^A = \left(\frac{\partial A}{\partial \omega_{ik}}\right)_T \qquad (4.7)$$

At equilibrium, in the absence of body forces the relation, $F_i = \sigma_{ik,k} = 0$, must be satisfied, which results in the following Lamé equations

$$\lambda_{xxxx}u_{x,xx} + (\lambda_{xxyy} + \lambda_{xyxy} - \gamma_{xyxy})(u_{y,xy} + u_{z,xz}) + \qquad (4.8)$$

$$(\lambda_{xyxy} + \gamma_{xyxy})(u_{x,yy} + u_{x,zz}) = 0$$

$$\lambda_{xxxx}u_{y,yy} + (\lambda_{xxyy} + \lambda_{xyxy} - \gamma_{xyxy})(u_{x,xy} + u_{z,yz}) +$$

$$(\lambda_{xyxy} + \gamma_{xyxy})(u_{y,xx} + u_{y,zz}) = 0$$

$$\lambda_{xxxx}u_{z,zz} + (\lambda_{xxyy} + \lambda_{xyxy} - \gamma_{xyxy})(u_{x,xz} + u_{y,yz}) +$$

$$(\lambda_{xyxy} + \gamma_{xyxy})(u_{z,xx} + u_{z,yy}) = 0$$

For a medium with a free energy given by equation (4.5) undergoing a uniaxial extension, it can be shown that the Young's modulus and Poisson's ratio (assuming isotropy and therefore $\lambda_{xxxx} - \lambda_{xxyy} - 2\lambda_{xyxy} \to 0$) are given by [147]

$$E = \frac{2(\lambda_{xxxx} - \lambda_{xxyy})(\frac{\lambda_{xxxx}}{2} + \lambda_{xxyy})}{\lambda_{xxxx} + \lambda_{xxyy}} \qquad \nu = -\frac{\lambda_{xxyy}}{\lambda_{xxxx} + \lambda_{xxyy}} \qquad (4.9)$$

If the identifications $\lambda_{xxxx} = \lambda + 2\mu$, $\lambda_{xxyy} = \lambda$ and $\lambda_{xyxy} = \mu$ are made, where λ and μ, are the Lamé coefficients, the standard results for the Young's modulus E and Poisson's ratio ν for a three dimensional isotropic material are recovered

$$E = \frac{\mu(3\lambda + 2\mu)}{(\lambda + \mu)} \qquad \nu = -\frac{\lambda}{2(\lambda + \mu)} \qquad (4.10)$$

4.1.3 Mapping of the spring model onto continuum equations

In order to map the spring model onto the continuum equations the Taylor approximation is utilised

$$\mathbf{u}_m - \mathbf{u}_n \approx (\mathbf{e}_{mn}.\nabla)\mathbf{u} + \frac{1}{2}(\mathbf{e}_{mn}.\nabla)^2\mathbf{u} \qquad (4.11)$$

where $\mathbf{u}$ is the vector displacement field of a three dimensional continuum material and $\mathbf{c}_{mn}$ are the bond vectors (*not* unit vectors). This expansion in the expression, $\mathbf{F}_m = \sum_n \mathbf{M_{mn}}.(\mathbf{u_m} - \mathbf{u_n})$ for the force on node m, is used to derive the form of the Lamé equations for the spring model. Alternatively, an expression for the energy density can be derived using the Taylor approximation (4.11) in the energy E_m given by equation (4.1). If the coefficients in these equations are equated with those for the elastic continuum (equations (4.5) and (4.9)), and assuming the primitive cell of

47

the simple cubic lattice has unit side, the following relationships between the elastic constants of the continuum and spring models are obtained

$$\lambda_{xxxx} = k_1 + 2k_2 + 2c_2 \qquad \lambda_{xxyy} = k_2 - c_2$$
$$\lambda_{xyxy} = k_2 + \frac{c_1}{2} + c_2 \qquad \gamma_{xyxy} = \frac{c_1}{2} + 2c_2 \qquad (4.12)$$

It is important to note that although the term γ_{xyxy} associated with the antisymmetric contribution to the free energy does not affect the elastic constants, it is essential for this term to be included if the mapping onto the continuum equations using the free energy expression and the Lamé equations are to be consistent. In order for the spring model to become isotropic it is required that $\lambda_{xxxx} - \lambda_{xxyy} - 2\lambda_{xyxy} \to 0$ and for simplicity $k_2 = k_1$ and $c_2 = c_1$ are chosen. Applying these, the spring model obtains the following properties

$$\lambda = (k - c) \qquad \mu = \frac{1}{2}(2k + 3c) \qquad (4.13)$$

and hence

$$E = \frac{5k(2k + 3c)}{4k + c} \qquad \nu = -\frac{k - c}{c + 4k} \qquad K = \frac{3\lambda + 2\mu}{3} = \frac{5k}{3} \qquad (4.14)$$

where K is the bulk modulus, and is independent of non-central force interactions. The Poissons' ratio has a notable upper bound of a quarter, in the absence of non-central interactions, where it can be seen that the Cauchy relation holds ($\lambda_{xxyy} = \lambda_{xyxy}$).

4.2 Plasticity

In order to expand the range of materials that can be simulated using this LSM, the present formulation is extended to include continuum plasticity. In reality, the shape of the yield surface has a complex load history dependence [148], and this results in anisotropic hardening characteristics. For simplicity a system is considered which undergoes isotropic hardening, in which the yield surface expands isotropically (proportional loading) [149]; this is valid, providing that variations in the principal directions of applied stress remain small.

The Ramberg-Osgood stress-strain relation is adopted from Wilner [1], and utilised in section 5.4. This incorporates a plastic strain field, u_{ij}^p, of the form

$$u_{ij}^p = \frac{9}{14} \left(\frac{\sigma_{eq}}{\alpha}\right)^{n-1} \frac{\sigma'_{ij}}{E} \tag{4.15}$$

where α is the plastic resistance, n is the hardening exponent, and the equivalent stress, σ_{eq}, is defined by $\sigma_{eq} = \left(\frac{3}{2}\sigma'_{ij}\sigma'_{ij}\right)$ (often referred to as the Von Mises stress), where the deviatoric stress tensor is of the form $\sigma'_{ij} = \sigma_{ij} - \frac{1}{3}\delta_{ij}\sigma_{ll}$.

The Hencky-Mises relationship [148] is also adopted (in chapters 6 and 7), incorporating a plastic strain of the form

$$u_{ij}^p = \frac{3}{2\sigma_{eq}} \langle \frac{\sigma_{eq} - \sigma_y}{\alpha} \rangle^n \sigma'_{ij} \tag{4.16}$$

where σ_y is the stress at yielding and the angular brackets dictate that negative values are not considered. The main difference between the two is that the Ramberg-Osgood relation deviates from elasticity instantly, whilst the Hencky-Mises relation

only exhibits plastic deformation at stresses greater than the yield stress. This allows the Hencky-Mises relation to capture the change in gradient at the yield point, although such effects can still pose computational difficulty.

The plastic response of the material depends upon the equivalent stress and the deviatoric stress tensor both of which are undefined for a single bond. Attempting to introduce plasticity through bond dependent criterion results in anisotropic plasticity and, therefore, in this work the plastic response is controlled by the stress fields calculated at each node.

In order to maintain the linearity of the algorithm defined in section 4.1, the plastic response of the material is modelled by decreasing the elastic moduli locally whilst maintaining stress continuity. Thus the force constants of the springs are modified at each iteration, with the modifications being determined by the elastic fields from the previous iteration. The continuity of stress is achieved by incorporating internal forces applied at each node. The force constant for each spring is calculated from the elastic fields at its terminal nodes as shown below.

After each iteration the stress field, σ_{ij}, is calculated at each node and hence the equivalent stress, σ_{eq}. These quantities are used to determine the required value of the strain tensor in the presence of plastic deformation from the relation $u_{ij} = u_{ij}^{e} + u_{ij}^{p}$ where

$$u_{ij}^{e} = \frac{\delta_{ij}\sigma_{ll}}{9K} + \frac{\sigma_{ij}'}{2\mu} \tag{4.17}$$

and the constants K and μ determine the elastic response of the target material. In order to mimic the combined elastic and plastic response, the force constants of the

50

bond are set to be k^t and c^t which are chosen to be equivalent to a material which obeys the relation

$$\frac{\partial u_{ij}}{\partial \sigma_{lm}} = \frac{\partial}{\partial \sigma_{lm}} \left(\frac{\delta_{ij}\sigma_{ll}}{9K^t} + \frac{\sigma'_{ij}}{2\mu^t} \right) \qquad (4.18)$$

This recovers the required differential response of the stress-strain curve. In order to maintain continuity of stress as the bond parameters are modified, an additional force is applied to each end of the spring whose value ψ_{mn} is given by

$$\psi_{mn} = \mathbf{F}'_{mn} - \mathbf{M}^t_{mn}(\mathbf{u}_m - \mathbf{u}_n) \qquad (4.19)$$

where $\mathbf{M}^t_{mn}$ is the bond matrix with the force constants k^t and c^t, and $\mathbf{F}'_{mn}$ is the force which is currently carried by the bond.

The assumption of proportional loading is inaccurate, as the principle stress directions within the simulations are found to vary considerably. The uniaxial stress that is applied to the system may induce proportional loading in a homogeneous system. Although the effects of adding inclusions, especially in the presence of fracture, will lead to severe variations in both the principle stress direction and the yield surface which are not accounted for in the current model.

The Ramberg-Osgood formulation describes non-linear elastic, and not plastic deformation, which predominantly consists of an irreversable component. Currently upon unloading an equivalent elastic response is therefore adopted which, assuming small changes in the forces within the considered region, corresponds to the strain that would be experimentally expected. This is incorporated iteratively, and is therefore extremely inaccurate when considering the sudden reduction of locally applied stress. The equivalent elastic response, which is adopted during the reversal of ap-

plied stresses, does not allow for the finite residual plastic deformation intrinsically, therefore when the stress is completely removed the deformation returns to zero. This is especially problematic in the wake of a crack, where the newly created surfaces cannot support stresses normal to the surface, and must therefore experience a dramatice decrease in local stresses. The only alternative is to consider imposing constant displacement conditions in these regions, although this is currently not possible within the model.

With increasing plastic deformation, the Poisson's ratio is found experimentally to increase to a value close to half and hence corresponds to a volume conserving deformation. However the current model has a Poisson's ratio with an upper bound of a quarter and hence the observed deformation in this scheme is isotropic, but not volume conserving. In order to rectify this problem, a volume conservation term will be required [44]. However, the dominant aspect of plastic deformation is assumed to be the reduction in Young's modulus and, therefore, the present procedure is considered adequate for the situations considered here. It should be noted, however, that the inability of the model to posses a Poisson's ratio greater than a quarter raises compressibility issues, in particular the problems of constraint around particle inclusions. The lack of volume conserving plastic deformation will result in less severe triaxial deformations around inclusions and ahead of propagating cracks. This will inhibit local plastic deformation and subdue plasticity effects.

4.3 Fracture.

The creation of a fracture surface may be achieved through the iterative removal of springs. Adopting a criterion for each individual bond can lead to unrealistic phenomena, as the current model consists of a dual combination of {100} and {110} bonds. If a critical force based criterion was considered then only bonds orientated in the tensile direction would initially satisfy the breaking criterion and regions depleted of these bonds would result. The crack would then propagate through these depleted regions via the removal of bonds not orientated, yet possessing a component, in the tensile direction. It is for this reason that a fracture criterion which enables a surface to be created, through the removal of an assembly of bonds, is considered. Both a stress based criterion, more befitting brittle fracture, and a strain based criterion, more befitting ductile fracture, are determined below.

The relative displacement of node m with respect to node n, in the presence of a uniaxial applied stress in the direction $\hat{n}$, is of the form

$$\mathbf{u_{mn}} \propto (\mathbf{c_{mn}} \cdot \hat{n})\, \hat{n} - \nu\, (\mathbf{c_{mn}} - (\mathbf{c_{mn}} \cdot \hat{n})\, \hat{n}) \tag{4.20}$$

where $\mathbf{c}_{mn}$ is the bond vector, and ν is the Poisson's ratio. The forces which contribute to the stress field in a given direction can be obtained from the displacement field and plastically assigned forces, and therefore the contribution of the bonds in overcoming the cohesive strength of the material can be ascertained.

A critical normal force is adopted for each bond considered to contribute towards the

53

critical stress needed to create a fracture surface in a given direction. The directions in which a crack can propogate are defined as normal to the nearest and next-nearest interactions; bonds whose vectors have positive components in this direction $(\hat{c}_{mn} \cdot \hat{n} > 0)$ are considered.
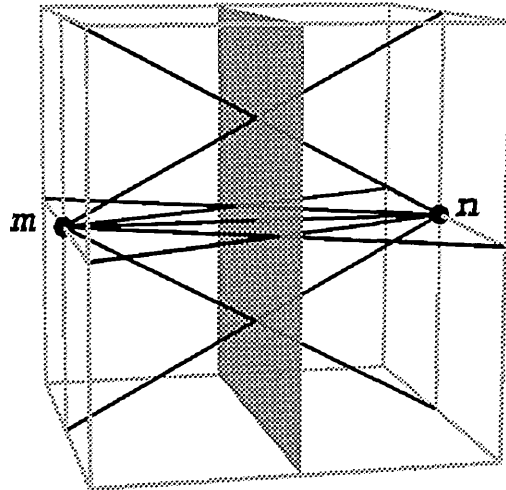
Figure 4.2: Bonds which contribute (black) towards the creation of a fracture surface are depicted.

An example of the bonds considered in the [100] direction between nodes m and n are depicted in figure 4.2. In order for the surface to be created all of the contributing bonds must attain the necessary critical force. In the [100] direction the [100] bond must have a force greater than $0.4\sigma_c$ (where σ_c is the strength of the material), whilst the $\{110\}$ bonds must attain $0.15\sigma_c$. In this event all of the contributing bonds are simultaneously removed.

A strain based criterion is defined through the attainment of a critical relative dis-

placement between neighbouring nodes; in which case all of the bonds whose vectors have positive components in this direction are removed. It is not necessary to consider all of these bonds in the fracture criterion explicitly as they do not directly contribute to the calculation of the strain tensor. Due to the different nature of the two criterion, both are simultaneously considered, and clusters of bonds may therefore be removed for both ductile and brittle fracture.

4.4 Bits and bobs.

The model may be extended to include regions of differing elastic constants. Bonds contained within a certain region, usually spherical, are assigned different elastic properties from those in the matrix. In the current model only the matrix is assumed to exhibit plastic deformation. Bonds which straddle two phases are assigned linearly interpolated values between the two elastic characteristics; in the presence of plasticity an equivalent elastic response is considered.

The strain tensor can be obtained through a finite difference approximation of the displacement field. A central difference approximation can be used

$$\delta_x u_{(i,j,k)} = \frac{-u_{(i+2,j,k)} + 8u_{(i+1,j,k)} - 8u_{(i-1,j,k)} + u_{(i-2,j,k)}}{12h} \qquad (4.21)$$

where $u_{(i,j,k)}$ is the displacement field at coordinates i, j, k, and h is the initial distance between adjacent nodes; alternatively forward or backward approximations are considered at system boundaries and fracture surfaces. The stress tensor is directly

obtainable from the forces acting on a node (the centre of a cubic unit cell) [93],

$$\sigma_{ij} = \frac{\sum_m F_m.n_{ij}^m}{A} \qquad (4.22)$$

Here, $\sum_m$ represents a sum over the cube surfaces, F_m is the force on any surface m of the cubic cell, while n_{ij}^m is a unit vector either normal or parallel to the surface m, and A is the surface area.

In order to distinguish real trends from anomolies as a consequence of discretisation effects at the particle surface, a weighted moving average is sometimes applied to the stress field results (only the contours in section 6.1); the strain field calculation includes information from neighbouring sites and therefore discontinuity effects are less apparent. The weighted average stress field is of the form

$$\sigma_s = \frac{\sum_{i=1}^n w_i \sigma_i}{\sum_{i=1}^n w_i} \qquad (4.23)$$

where the summation is over neighbouring sites, σ_i is the stress field at site i and w_i is the weighting given to the stress field at site i (taken as 1 for the central site and 0.5 for neighbouring sites).

The applied stress is only incremented if no damage is accumulated in the preceding iteration. In this manner the applied stress is escalated until the crack continuously propagates with no further stress increments occurring; at this stage the fracture process is considered catastrophic. The strength of the material being simulated is attributed to the maximum stress level attained, whilst the toughness of the simulation is given by the numerical integration, of the global stress-strain relation, up to the point of catastrophic crack propagation.

Chapter 5

Simulation of the Inhomogeneity

Problem.

An investigation into the effects of an elastic particle embedded, both in an elastically deforming matrix and one exhibiting initial plastic deformation, were performed in order to ascertain the range of validity of the lattice spring model in the simulation of dilute heterogeneous materials. In order to replicate the far field effects of the deforming matrix, a uniform stress tensor was imposed upon the boundary. The far field stress tensor adopted was uniaxial (constant forces applied in the tensile direction, and free boundaries in perpendicular directions) and, in the purely elastic systems, corresponded to a deformation strain of four percent. This section considers the discretisation of a spherical particle, and the variation of particle size and characteristics in order to make comparison with the theoretical predictions of Eshelby [2-4] for an elastic matrix. Results are also presented for a spherical inclusion

in a plastic matrix and are found to be in reasonable agreement with predictions obtained by Wilner [1].

5.1   Discretisation of a Spherical Particle.

The systems consisted of 81^3 nodes and particles were included through the variation of bond characteristics in a localised region of the material; the ratio of Young's modulus was $\frac{E^p}{E^m} = 4$, where p and m denote particle and matrix characteristics respectively, and the Poisson's ratio maintained at $\nu^p = \nu^m = 0.25$. A central node and radius were defined, and any bonds contained within this radius were allocated particle characteristics, whilst bonds which crossed the radius of the spherical particle were considered interface bonds and initially assigned the same properties as particle bonds. Due to the discrete nature of the lattice, the radius can dictate how accurately the spherical particle is approximated. In order to evaluate the elastic field disturbances, these are plotted as a function of the position along the tensile direction (X_x is the tensile direction), relative to the radius of the particle (denoted by R). A diagram depicting the particle, and the loading direction is given in figure 5.1.

Deviations from spherical properties produce stress concentrations, as a consequence of geometrical discontinuities and particle bonds protruding into the matrix. The latter is demonstrated in figure 5.2, which shows elastic fields taken along the tensile direction through the pole of the particle whose radii varies from 10.0 to 10.9; field
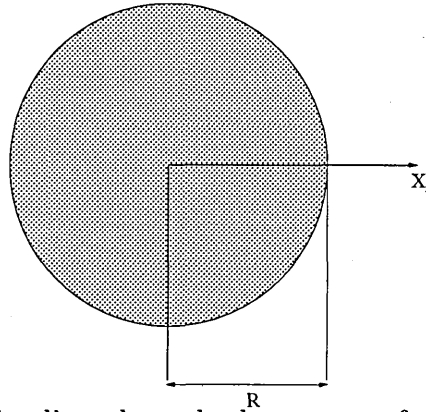
Figure 5.1: The line of loading through the centre of the particle, in the tensile directions. The position currently adopts the centre of the particle as the origin, and loading is applied in the X_x direction.

variations are greatest in this direction. The irregularity observed in a particle of radius 10.0 unit lengths has lead to substantial stress concentrations.

The deviations in the strain field were not as pronounced, as the strain tensor was calculated from a central difference approximation of the displacement field over four unit lengths. In order to alleviate the concentrations due to the discrete nature of the particle the interface bonds were assigned values in between the particle and matrix characteristics; point of intersection of the particle radius through the bond is used to determine a linear interpolation between the matrix and particle characteristics (defined as being spherically smoothed). The subsequent effect upon the stress concentrations, as a result of particle protrusion, can be seen in figure 5.3, which in contrast to 5.2 shows a relatively subdued response to the non-integer effects of the particle radius. It is noted that the most accurate representation of a sphere is obtained with a particle of radius 10.4 unit lengths, and therefore the non-integer portion is taken as 0.4 unit lengths, for varying particle sizes; the optimum spherical representation is almost certainly radius dependent, but with no

59
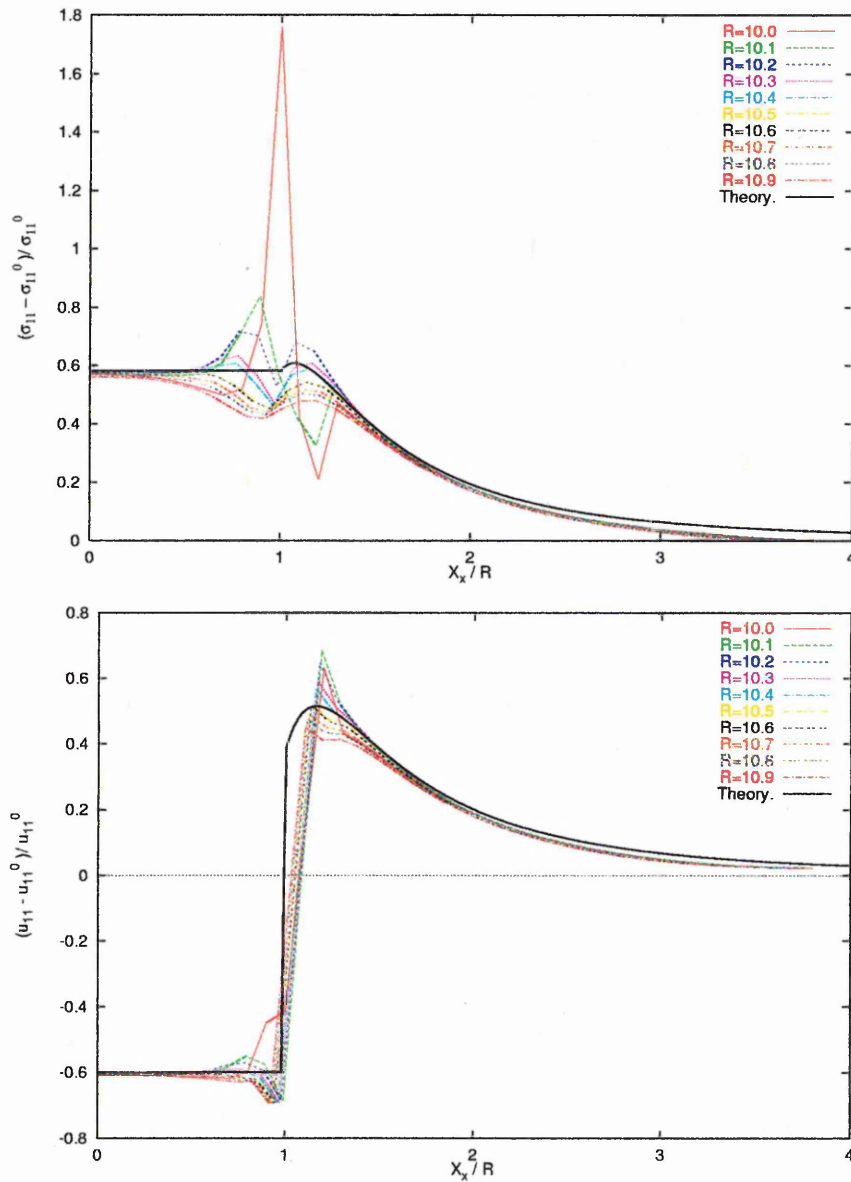
Figure 5.2: Relative normal stress and strain profiles (defined as being in the tensile direction), for varying particle radii, along the tensile direction through the pole. The closed form theoretical solutions taken from eshelby [2–4] are provided for comparison. The fields are depicted relatice to the far field theoretical response, as indicated by the zero superscript.

mathematical proof to dictate the exact non-integer portion, this is considered a reasonable approximation.

Stress concentrations, resulting from spherical discretisation, are not only due to protrusion effects, but also the geometrical discontinuities. Maximum stresses occur away from the poles of the particle as a consequence of cubic characteristics present in the discretised sphere. Such effects were significantly reduced by the linear interpolation, as can be seen in the elastic field profiles in figures 5.4, which shows both particle representations, for a particle radius of 10.4 unit lengths.

The stress concentrations are more pronounced at the interface between the particle and the matrix; there are significant reductions in the particle, which possesses varying interfacial properties. In reality particles may not possess perfect spherical geometry, and such stress concentrations may be influential; this can potentially be imposed upon the geometry of the particle, but should not occur as an artifact of discretisation.

5.2 Variation of Particle Size.

The size of the inhomogeneities considered ranged from 3.4 to 10.4 unit lengths; 0.4 unit lengths being maintained as the non-integer portion. The effects of varying the particle size are compared to the theoretical predictions for a perfectly spherical particle. The elastic properties ($\frac{E^p}{E^m} = 4$ and $\nu^p = \nu^m = 0.25$) are retained.

61
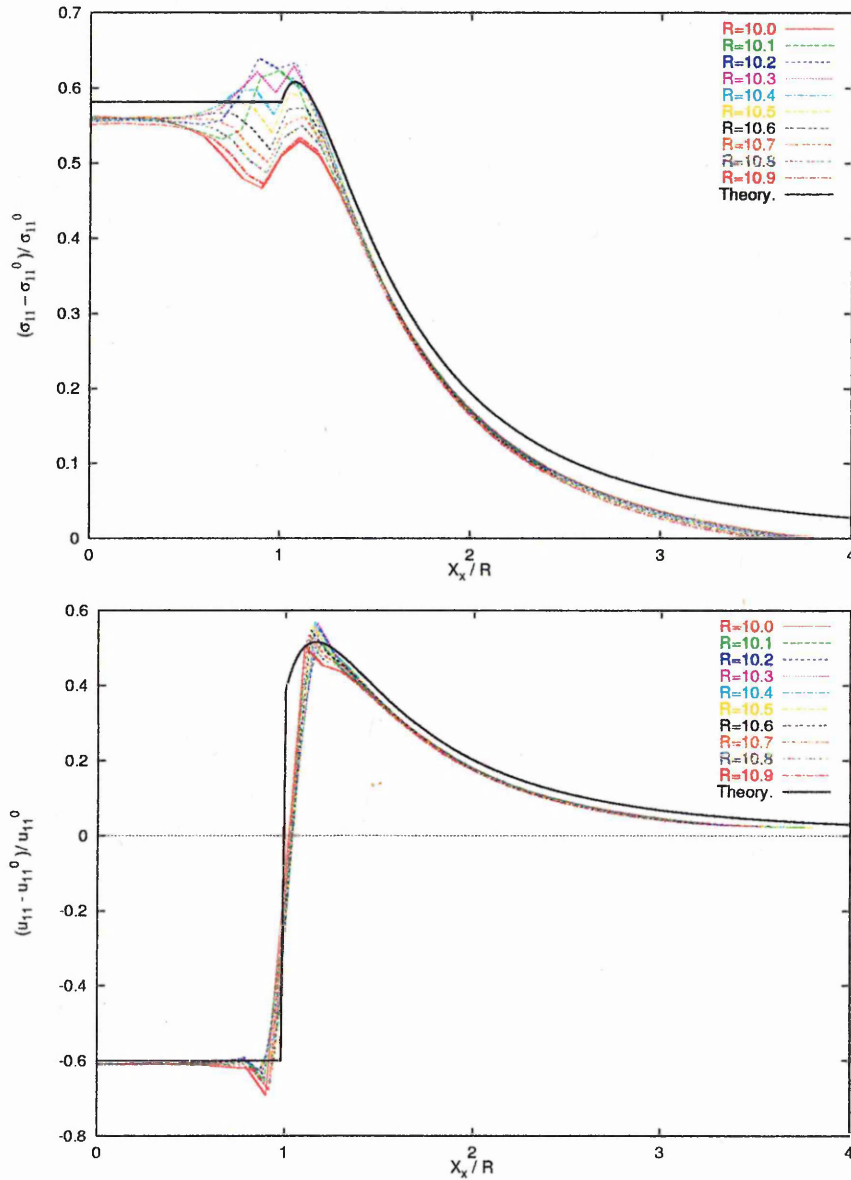
Figure 5.3: Relative normal stress and strain profiles, for varying particle radii, along the tensile direction through the pole. The interface elastic properties are assigned values between the particle and matrix characteristics. The closed form theoretical solutions taken from eshelby [2–4] are provided for comparison. The fields are depicted relatice to the far field theoretical response, as indicated by the zero superscript.
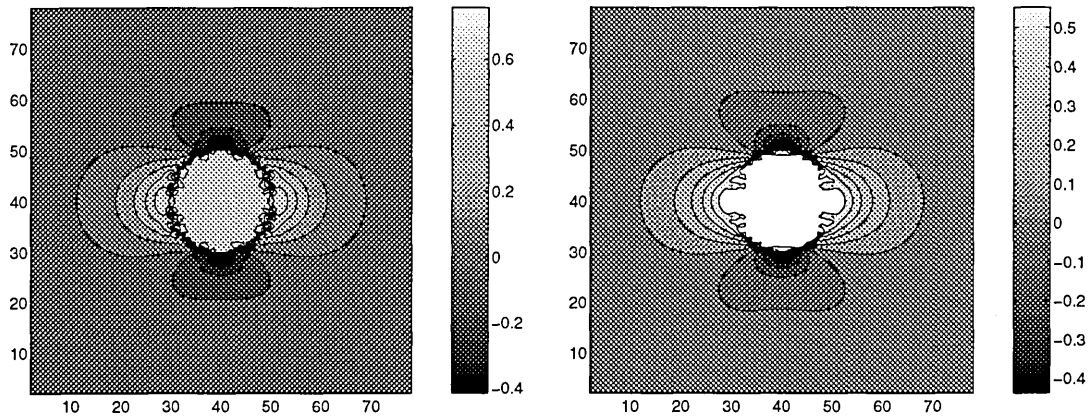
(a)
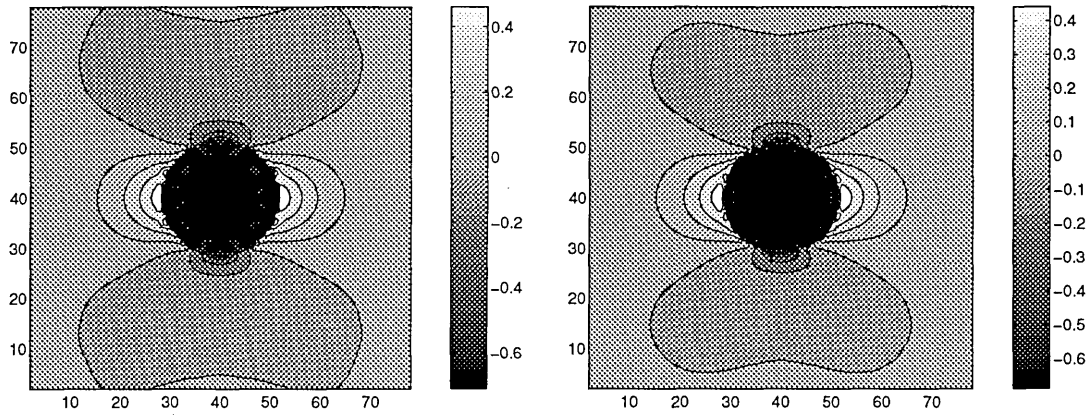
(b)

Figure 5.4: Contour plots of (a) relative normal stress and (b) relative normal strain distributions. Left contour plots depict elastic fields for a particles with interfacial bonds assigned particle characteristics, whilst the contour plots on the right exhibit the smoother elastic fields associated with assigning the interface bonds linearly interpolated force constants, between particle and matrix characteristics.
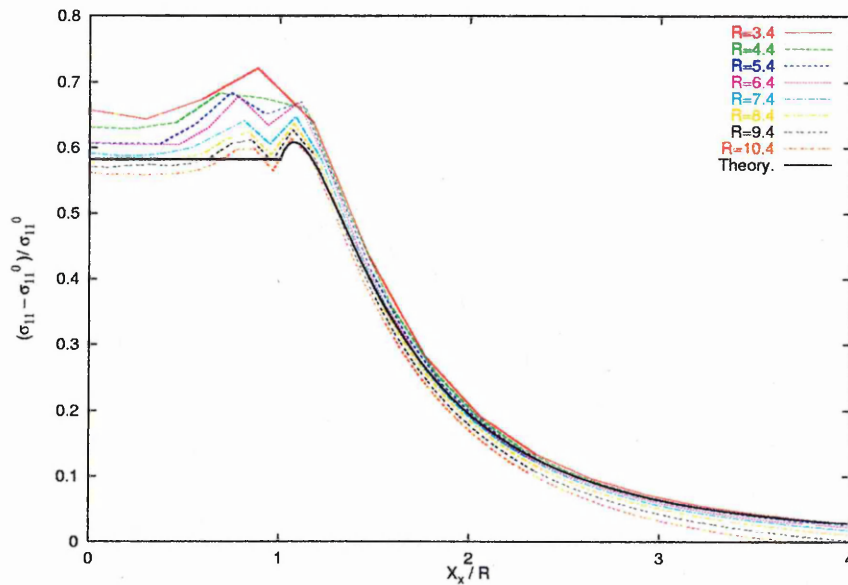
Figure 5.5: Relative normal stress profile, for varying particle radii, along the tensile direction through the pole. The closed form theoretical solutions taken from eshelby [2–4] are provided for comparison. The fields are depicted relatice to the far field theoretical response, as indicated by the zero superscript.

Increasing the particle size results in a more accurate representation of the stress field in the vicinity of the particle (figure 5.5), although the far field response of the simulation deviates from theoretical expectations. The former is a consequence of the improved spherical approximation of the discrete particle, whilst the latter is a result of the imposed stress field at the simulation boundaries; increasing the system size will reduce this effect.

The far field response of the normal strain field (figure 5.6) is reasonably accurate, as the boundary in the tensile direction is allowed to deform, and therefore accommodate the effects of the particle to some degree. In the vicinity of the particle the strain field undergoes a discontinuous change; the strain tensor is calculated from information over a range of nodes, and therefore the discontinuity is averaged out. Selective application of either a narrower central difference approximation, or

64
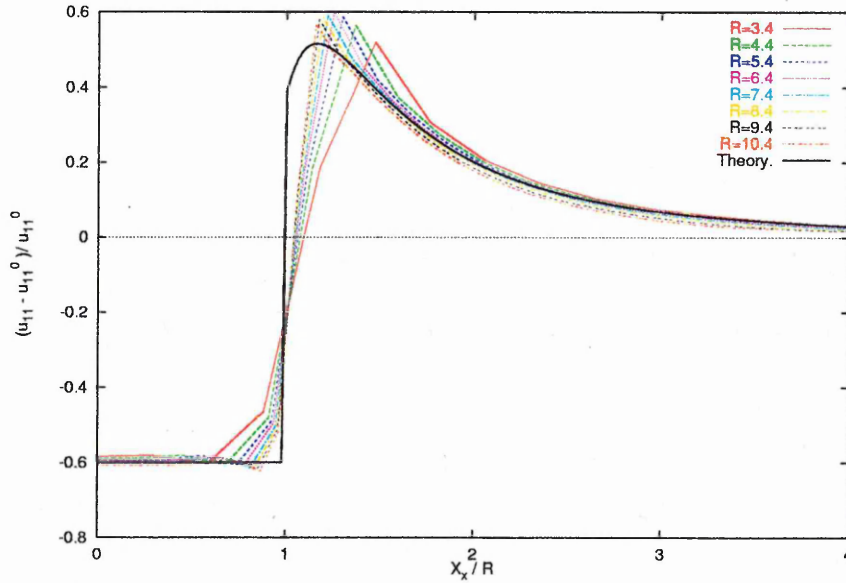
Figure 5.6: Relative normal strain profile, for varying particle radii, along the tensile direction through the pole. The closed form theoretical solutions taken from eshelby [2–4] are provided for comparison. The fields are depicted relatice to the far field theoretical response, as indicated by the zero superscript.
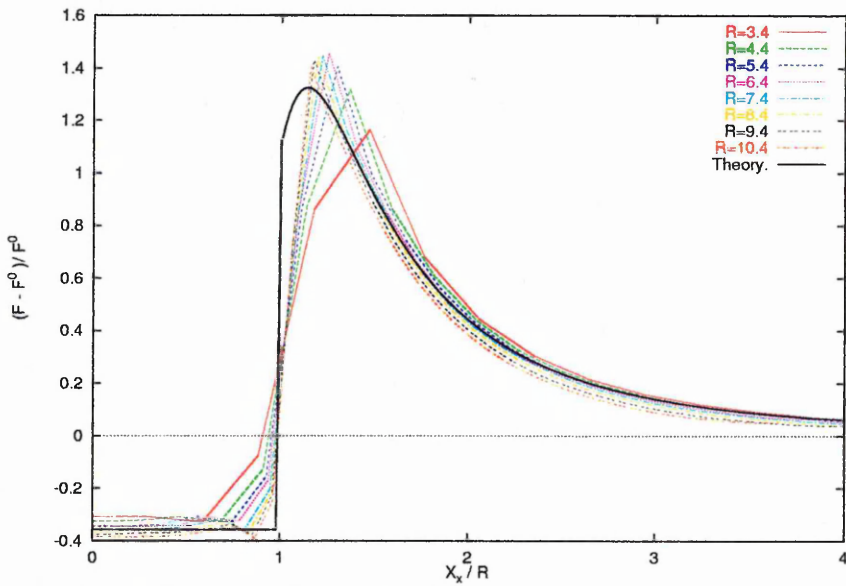
Figure 5.7: Relative free energy profile, for varying particle radii, along the tensile direction through the pole. The closed form theoretical solutions taken from eshelby [2–4] are provided for comparison. The fields are depicted relatice to the far field theoretical response, as indicated by the zero superscript.
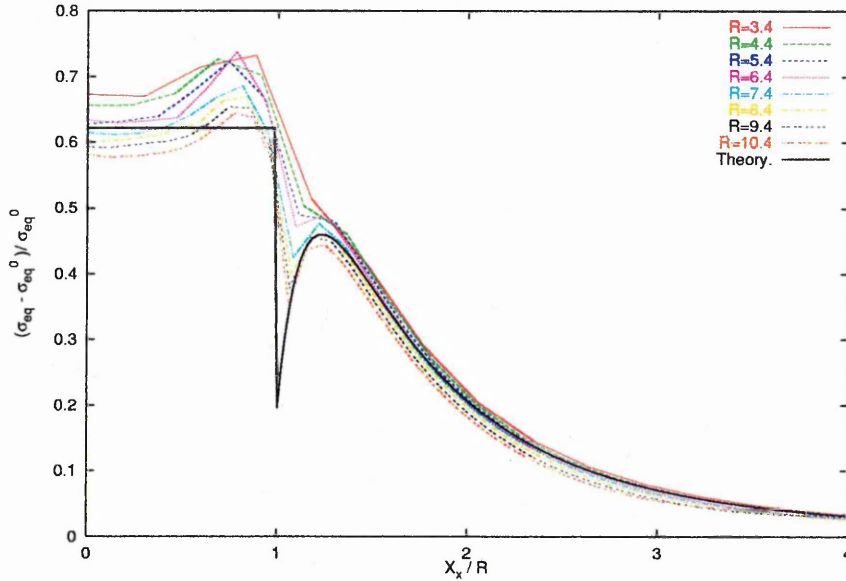
Figure 5.8: Relative von Mises' stress profile, for varying particle radii, along the tensile direction through the pole. The closed form theoretical solutions taken from eshelby [2–4] are provided for comparison. The fields are depicted relatice to the far field theoretical response, as indicated by the zero superscript.
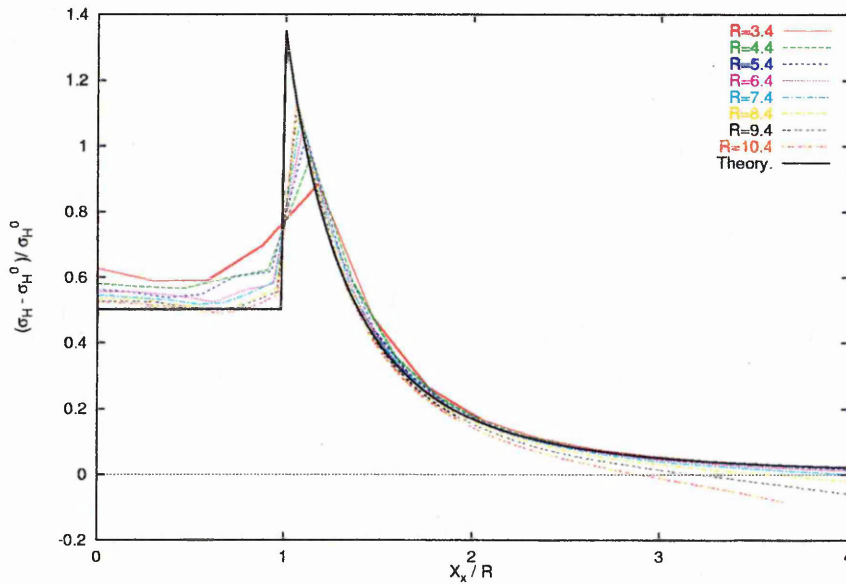

Figure 5.9: Relative hydrostatic pressure profile, for varying particle radii, along the tensile direction through the pole. The closed form theoretical solutions taken from eshelby [2–4] are provided for comparison. The fields are depicted relatice to the far field theoretical response, as indicated by the zero superscript.

appropriate forward/backward difference approximations may facilitate the capture of such discontinuities.

The free energy, von Mises' stress and hydrostatic pressure are also compared with similar characteristics to the stress and strain profiles emerging (figures 5.7 to 5.9). A reasonable replication of the theoretical elastic fields, both in the vicinity of the particle and in the surrounding matrix, is obtained with a particle of radius 7.4 unit lengths; increasing the system size will allow larger particles to be included with greater accuracy.

5.3   Variation of Particle Characteristics.

Considering a particle of radius 7.4 unit lengths, the effects upon varying the ratio of elastic modulii have been investigated. The effects of varying the Young's modulus between the particle and matrix (corresponding to ratios $\frac{E^p}{E^m}$ of 2, 4 and 8), are shown in figures 5.10 to 5.14; the Poisson's ratio is maintained at a quarter. The effect of decreasing the ratio of elastic moduli appears to attenuate the deviations in the simulation results, from theoretical calculations.

A particle is likely to have a different Poisson's ratio than that of the matrix. The effects of altering the particulate's Poisson's ratio is not found to be significant, in comparrison with the effects of varying the Young's modulus.
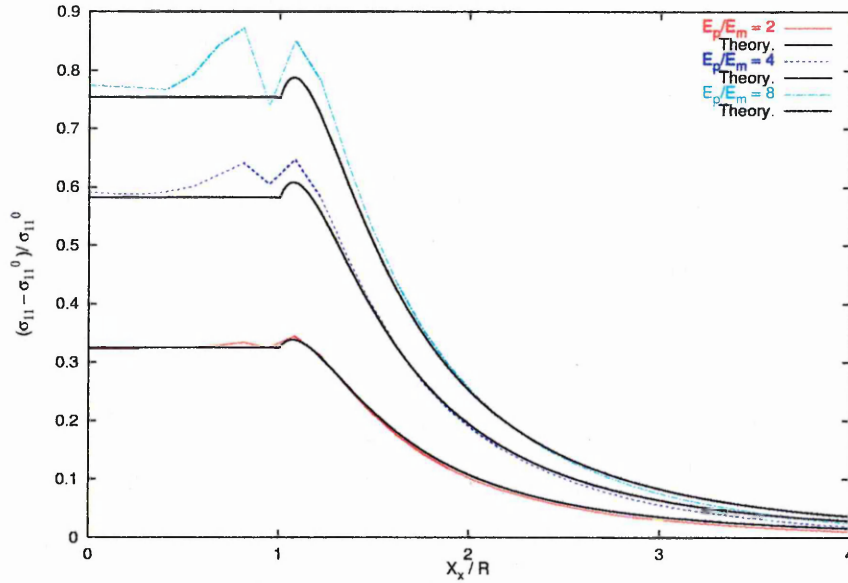
Figure 5.10: Relative normal stress profile, for varying particlulate Young's modulus, along the tensile direction through the pole. The closed form theoretical solutions taken from eshelby [2–4] are provided for comparison. The fields are depicted relatice to the far field theoretical response, as indicated by the zero superscript.
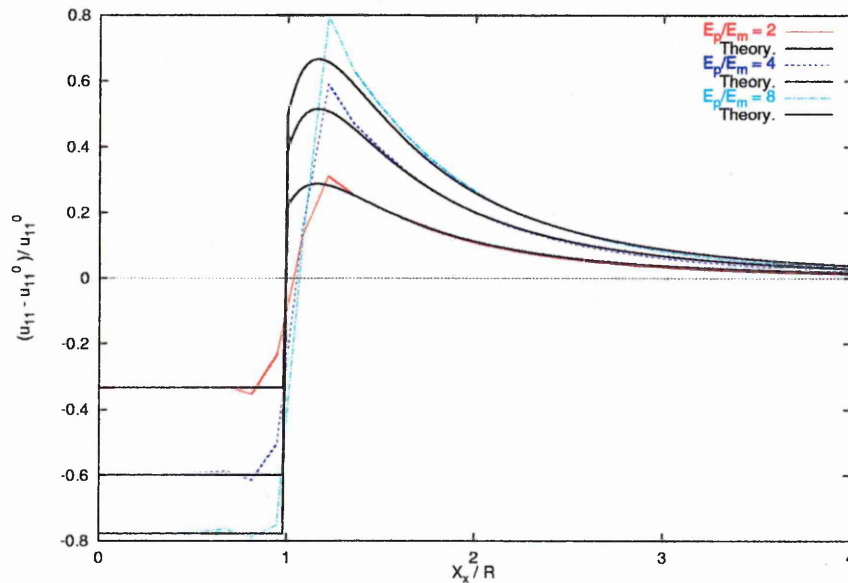
Figure 5.11: Relative normal strain profile, for varying particlulate Young's modulus, along the tensile direction through the pole. The closed form theoretical solutions taken from eshelby [2–4] are provided for comparison. The fields are depicted relatice to the far field theoretical response, as indicated by the zero superscript.
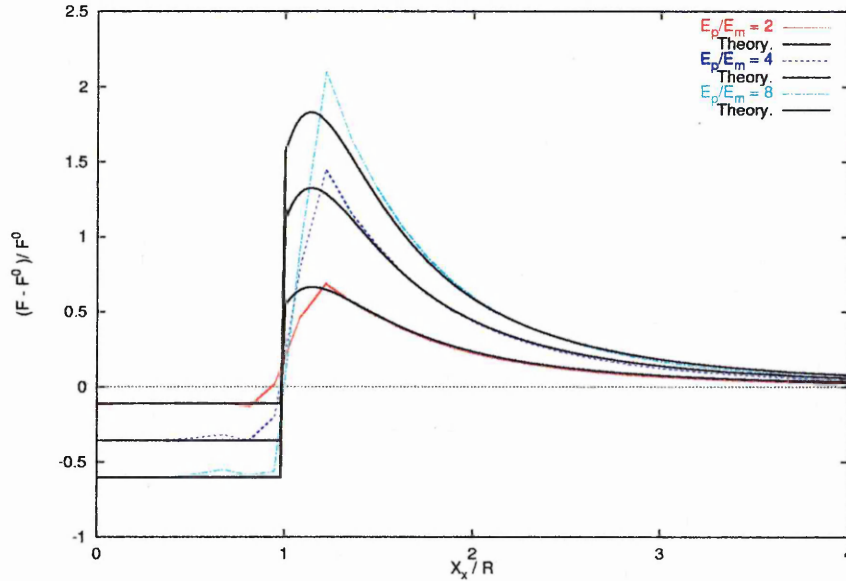
Figure 5.12: Relative free energy profile, for varying particlulate Young's modulus, along the tensile direction through the pole. The closed form theoretical solutions taken from eshelby [2–4] are provided for comparison. The fields are depicted relatice to the far field theoretical response, as indicated by the zero superscript.
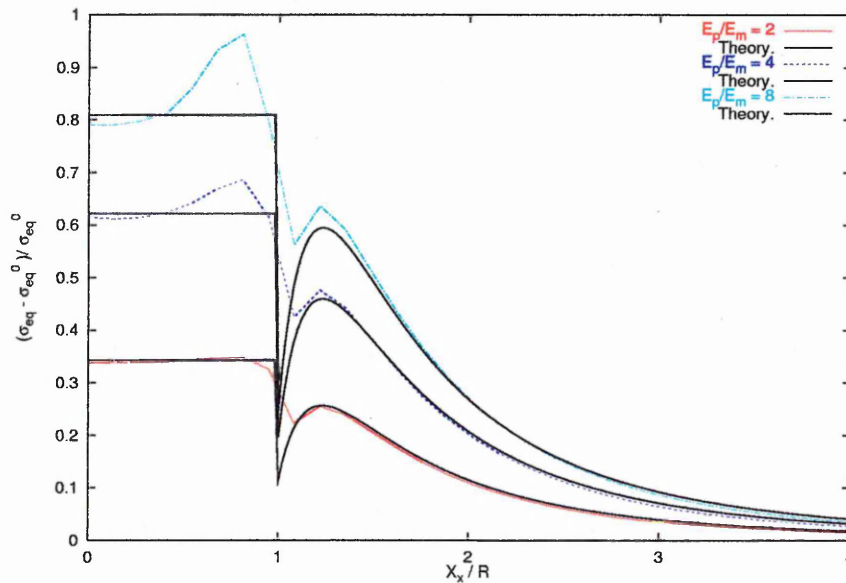
Figure 5.13: Relative von Mises' stress profile, for particlulate Young's modulus, along the tensile direction through the pole. The closed form theoretical solutions taken from eshelby [2–4] are provided for comparison. The fields are depicted relatice to the far field theoretical response, as indicated by the zero superscript.
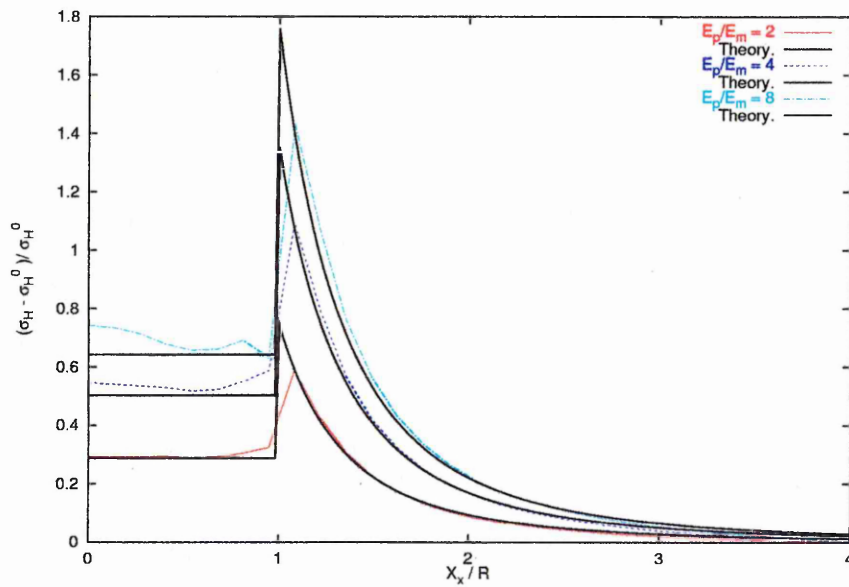
Figure 5.14: Relative hydrostatic pressure profile, for particlulate Young's modulus, along the tensile direction through the pole. The closed form theoretical solutions taken from eshelby [2–4] are provided for comparison. The fields are depicted relatice to the far field theoretical response, as indicated by the zero superscript.

5.4 Elastic inclusion in plastic matrix

In this section we present results for an elastic inclusion embedded within a plastic matrix. Of particular importance in real materials is the inability of elastic inclusions to deform to the same extent as a plastically deforming matrix. This can be the source of internal necking in particulate systems, leading to premature failure. In order to incorporate the micromechanical behaviour of such systems into a LSM, plasticity must first be introduced. Here, the incipient stages of plastic deformation around an elastic inclusion are simulated. The system considered is directly comparable to that studied by Wilner in which equation (4.15) reduces, for uniaxial stress strain behaviour, to the relation [1]

$$\epsilon = \frac{\sigma}{E} \left[1 + \frac{3}{7} \left(\frac{\sigma}{\alpha} \right)^{n-1} \right]. \tag{5.1}$$

The ductility of a nondimensional Ramberg-Osgood stress-strain relation (α is unity) is dependent upon the hardening exponent, n, which is assigned a values of 19, characteristic of a considerably ductile response. The initial elastic properties are also taken from Wilner and consist of particle to matrix Young's moduli ratio of two and a Poison's ratio of a quarter for both phases. The plastic zone is defined as being a region were the Mises stress is greater than the plastic resistance; in order to make comparison with the results of Wilner (which displayed a Mises stress contour of one), only Mises stress values in the range 0.99α to 1.01α are considered in Figure 5.15. From symmetry it is only necessary to present data for one quadrant of the contour map.

The onset of plastic deformation is related to a critical Mises stress and, therefore, the initial plastic zone is expected to develop where the maximum Mises stress occurs (Figure 5.8); this is generally observed in the literature at a position separate from the particle [53, 54, 150]. In the present simulation this phenomenon is not fully captured, due to the discretisation of the particle, and the plastic zone develops at the interface of the particle (Figure 5.15a). Increasing the applied stress (Figures 5.15b, 5.16a, and 5.16b) results in further growth of the plastic zone along the line of loading, and hence a local increase in deformation, causing an increase in Mises stress at roughly $r/a \approx 2$ in the equatorial plane. Comparable phenomena have been observed using FEMs [56, 57], but the numerical results of Wilner [1](based on a variational method), show a more pronounced effect than the LSM simulations presented here; this is attributed to the lack of volume conservation in the plastic zone along the tensile polar axis. Another discrepancy with the results of Wilner is the effect of the boundary conditions on the Mises stress profile. In the LSM, the applied far field imposes a constant normal stress contour along the boundary, which curbs the Mises stress profile. That said, the model captures the essential features of the evolution of the plastic zone and are very similar to those reported by Wilner [1].

The three-dimensional surface contours, with similar parameters as the above system, are considered in figure 5.17, which depicts surfaces of constant equivalent stress equal to the plastic resistance. The surface profiles appear to exhibit no significant discretisation effects and the onset of plastic deformation is equivalent in all directions perpendicular to the tensile direction. In figure 5.17a the particle is

72

at a higher Von Mises stress than the matrix, and is therefore contained within the surface of constant Von Mises stress, along with polar region on the particle surface; external regions are at a lower Von Mises stress. Increasing the applied stress (figures 5.17b and 5.17c) results in an increase in volume which is considered yielded, this can be interpreted from the funnel of constant Von Mises stress eminating in the polar direction from the particle surface. Surface effects are also noticable in this region. Increasing the applied stress further (figures 5.17d) results in an area of lower Von Mises stress being contained within the surface contour, whilst the surrounding outer region is greater than the plastic resistance, and therefore considered yielded.

5.5   Conclusions.

Numerical simulation of the elastic inhomogeneity problem, utilising a LSM, has been undertaken and it is found that the analytical solutions of Eshelby are reasonably replicated, although the discretisation of a spherical particle results in elastic field anomalies at the particle-matrix interface. In reality the particles may not be perfect spheres (or ellipsoids), and the consequences of stress concentrations resulting from geometric anomolies may be more significant than discretisation effects.

It is found that the onset of plastic deformation agrees well with that determined using alternative methods. The simulation does exhibit surface effects, but the discretisation does not appear to hinder the ability of the model to capture the

three-dimensional yield characteristics.
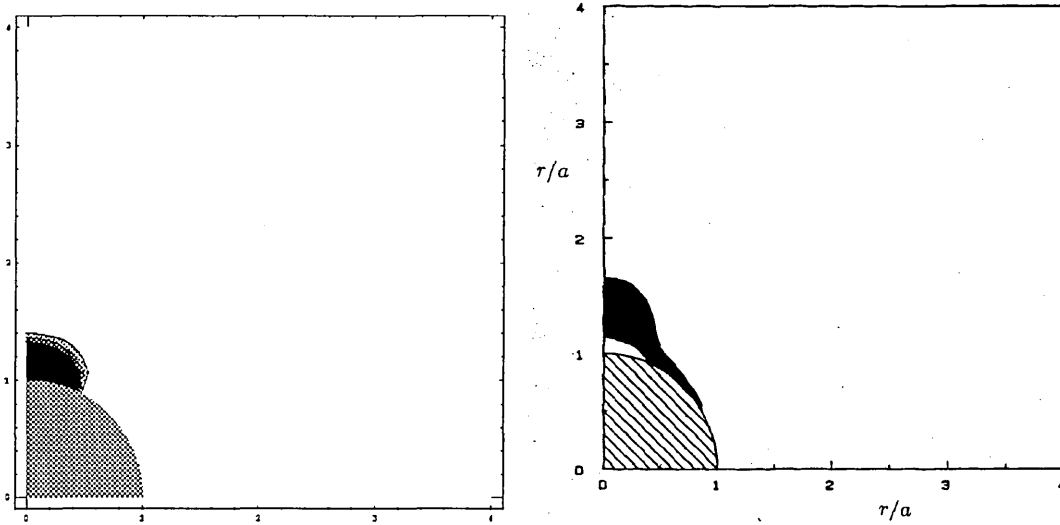
(a)
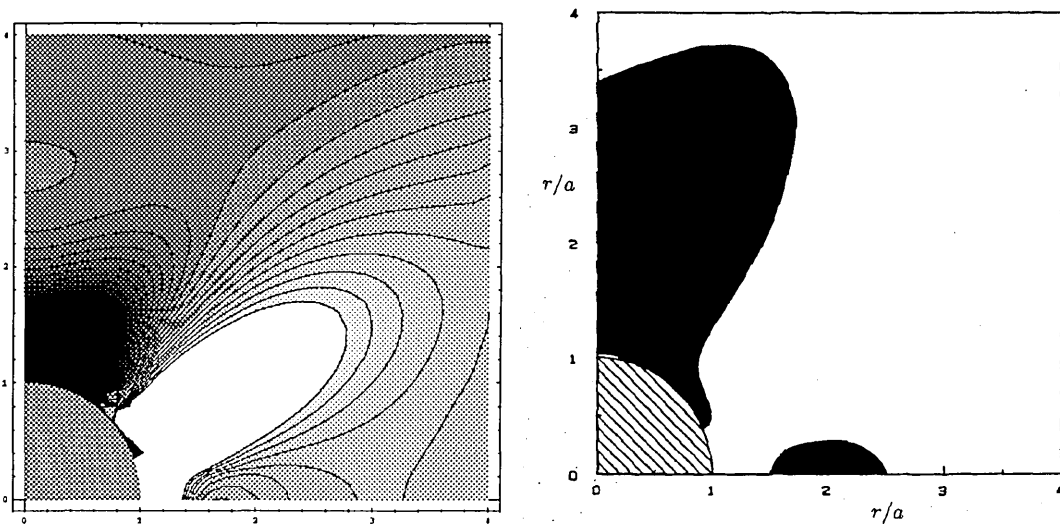
(b)

Figure 5.15: Comparison between LSM (left) and Wilner [1](right) of the Mises stress profile exhibiting the onset and growth of plastic zone (defined as $\sigma_{eq} = \alpha$). The ratio of particle to matrix Young's modulus is two, both phases are assigned a Poisson's ratio of a quarter, and the hardening exponent is nineteen. Within the LSM the particle diameter is thirteen unit lengths, and the vertically applied stresses are a) $\sigma/\alpha = 0.95$, b) $\sigma/\alpha = 0.9975$. Mises stress values in the range 0.99α(white) to 1.01α(black) are presented in 20 contours in the LSM results, whilst a single contour at $\sigma_{eq} = \alpha$ is presented from Wilner.
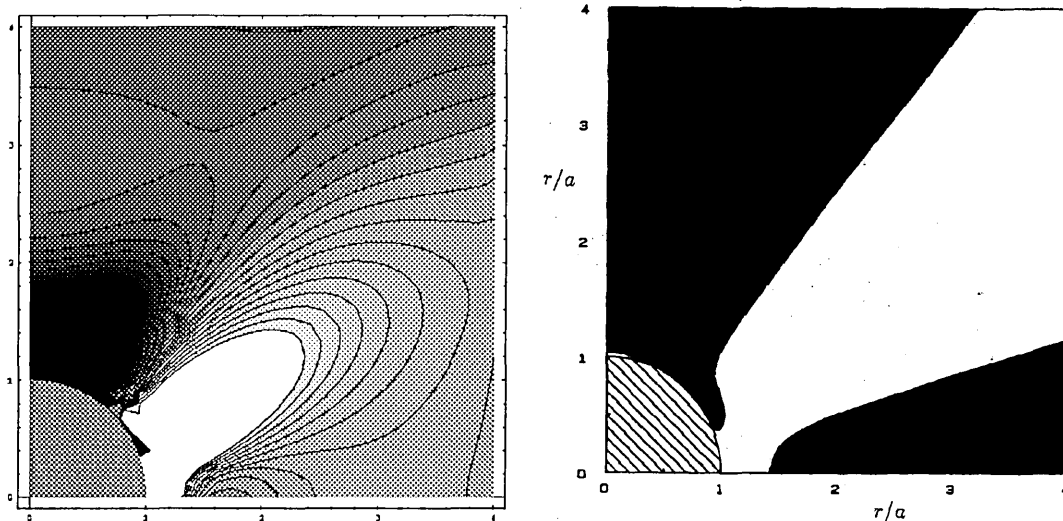
(a)
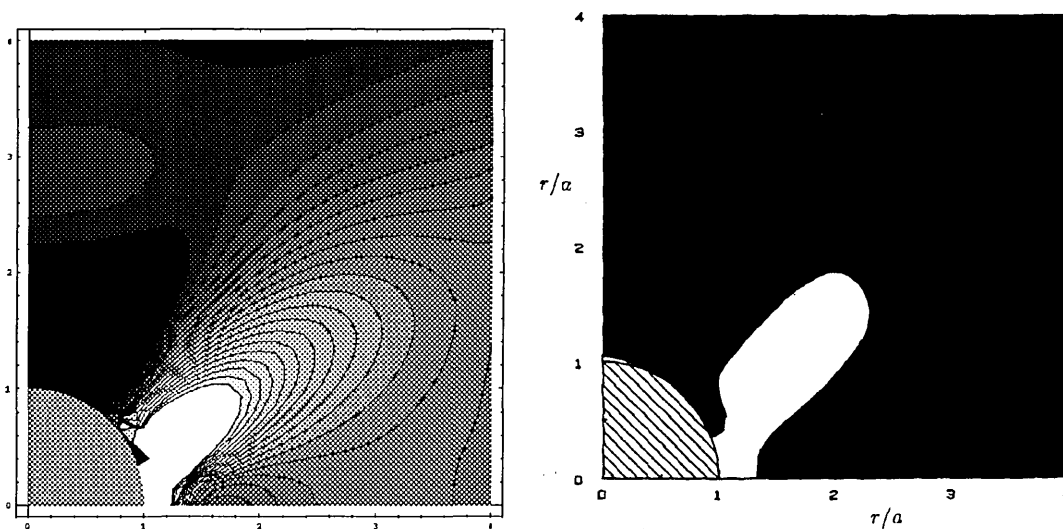
(b)

Figure 5.16: Comparison between LSM (left) and Wilner [1](right) of the Mises stress profile exhibiting the onset and growth of plastic zone (defined as $\sigma_{eq} = \alpha$). The ratio of particle to matrix Young's modulus is two, both phases are assigned a Poisson's ratio of a quarter, and the hardening exponent is nineteen. Within the LSM the particle diameter is thirteen unit lengths, and the vertically applied stresses are a) $\sigma/\alpha = 1.0$, b) $\sigma/\alpha = 1.005$. Mises stress values in the range 0.99α(white) to 1.01α(black) are presented in 20 contours in the LSM results, whilst a single contour at $\sigma_{eq} = \alpha$ is presented from Wilner.

76
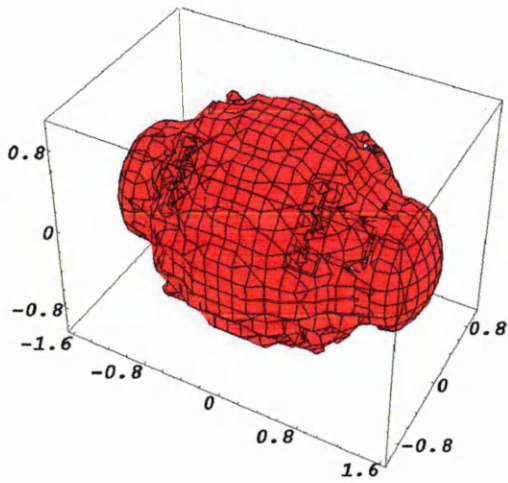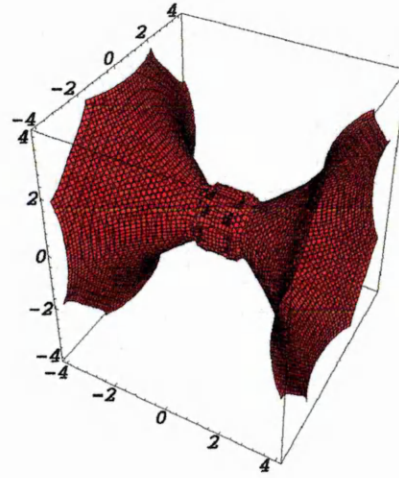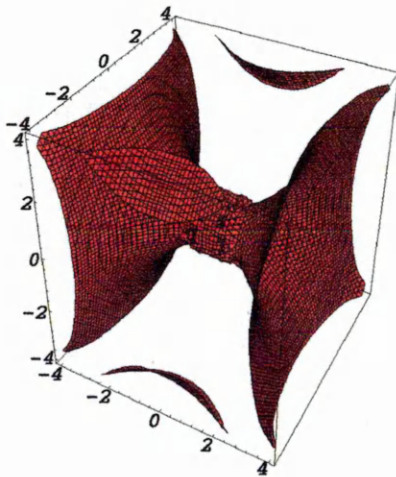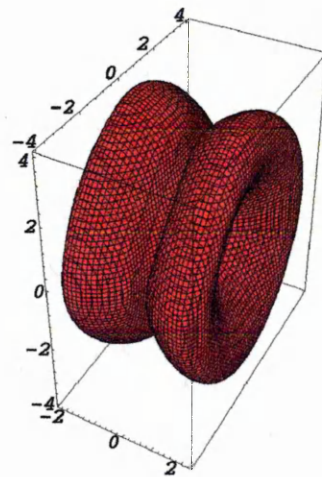
Figure 5.17: Surface of constant Von Mises stress exhibiting the onset and growth of plastic zone (defined as $\sigma_{eq} = \alpha$). The ratio of particle to matrix Young's modulus is two, both phases are assigned a Poisson's ratio of a quarter, and the hardening exponent is nineteen. The particle diameter is fifteen unit lengths, and the applied stresses (in the x-direction) are a) $\sigma/\alpha = 0.95$, b) $\sigma/\alpha = 0.9975$, c) $\sigma/\alpha = 1.0$, and d) $\sigma/\alpha = 1.005$.

Chapter 6

Particulate systems in steel.

The effects of incorporating three different varieties of heterogeniety within a matrix, whose continuum mechanical behaviour corresponds with that of austenitic steel, are investigated in this current chapter. The resulting deformation fields for systems containing a single inclusion are elucidated. The subsequent damage accumulations, through either particle decohesion or fracture, are explored. The single inclusions considered are a spherical iron carbide (Fe3C) particle, a spherical and an elongated spherocylindrical manganese sulphide (MnS) particle, and a spherical void.

Both the theoretical investigation, and simulation, of ductile fracture often considers a uniform distribution of inclusions, along with the assumption of simultaneous nucleation of voids at all particles. In this chapter the detrimental effects of inclusion interaction through the simulation of the deformation and damage accumulations in three-dimensional systems, containing two inclusions (either Fe3C or voids) are

studied. The simulation of MnS particles are not undertaken as the effects of particle debonding and nucleated void interactions are expected to be similar in both Fe3C and MnS particle systems.

The plasticity algorithm, described in section 4.2, is now utilised to describe the continuum mechanical behaviour of an austenitic steel. The experimental stress-strain tensile behaviour, provided by Rolls-Royce Associates, is best approximated by the Hencky-Mises relation. The curve that best describes the experimental behaviour exhibits quite severe yielding which can result in computational difficulties. The sudden onset of plastic deformation, accompanying yielding, can shield neighbouring regions (i.e. reduce the stress by deforming to a greater degree in an adjacent region); a resultant rippling effect ensues consisting of low (shielded) and high deformation bands within the simulation. This effect is unrealistic and therefore a gradual onset of plastic deformation is sought, with the Ramberg-Osgood relation being applicable, providing as it does, a continuous functional form. The Ramberg-Osgood relation notoriously fails to capture the stress-strain curve at the initial onset of yielding, and therefore a compromise is obtained by applying the Hencky-Mises relation, but mathematically considering a lower yield strength. The resultant theoretical stress-strain behaviour, adopted in the present analysis, along with the experimental data is presented in figure 6.1. The non-dimensional stress is normalised to the yield strength of the austenitic steel (525MPa), whilst the strain is intrinsically non-dimensional. It should be noted that mathematically, whilst determining the constitutive Hencky-Mises relation, σ_y is redefined as half the yield stress but elsewhere in the study unity is chosen for normalisation purposes.

79
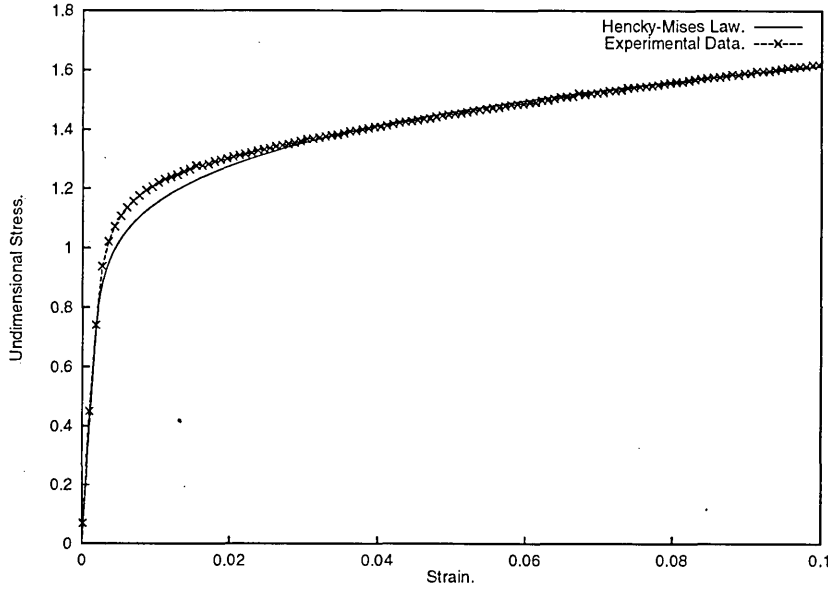
Figure 6.1: Theoretical Hencky-Mises relation and experimental stress-strain tensile relation. The uniaxial behaviour is of the form, $u = \frac{\sigma}{E} + \langle \frac{\sigma - \sigma_y}{\alpha} \rangle^n$. The non-dimensional parameters are as follows: E (Young's modulus) is 400, σ_y (yield stress) is 0.5, α (plastic resistance) is 1.8 and n (hardening exponent) is 4.86 .

The constituent properties, for iron carbide and manganese sulphide particles, are obtained from the literature and are summarised in the following table

Parameter	Dimensional value	Non-dimensional value
Youngs'Modulus of Steel	210 GPa	400
Youngs'Modulus of Fe3C [14]	268 GPa	510.5
Youngs'Modulus of MnS [35]	137 GPa	260.9
Fe3C interfacial strength [30]	1024 MPa	$1.95\sigma_y$
Fe3C fracture strength [29]	2027 MPa	$3.86\sigma_y$
MnS interfacial strength ($\perp \sigma$) [37]	810 MPa	$1.54\sigma_y$
MnS fracture strength ($\parallel \sigma$) [37]	1120 MPa	$2.13\sigma_y$

It should be noted that whilst a critical strength is applicable to the brittle fracture of inclusions, and to interfacial debonding, this is not the case when considering the fracture of the ductile matrix and therefore a strain based criterion is considered; the critical strain in the present study corresponds to 60% deformation.

80

6.1   Deformation of single particle systems.

Spherical inclusions of radius 7.5 unit lengths were simulated in a system of 61^3 nodes; in this section damage accumulation is not considered. The inclusions considered were a Fe3C particle, a MnS particle and a void. Contours though the centre of the particle are considered in the three-dimensional system, as the deformation fields perpendicular to the tensile direction are equivalent in all radial directions from the polar axis (through the particle centre, in the tensile direction). The stress concentration factor is investigated, being defined here as the ratio of the stress within a particle to the far field stress. The one-dimensional stress and strain profiles along the polar axis are also examined.

The Fe3C particle possesses a greater Young's modulus than the steel matrix and therefore is unable to deform to the same extent. This results in the non-dimensional normal stress and normal strain fields (where normal refers to the fields in the tensile direction and non-dimensional means the fields are divided by the yield stress) given in figure 6.2, which shows the elastic fields prior to plastic deformation (applied stress $= 0.5\sigma_y$). The stress and strain fields in the matrix are concentrated at the pole of the particle in the tensile direction, and reduced at the particle surface in the equatorial plane. The stress is concentrated in the particle, whilst the strain in the particle is abated.

The stress field within the Fe3C particle is initially uniform, as theoretically expected in the elastic regime, but in the presence of plastic deformation the field becomes

81
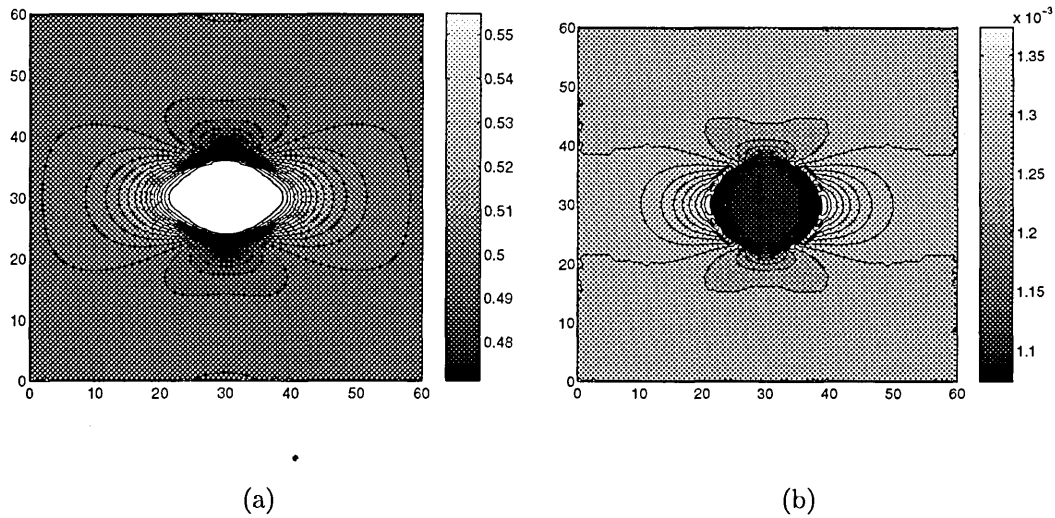
Figure 6.2: 2D Contour plots, taken through the Fe3C particle centre, of non-dimensional (a) normal stress and (b) normal strain distributions in a Fe3C particulate stystem. The applied stress, in the horizontal direction, is $0.5\sigma_y$.

increasingly non-uniform. The stress and equivalent stress fields, at an applied stress of $1.5\sigma_y$, are shown in figure 6.3. The non-uniformity has been mentioned within the literature [1,53], where one-dimensional profiles along the polar axis reveal that the stress is greater at the centre of the particle and reduces towards the particle interface. Whilst this phenomena is present in the figure 6.3, it is also noted that the two-dimensional profile reveals an additional development; concentrations in normal stress within the particle in the equatorial plane towards the interface and radial concentrations of equivalent stress towards the particle interface with a local minimum at the centre.

In contrast with the Fe3C particle, the MnS particle possesses a lower Young's modulus than the steel matrix, and hence the resultant elastic fields are therefore dissimilar to the Fe3C particulate system. The normal stress and normal strain fields are presented in figure 6.4, and are qualitatively opposite from the fields associated
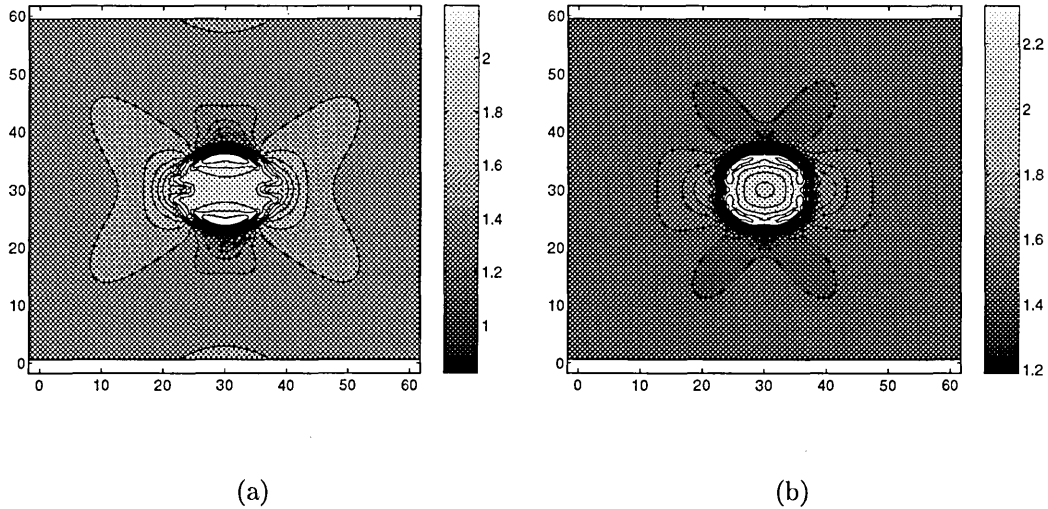
Figure 6.3: 2D Contour plots, taken through the Fe3C particle centre, of non-dimensional (a) normal stress and (b) equivalent stress distributions in a Fe3C particulate stystem. The applied stress, in the horizontal direction, is $1.5\sigma_y$.

with the Fe3C particle. The MnS particle is capable of deforming to a greater extent than the steel matrix, and therefore the normal strain field is concentrated within the particle whilst the normal stress is reduced. The elastic fields within the matrix are intensified in the equatorial plane and suppressed in the tensile direction.

Increasing the applied stress has the effect of increasing the plastic deformation and therefore the matrix is able to deform to a greater extent than the particle. This shifts the regions of stress concentration and relaxation as indicated in figure 6.5. As the applied stress is increased further, the profiles exhibit the same characteristics as the profiles from the simulation containing a Fe3C particle.

The remaining inclusion considered is a void and therefore does not sustain a stress or strain field. The elastic fields in the matrix are concentrated in the equatorial plane, as shown in figure 6.6. As the stress is increased the regions of stress and strain
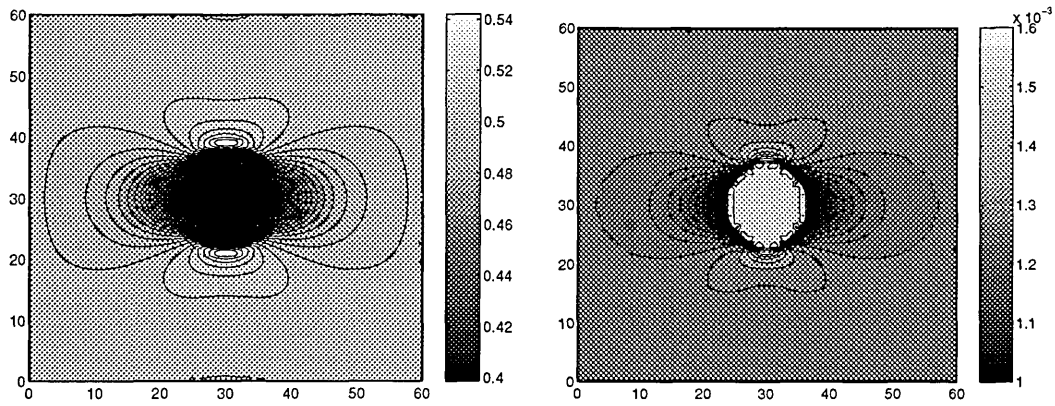
Figure 6.4: 2D Contour plots, taken through the MnS particle centre, of non-dimensional (a) normal stress and (b) normal distributions in a MnS particulate stystem. The applied stress, in the horizontal direction, is $0.5\sigma_y$.

concentration and relaxation remain similar, but the form varies. The main feature

of interest is the extension of the region of strain concentration in the equatorial plane

with increased plasticity; potentially significant when two voids (both orientated in

the others equatorial plane) are positioned in close proximity.

The stress gathering capability of a particle (defined as the ratio of stress within the

particle to the far field applied stress) is considered to be an indicative parameter

when assessing the detrimental effects of particulate systems [58]; it would appear

that the stress in the particle is usually quantified as the level of stress within the

centre of the particle. One-dimensional profiles of the stress and strain fields along

the tensile polar axis, with increasing applied stress, are presented in figures 6.7 and

6.8. The fields are normalised with respect to the far field.

The normal stress field in the Fe3C particle is shown in figure 6.7a. The magnitude
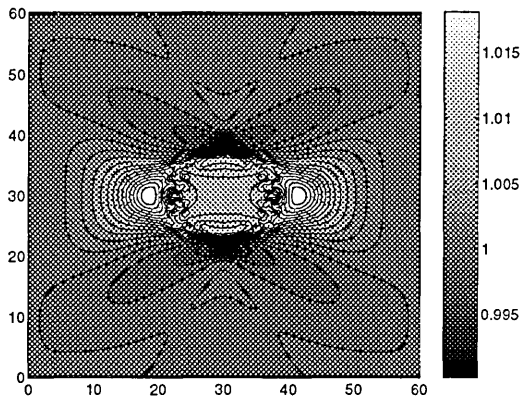
(a)
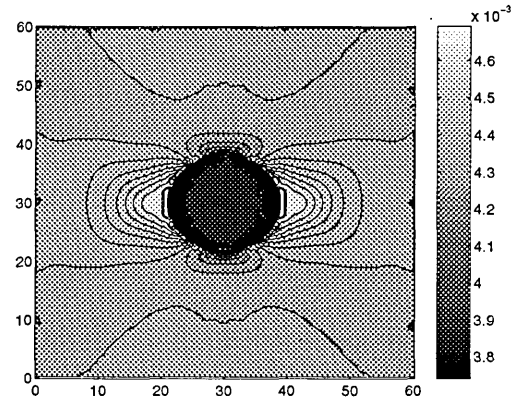
(b)
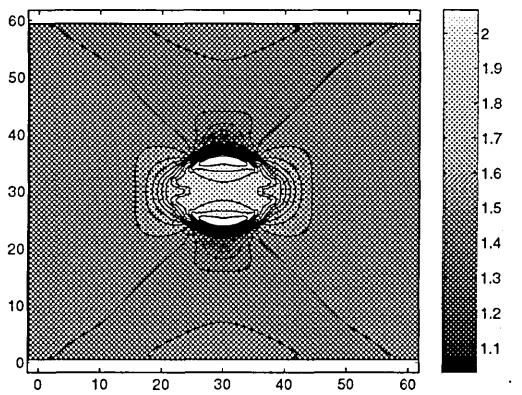
(c)
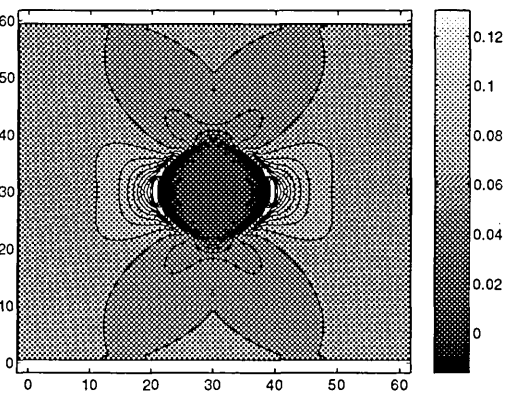
(d)

Figure 6.5: 2D Contour plots, taken through the MnS particle centre, of non-dimensional (a) normal stress at an applied stress of σ_y, (b) normal strain at an applied stress of σ_y, (c) normal stress at an applied stress of $1.5\sigma_y$, and (d) normal strain at an applied stress of $1.5\sigma_y$; loading is in the horizontal direction.

(a)   (b)

(c)   (d)
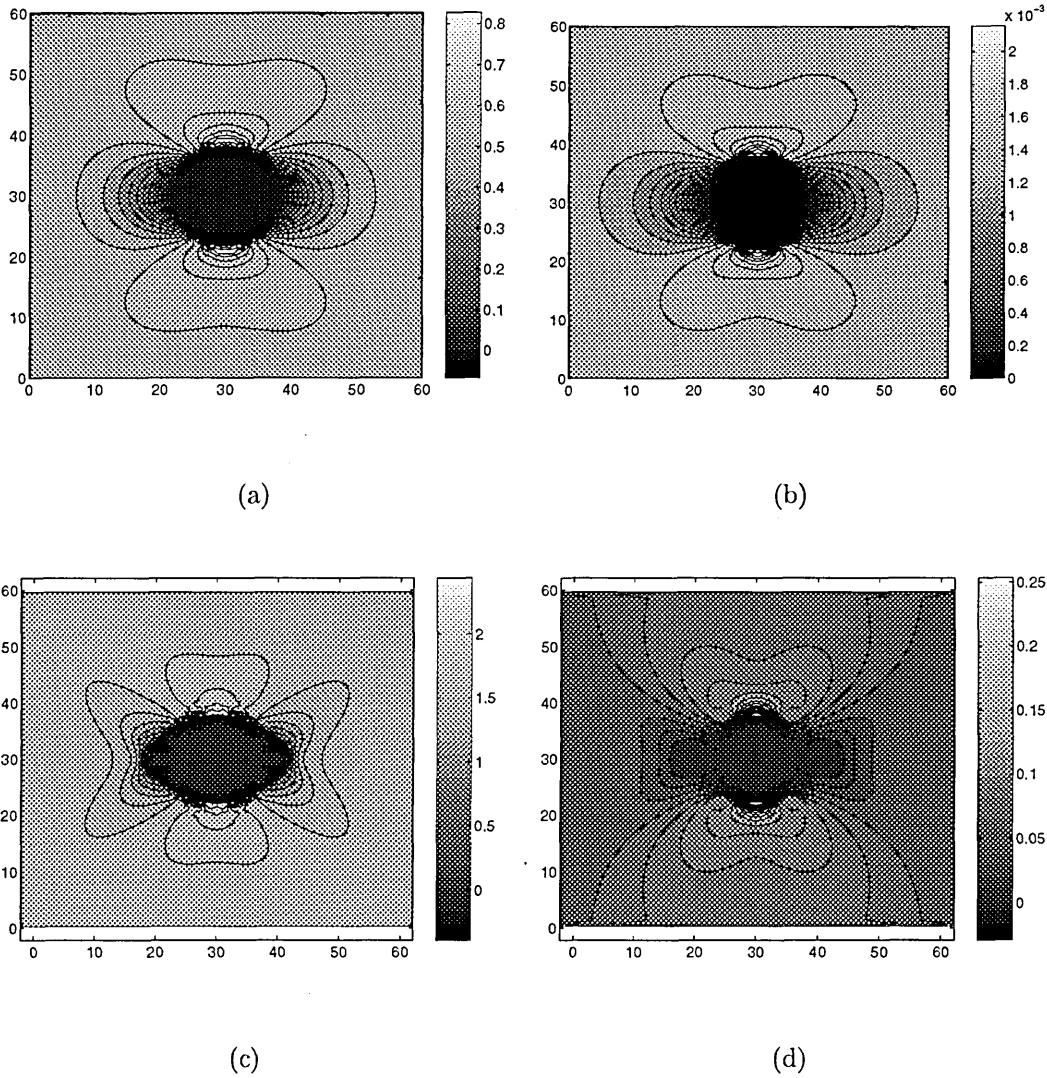
Figure 6.6: 2D Contour plots, taken through the centre of the void, of non-dimensional (a) normal stress at an applied stress of $0.5\sigma_y$, (b) normal strain at an applied stress of $0.5\sigma_y$, (c) normal stress at an applied stress of $1.5\sigma_y$, and (d) normal strain at an applied stress of $1.5\sigma_y$; loading is in the horizontal direction.

of the stress within the particle, relative to the far field stress, is constant during the elastic regime and increases with plastic deformation. Stress reduction within the particle, near the particle interface, becomes increasingly severe with escalating applied stress. The strain field (figure 6.7b) reveals a large increase in concentration within the matrix, and decrease in the particle.

The transition between the MnS particle acting a stress relaxer, and acting as a stress concentrator, is evident in figure 6.8a. This transition may have important implications regarding the uncertainty concerning the interfacial strength of the MnS particle; i.e. which position on the particles surface initially exhibits debonding? The strain field (figure 6.8b) is originally greater within the particle, during elastic deformation, but as the matrix plastically deforms the fields becomes increasingly similar to those in the Fe3C particle.

The stress gathering capability was observed by Xu [58] to decrease in the incipient stages of plastic deformation and then continually increase with applied stress. The system considered by Xu corresponded to a silicon carbide particle in an aluminium matrix; a particle system has been considered here, where the particle to matrix ratio is 6.4, which is identical to that of Xu. The stress concentration within the particle decreases in a similar manner to that reported by Xu, were a region of intense plastic deformation essentially shields the particle (figure 6.9). The gradual increase in stress gathering capability reported by Xu is attributable to the functional form of the stress-strain curve. In the Hencky-Mises relation considered here the gradient continues to decrease, even after substantial plastic deformation, whilst it

Normal Stress.

(a)
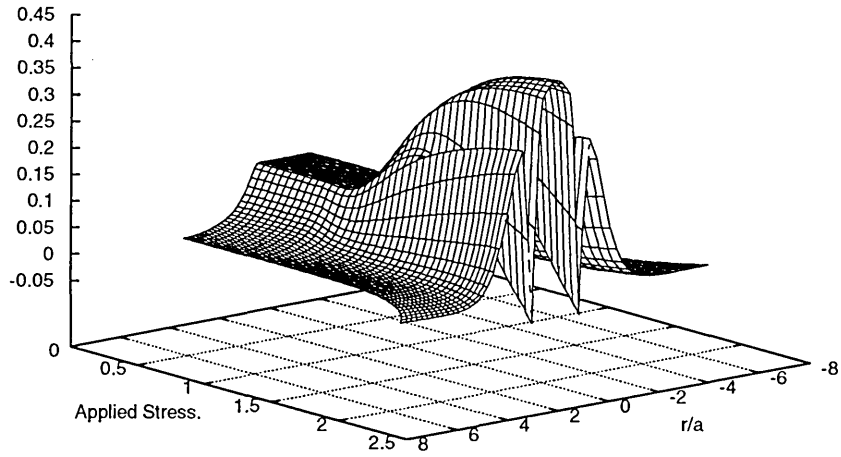
Normal Strain.
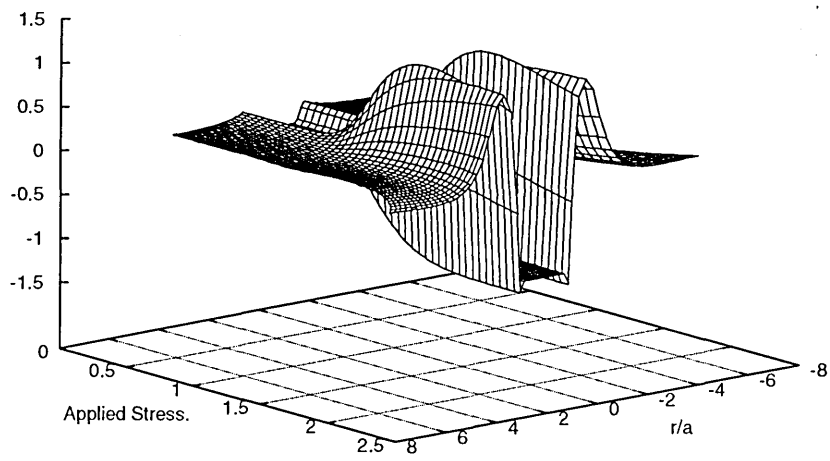
(b)

Figure 6.7: One-dimensional normalised (relative to far field) profiles of the (a) normal stress and (b) normal strain fields along the tensile polar axis, with increasing applied stress are presented for a Fe3C particle.

Normal Stress.

(a)
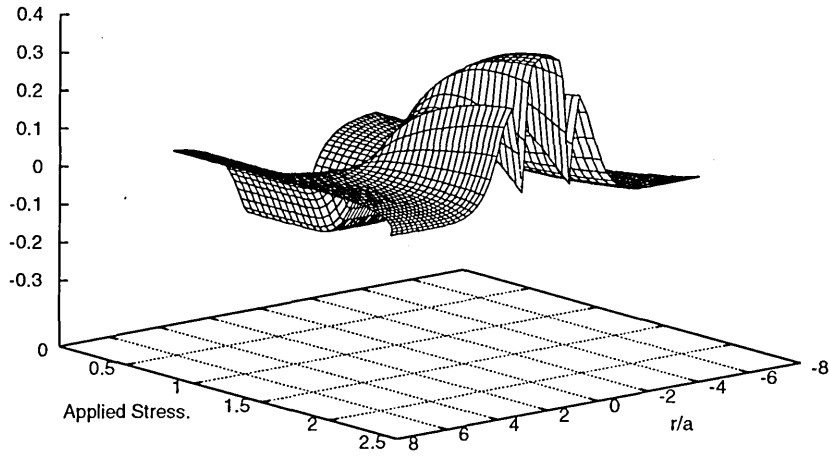
Normal Strain.
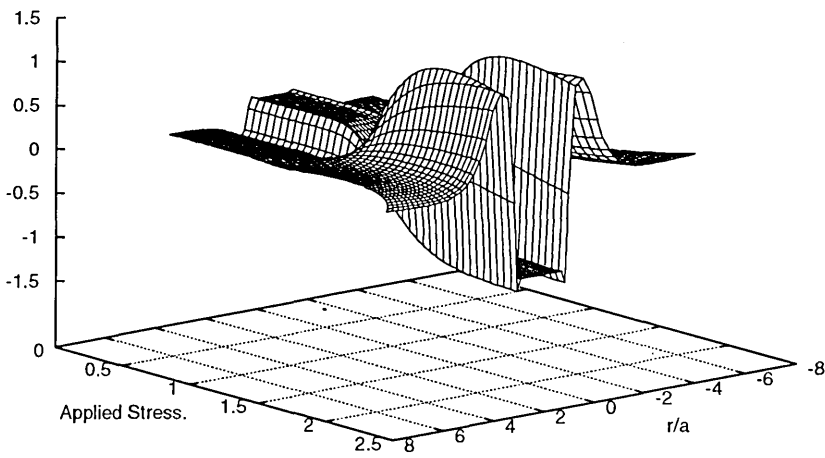
(b)

Figure 6.8: One-dimensional normalised (relative to far field) profiles of the (a) normal stress and (b) normal strain fields along the tensile polar axis, with increasing applied stress are presented for a MnS particle.

is suspected that the relation considered by Xu approaches a constant gradient.

Two systems are considered: the first possesses matrix characteristics which are non-linear and obey the Hencky-Mises relation, whilst the second initially follows the same relation but at some point ($\sigma = 2\sigma_y$) is assumed to exhibit linear hardening characteristics (see inset of figure 6.9). The particle embedded in the non-linearly hardening matrix is continually shielded by a region of much greater plastic deformation, with respect to the rest of the matrix, and therefore does not exhibit a gradual increase in stress concentration with large plastic deformation. In contrast, the particle embedded in the linearly hardening matrix experiences an increase in stress concentration, as with increasing deformation the matrix essentially possesses similar behavior throughout the system. Therefore the particle is no longer shielded by a region of intense plastic deformation, but is still unable to deform to the same extent as the surrounding matrix, hence a steady increase in the stress concentration factor.

6.1.1 Summary.

Regions where deformation fields are concentrated, and the magnitudes of these concentrations, due to both the misfits in elastic properties between the particle and matrix, and the ensuing variations in plastic deformation, have been identified as a function of applied stress. It was observed that the system considering a Fe3C particle possessed both stress and strain concentrations at the poles of the particle in the tensile direction, the system containing a void possessed stress and strain
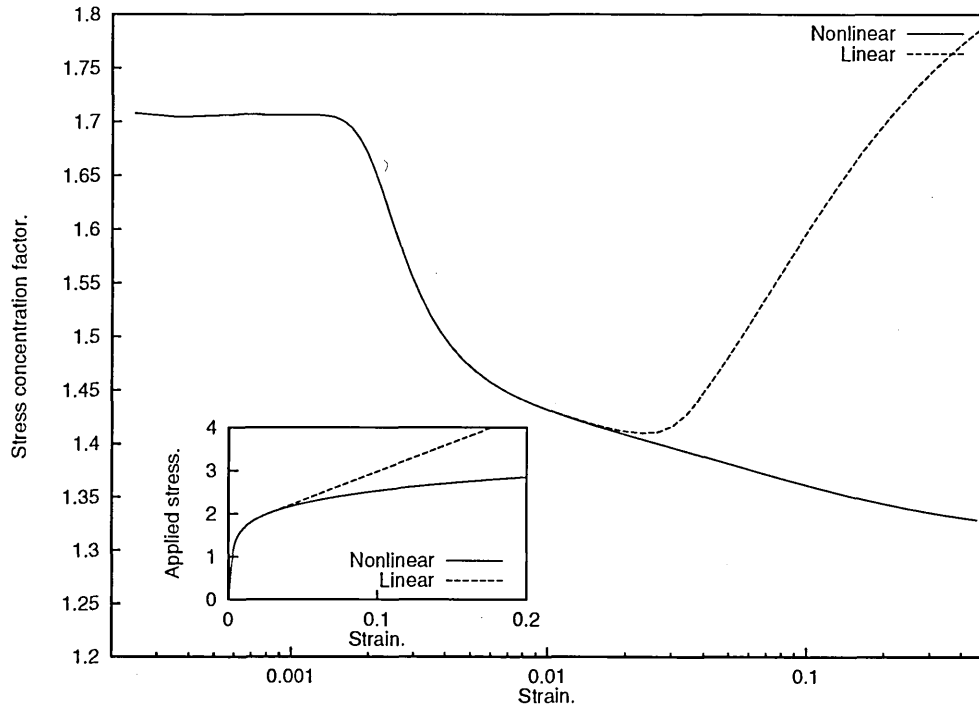
Figure 6.9: One-dimensional normalised (relative to far field) profiles of the normal stress fields along the tensile polar axis, for both non-linearly and linearly hardening materials, are presented; the particle elastic moduli is 6.4 times greater than the matrix elastic moduli. The stress-strain bexaviour for both materials are also presented.

concentrations in the equatorial plane, whilst the system containing a MnS particle exhibited a variation in the regions of stress and strain field concentrations with increasing plastic deformation.

The stress fields within a particle, whilst being initially uniform in the elastic regime, become increasingly irregular with the onset, and intensification, of plastic deformation. Whilst the normal stress perturbations along the polar axis have been previously observed in the literature [1, 53], the stress concentrations in the equatorial plane, and the radial concentrations in the equivalent stress contours, would appear to be undocumented.

6.2 Particle decohesion and fracture.

This section considers the fracture of particles, and their decohesion from the steel matrix. It should be noted that the results presented here invariably lack symmetry, although the original deformation fields are symmetric. The reason for this is the quasi-static definition of fracture in the current model; only a single fracture surface may be created at a given iteration for a given criteria. It is therefore impossible for fracture to simultaneously occur on both sides of the simulation (although similiar fracture characteristics may occur sequentially). The only alternative would be to vary the number of surfaces to be created in a given iteration in order to reflect the symmetry of the system.

The study of interfacial decohesion of both a Fe3C and a MnS spherical particles, of radius 5.5 unit lengths in a three-dimensional system of 41^3 nodes, are now presented; the special case of a spherocylindrical MnS particle was also investigated. The damage algorithm, resulting in the removal of bonds, has been described in section 4.3, and the constituent properties given above. The definition of damage in this study is taken to be the number of bonds broken in the simulation.

The broken bonds, normal stress and normal strain fields depicting the interfacial decohesion of a Fe3C particle are considered in figures 6.10 and 6.11. In the previous section the stress concentrations concerning the deformation of a Fe3C particle were investigated, and in figure 6.10a the initial debonding at the polar regions of the particle interface in the tensile direction is observed. The consequent loss of

stress carrying capability at these damaged regions has resulted in stress and strain concentrations in the matrix, ahead of the propagating cracks.

The crack, although developing, cannot be described as catastrophic as it is still required for the applied stress to be increased in order for the crack to progress. In figure 6.10b the applied stress has reached a maximum of $1.69\sigma_y$, for this simulation, and this is illustrated by the growth of the crack into the matrix. Once a crack extends into the matrix it can generally be considered catastrophic, in the present model, as the crack tip does not possess the ability to blunt.

The larger crack extension on the left side of the particle has resulted in intensified stress and strain concentrations in this region; this is now the dominant source of crack advancement. In a symmetrical system the choice of region, where fracture is initiated, is a consequence of the quasi-static nature of the damage algorithm, and rounding error variations between the breaking criterion in differing regions.

The ductile growth of the crack into the matrix and the more extensive continuation of interfacial debonding occur simultaneously in this model, as can be seen in figures 6.11. The interfacial decohesion over almost the entire left side of the particle has resulted in stress and strain concentrations above and below the particle, making the particle increasingly redundant to crack growth. In figure 6.11b the crack advancement no longer consists of interfacial decohesion and progresses entirely through the ductile fracture of the surrounding matrix.
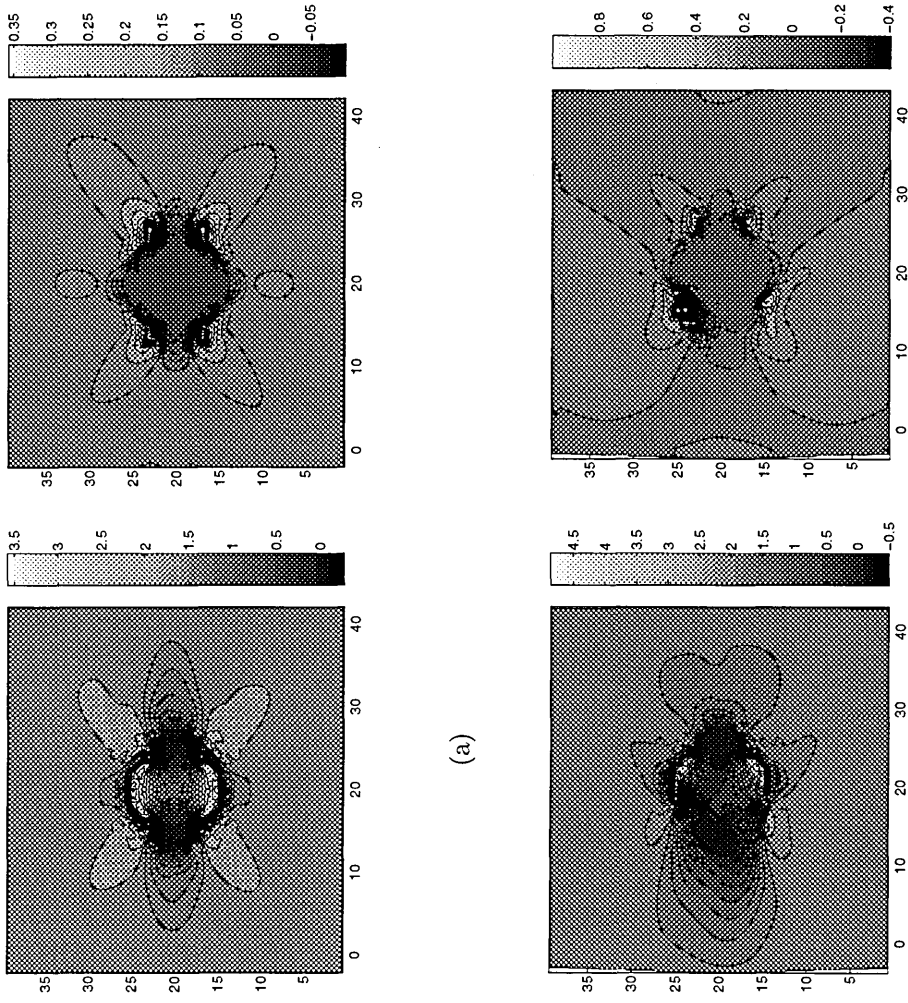
Figure 6.10: The broken bonds (left), 2D normal stress contours (centre), and 2D normal strain contours through the Fe3C particle centre are presented for two stages of the simulation; (a) applied stress is $1.61\sigma_y$ and damage is 338, (b) applied stress is $1.69\sigma_y$ and damage is 1051.
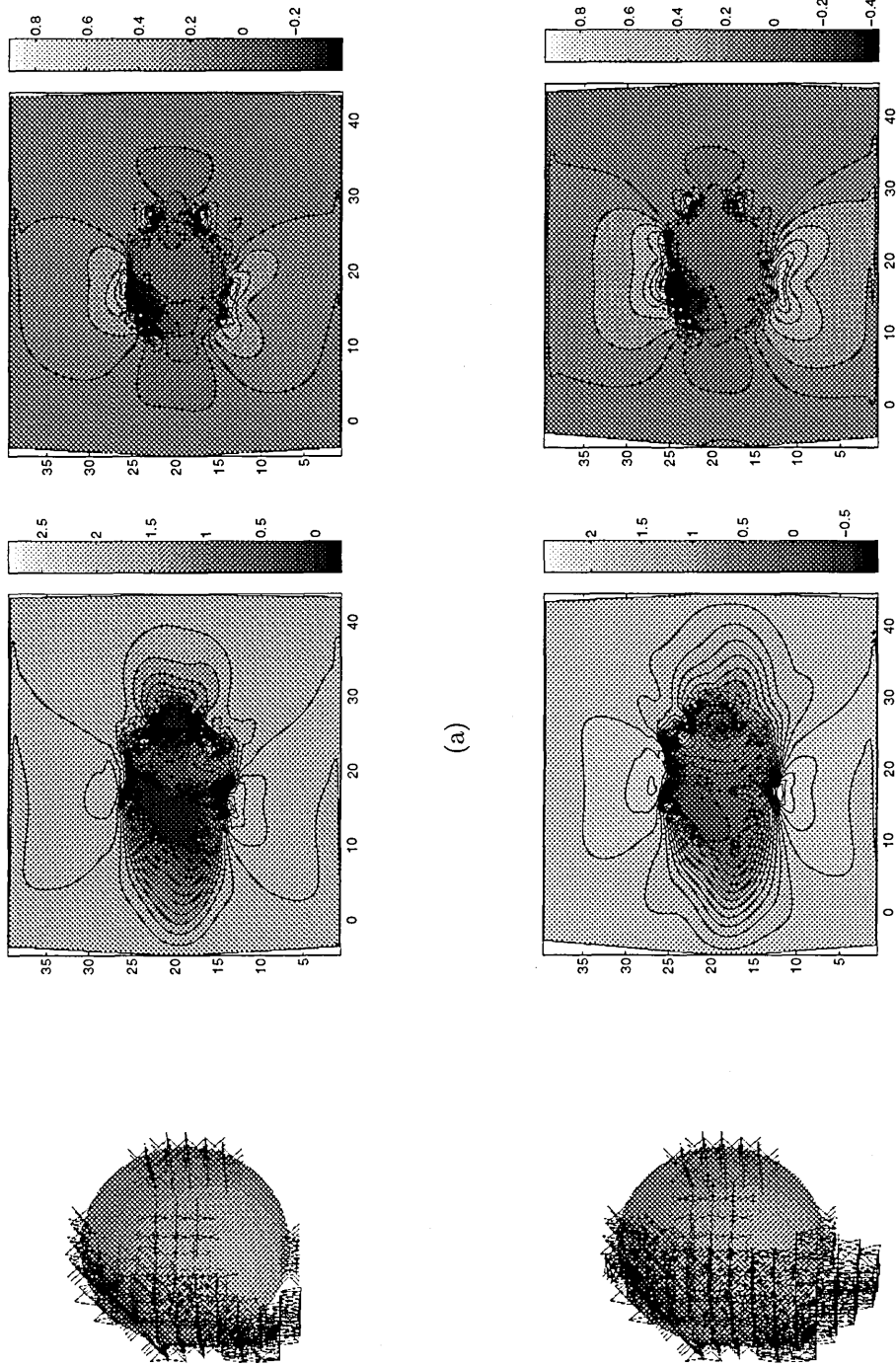
Figure 6.11: The broken bonds (left), 2D normal stress contours (centre), and 2D normal strain contours through the Fe3C particle centre are presented for two stages of the simulation; (a) applied stress is $1.69\sigma_y$ and damage is 1918, (b) applied stress is $1.69\sigma_y$ and damage is 3004.

It should be noted that the particle remains partially coupled to the matrix; the deformation required to separate the particle from the matrix is sufficiently severe to allow the propagating crack to extend into the surrounding matrix prior to complete particle debonding.

The interfacial strength of a MnS particle is considered lower than that of a Fe3C particle, and therefore the separation of the particle and matrix begins at the lower applied stress of $1.29\sigma_y$ (figure 6.12a). The initial debonding occurs in the same regions; at the poles of the particle, in the tensile direction. It should be noted here that the interfacial strength of the MnS particle is questionable (the interfacial strength of an elongated particle from [35] is assumed here), therefore debonding may occur at a different level of applied stress. If the interfacial strength was found to be less than the yield stress of the matrix, then debonding may occur at the particle surface in the equatorial plane.

In figure 6.12a the initial debonding once more produces stress and strain concentrations in regions perpendicular to the tensile direction, and adjacent to the damaged regions. In the present simulation, the deformation fields associated with initial interfacial decohesion are not large enough for ductile fracture to be initiated in the matrix, and in figure 6.12b the crack is shown to propagate along the particle-matrix interface.
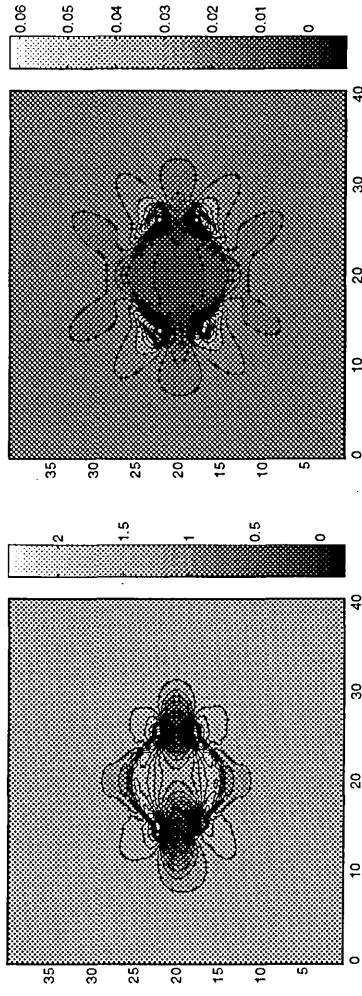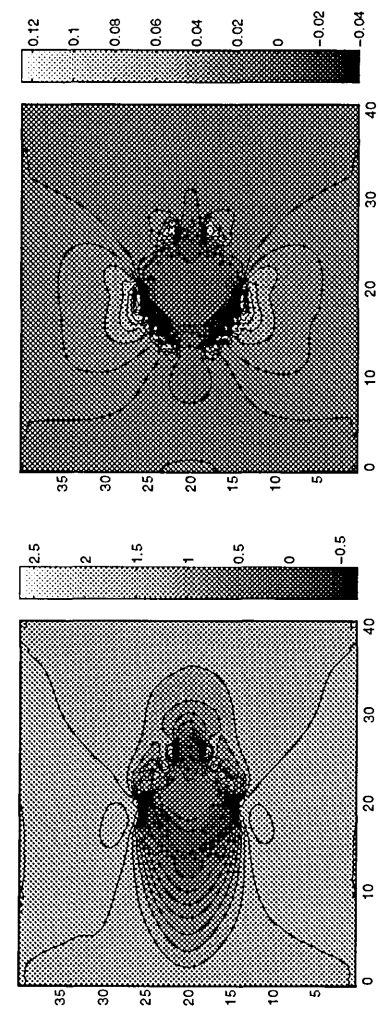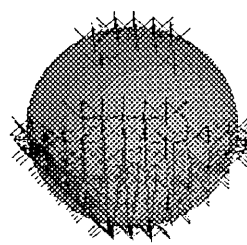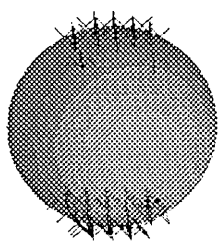
Figure 6.12: The broken bonds (left), 2D normal stress contours (centre), and 2D normal strain contours through the MnS particle centre are presented for two stages of the simulation; (a) applied stress is $1.29\sigma_y$ and damage is 224, (b) applied stress is $1.3\sigma_y$ and damage is 969.
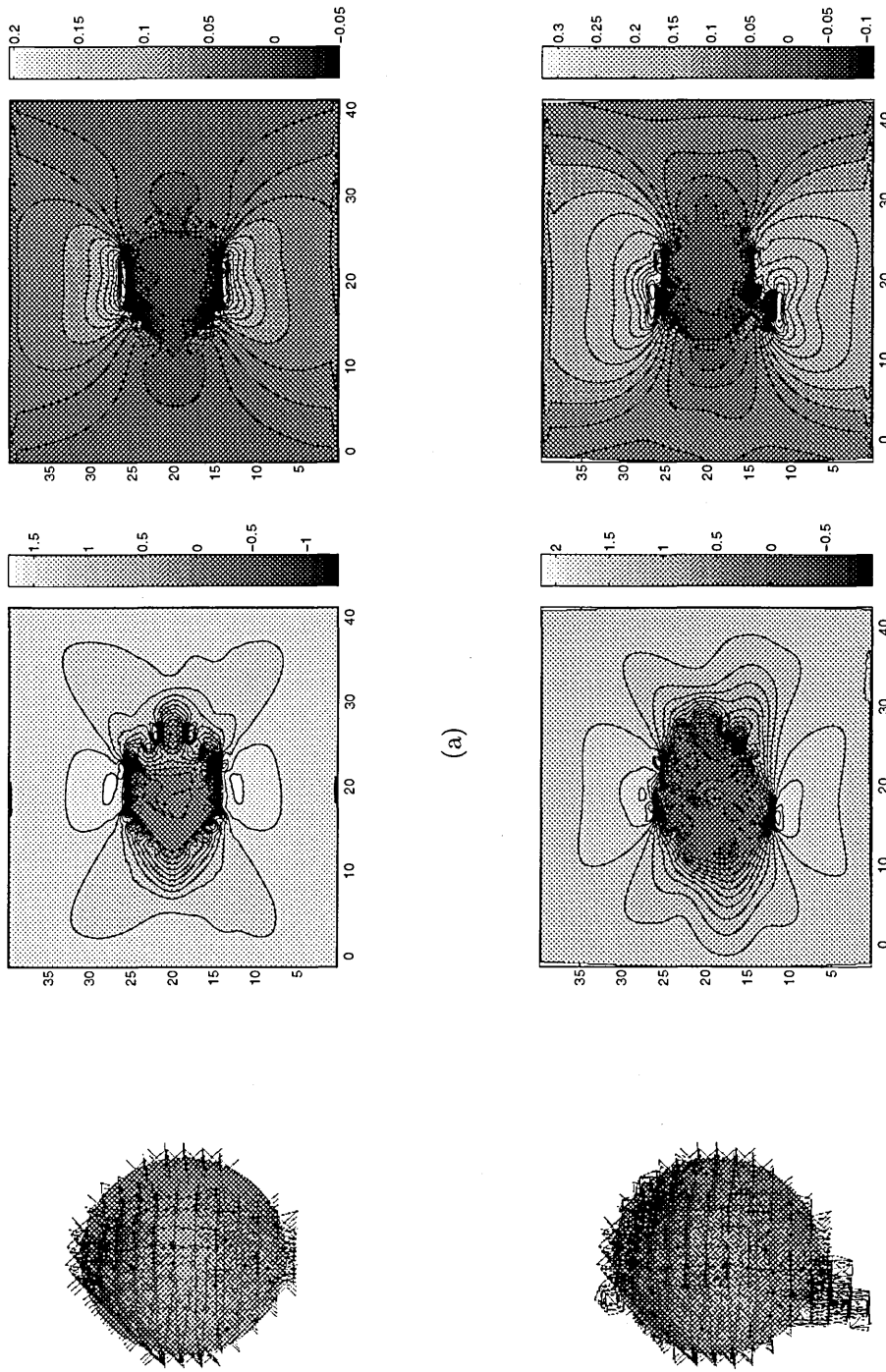
Figure 6.13: The broken bonds (left), 2D normal stress contours (centre), and 2D normal strain contours through the MnS particle centre are presented for two stages of the simulation; (a) applied stress is $1.45\sigma_y$ and damage is 2099, (b) applied stress is $1.58\sigma_y$ and damage is 3740.

The largest concentrations in the stress and strain fields, whilst occurring above and below the particle, are not large enough for the crack to propagate into the matrix. The stresses within the particle, and at the regions of the interface still connecting the particle with the matrix, and are not sufficiently pronounced to allow further particle decohesion. Therefore the applied stress is permitted progressively to increment; as it does, the interfacial regions, while not comprising the most stressed or deformed regions of the simulation, increasingly satisfy the local failure criterion and in figure 6.13a the particle can be observed to be almost completely debonded.

The stage of the simulation depicted in figure 6.13a is more analogous to the simulation of a void; although the effects of interfacial decohesion have had a detrimental consequence, as the strength of a similar system containing a void is $1.67\sigma_y$, whilst the current simulation reaches a maximum stress of 1.58. This level of stress is attained at the stage of the simulation depicted in figure 6.13b, which shows the incipient stages of crack propagation into the matrix.

The common case of an elongated MnS is now investigated. The particle is assumed to be a spherocylindrical and possesses a radius of 2.5 unit lengths in the transverse direction and a half-length of 15.5 unit lengths in the longitudinal direction. The system size reflects the elongated nature of the inclusion and is $71 \times 25 \times 25$ nodes.

Prior to damage accumulation and plastic deformation the particle is capable of deforming to a greater extent than the matrix, whilst with the onset of plastic deformation the situation is reversed. Figure 6.14 shows the normal stress and normal strain fields for applied stresses of 0.9 and 1. An important feature is the
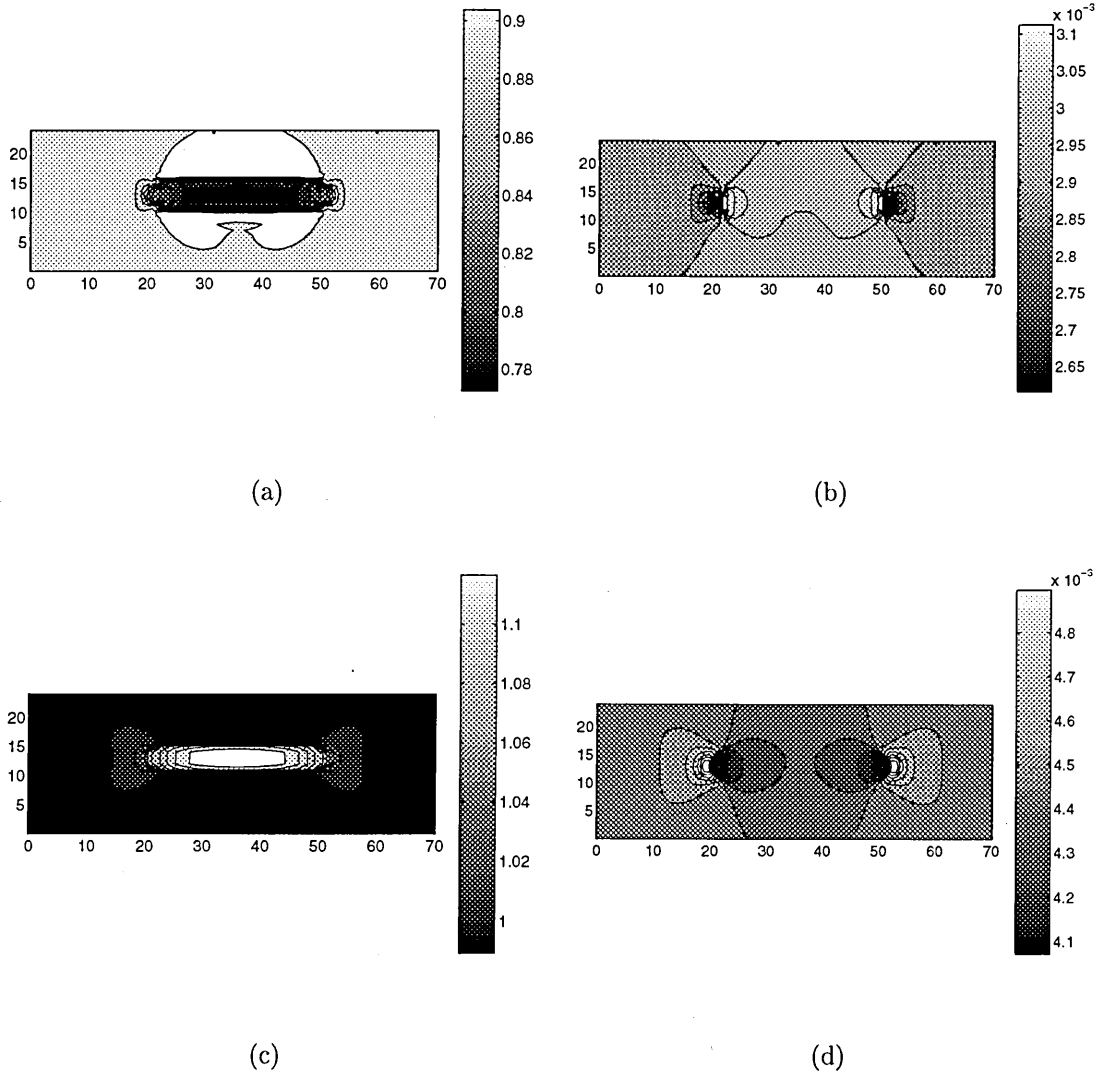
Figure 6.14: 2D Contour plots, taken through the spherocylindrical MnS particle centre, of non-dimensional (a) normal stress at an applied stress of $0.9\sigma_y$, (b) normal strain at an applied stress of $0.9\sigma_y$, (c) normal stress at an applied stress of σ_y, and (d) normal strain at an applied stress of σ_y; loading is in the horizontal direction.

100

manner in which the normal stress, subsequent to plastic deformation, displays a peak in the centre of the particle.

The broken bonds, normal stress and normal strain fields associated with the ensuing fracture of the longitudinally elongated MnS particle are given in figures 6.15 and 6.16. The stress concentration at the centre of the particle is responsible for initiating fracture of the particle at this point (figure 6.15a). The crack is capable of propagating through the particle until it reaches the matrix, when it would appear to be arrested. The resultant stress field reveals two peaks; the two halves of the fractured particle both concentrating stresses in their centres. Fracture is initiated in these regions, upon applied stress elevation, as can be observed in figure 6.15b, and the particle bifurcates into four segments. Once more the cracks are arrested upon reaching the matrix, and while the pre-existing cracks are allowed to become more damaged, no new cracks are initiated until the stress is incremented further.

In figure 6.16a the stress has been incremented to a level where internal fracture of the particle is allowed to occur once more; the particle now being comprised of six segments.

Eventually the strain in the matrix, adjacent to the cracked particle, is sufficiently large to enable crack propagation into the matrix and the fracture process is considered catastrophic. Similar phenomenon, concerning the internal cracking of elongated MnS particles, has been observed by Jaffrey [36]. Experimentally the particle is not a perfect sperocylinder, but the essential characteristics remain the same (figure 6.17).
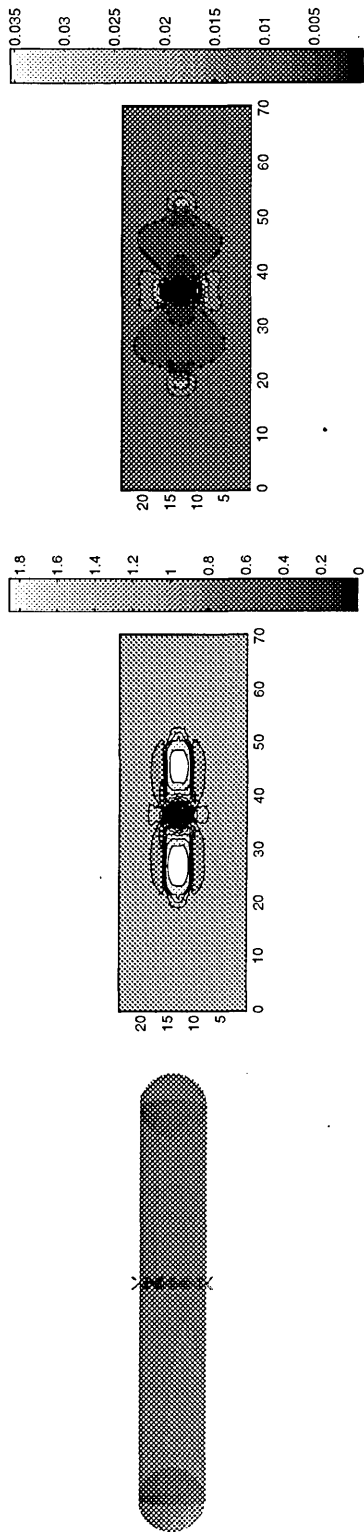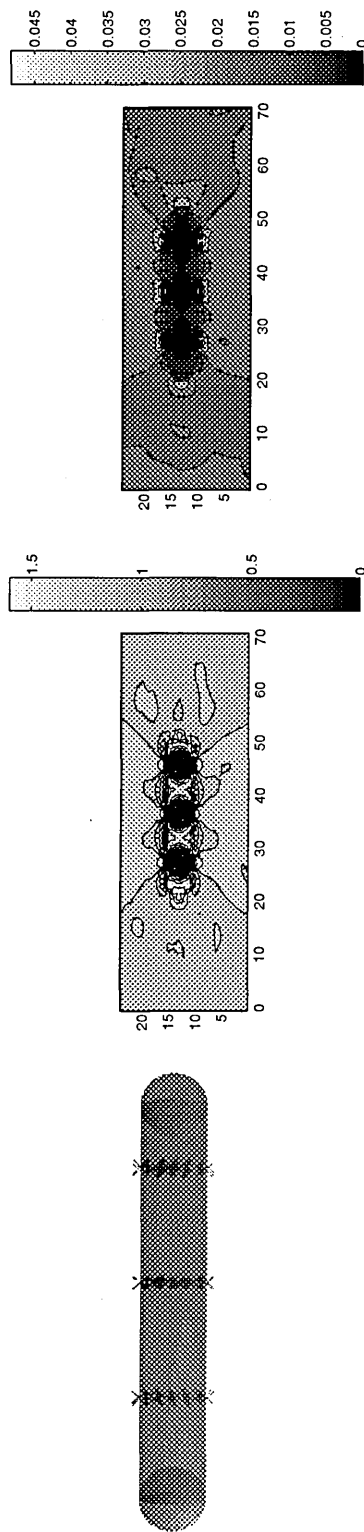
Figure 6.15: The broken bonds (left), 2D normal stress contours (centre), and 2D normal strain contours through the spherocylindrical MnS particle centre are presented for two stages of the simulation; (a) applied stress is $1.19\sigma_y$ and damage is 125, (b) applied stress is $1.23\sigma_y$ and damage is 375.
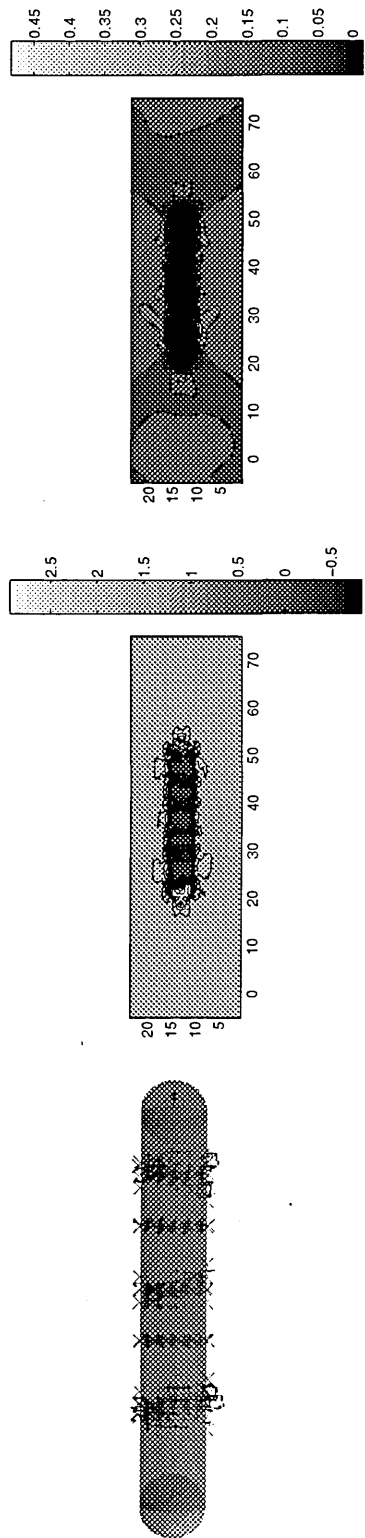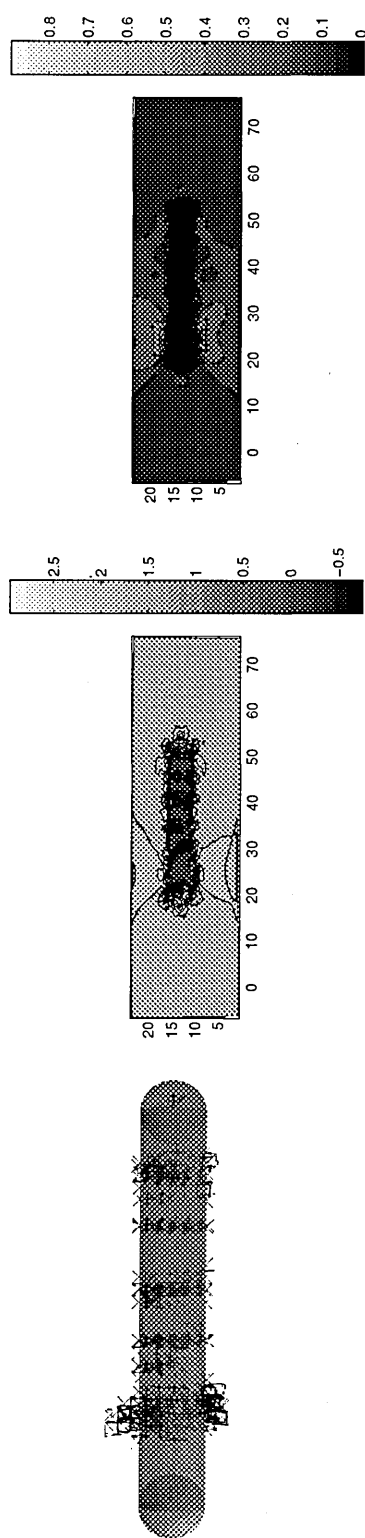
Figure 6.16: The broken bonds (left), 2D normal stress contours (centre), and 2D normal strain contours through the spherocylindrical MnS particle centre are presented for two stages of the simulation; (a) applied stress is $1.68\sigma_y$ and damage is 1317, (b) applied stress is $1.69\sigma_y$ and damage is 2173.

103
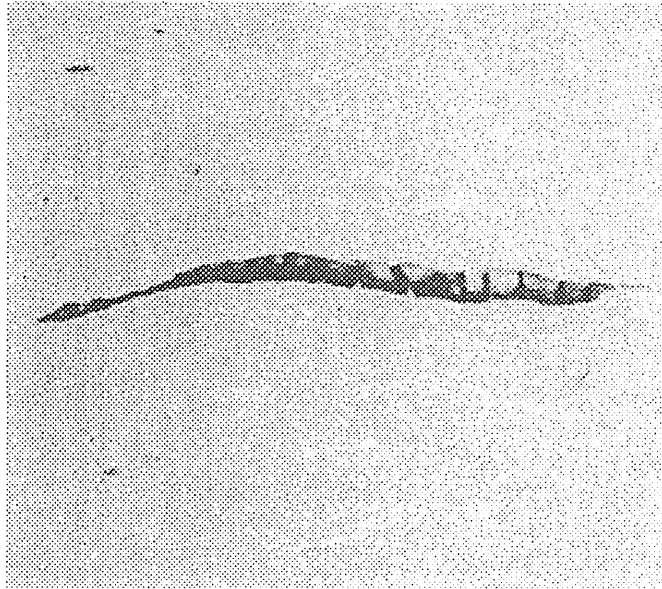
Figure 6.17: A large MnS stringer showing multiple transverse cracking; taken from Jaffrey [36].

The effects of varying the aspect ratio of an elongated MnS particle upon the bifurcation characteristics of the internal fracture are investigated. Systems considering MnS spherocylindrical particles whose radii in the transverse direction are 2 unit lengths, whilst the longitudinal half-lengths are 4, 8, and 16 unit lengths are considered; representing aspect ratio's of 2, 4, and 8 unit lengths. The simulations consist of $61 \times 21 \times 21$ nodes.

The relative one-dimensional stress profiles through the centre of the particle in the tensile (longitudinal) direction are presented in figure 6.18, for both an applied stress above and below the yield stress. It is observed that the longer particle exhibits a more severe influence on the stress field perturbations, especially in the presence of plasticity, where the stress concentration in the centre of the particle increases. The increase in stress concentration in the centre of the more elongated particle results
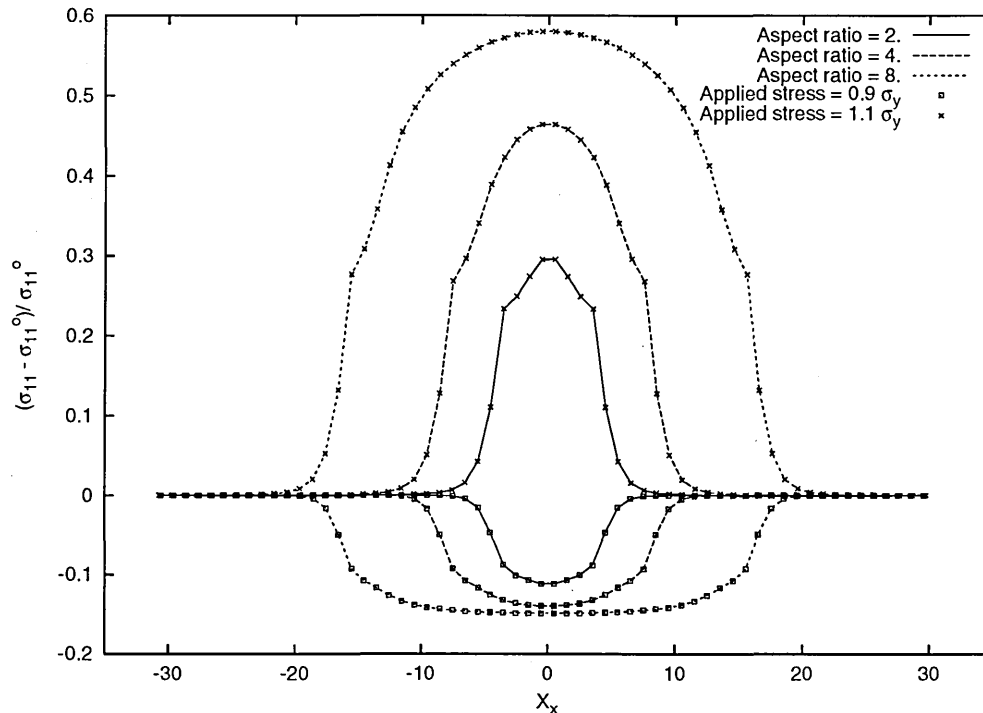
Figure 6.18: The relative one-dimensional stress profiles through the centre of the particle in the tensile direction. Applied stresses above ($\sigma = 1.1\sigma_y$) and below ($\sigma = 0.9\sigma_y$) the yield stress are considered.

in internal cracking occuring at lower levels of energy in the system (figure 6.19); the subsequent damage accumulation is substantially greater in the longer particle.

The internal fracture in the particle, whose aspect ratio is two, is given in figure 6.20a along with the accompanying stress field. The crack arrests at the matrix interface subsequent to the propagation of an internal crack through the centre of the particle. With increased energy in the system the particle experiences increased damage accumulation about the internal crack, and surrounding particle-matrix interface, before catastrophically failing (figure 6.20b).

The system containing a particle, whose aspect ratio is four, is again observed inter-
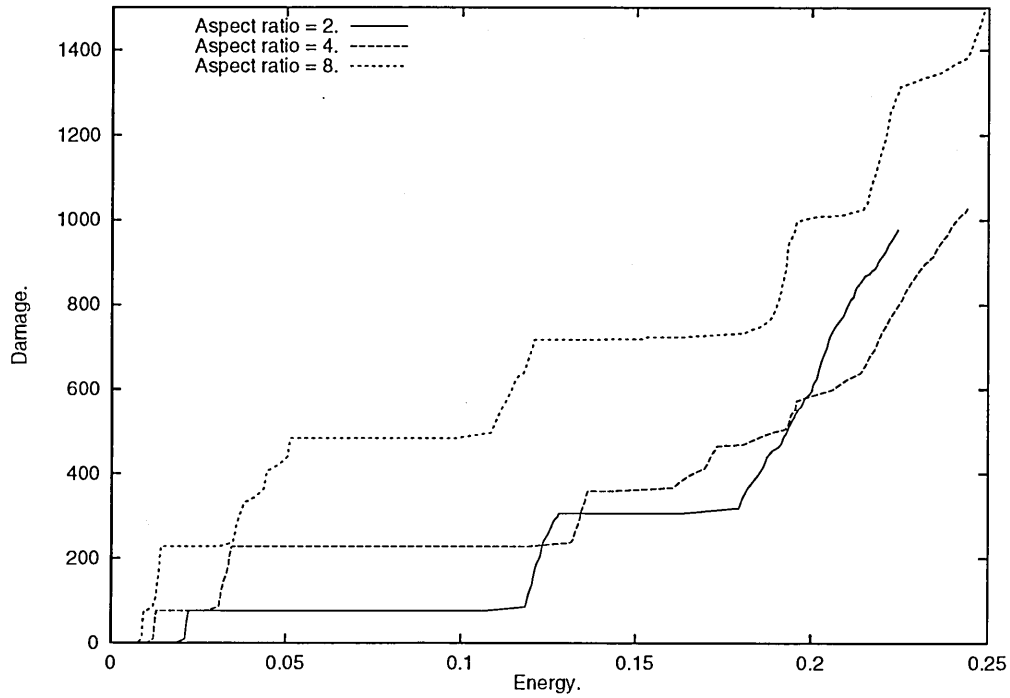
Figure 6.19: The damage accumulated (broken bonds) as a function of the energy absorbed (integration of the stress-strain curve) for various particle aspect ratio's. The particles are elongated in the tensile direction. The arrows indicate the energy absorbed prior to catastrophic failure.

(a)

(b)
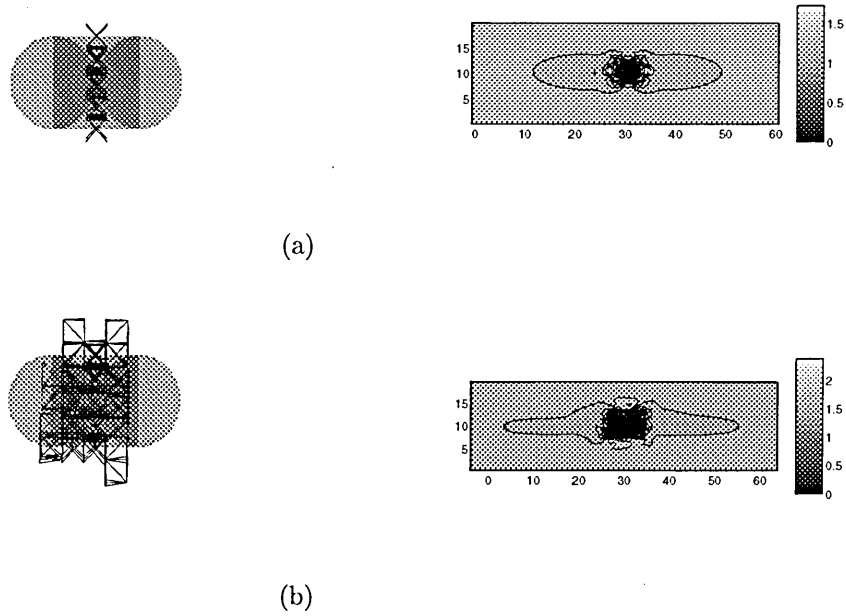
Figure 6.20: The broken bonds (left), and 2D normal stress contours through the centre of the elongated MnS particle (right) are presented for two stages of the simulation; (a) applied stress is $1.28\sigma_y$ and damage is 76, (b) applied stress is $1.66\sigma_y$ and damage is 456. The particle aspect ratio is two.

nally to fracture through the particle centre, although at a lower level of absorbed energy, than in the previous system. The particle experiences further internal fracture; the particle bifurcates into four sections as depicted in figure 6.21. Internal fracture does not subsequently occur, with increasing energy, until the previously cracked regions become increasingly damaged and the propagating fracture spreads catastrophically into the matrix (figure 6.21c).

Considering the particle, of aspect ratio equal to eight, the internal fracture follows a similar pattern as before, with the particle fracturing into first two and then four segments as depicted in figure 6.22a; the further increase in particle fracture can be observed in figures 6.22b and 6.22c. The particle is observed to undergo further internal cracking, into eight segments, at relatively low levels of energy (≈ 0.05),

107
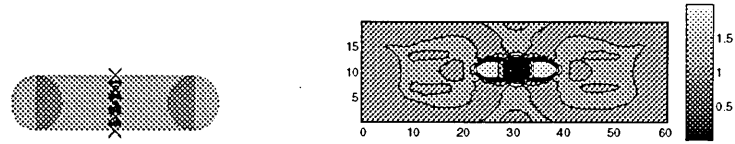
(a)
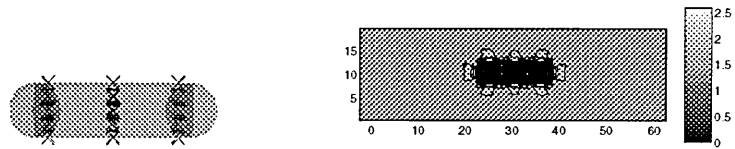
(b)
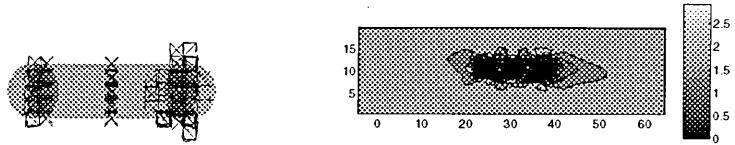
(c)

Figure 6.21: The broken bonds (left), and 2D normal stress contours through the centre of the elongated MnS particle (right) are presented for two stages of the simulation; (a) applied stress is $1.26\sigma_y$ and damage is 76, (b) applied stress is $1.58\sigma_y$ and damage is 228, (c) applied stress is $1.68\sigma_y$ and damage is 734. The particle aspect ratio is four.

(a)

(b)

(c)
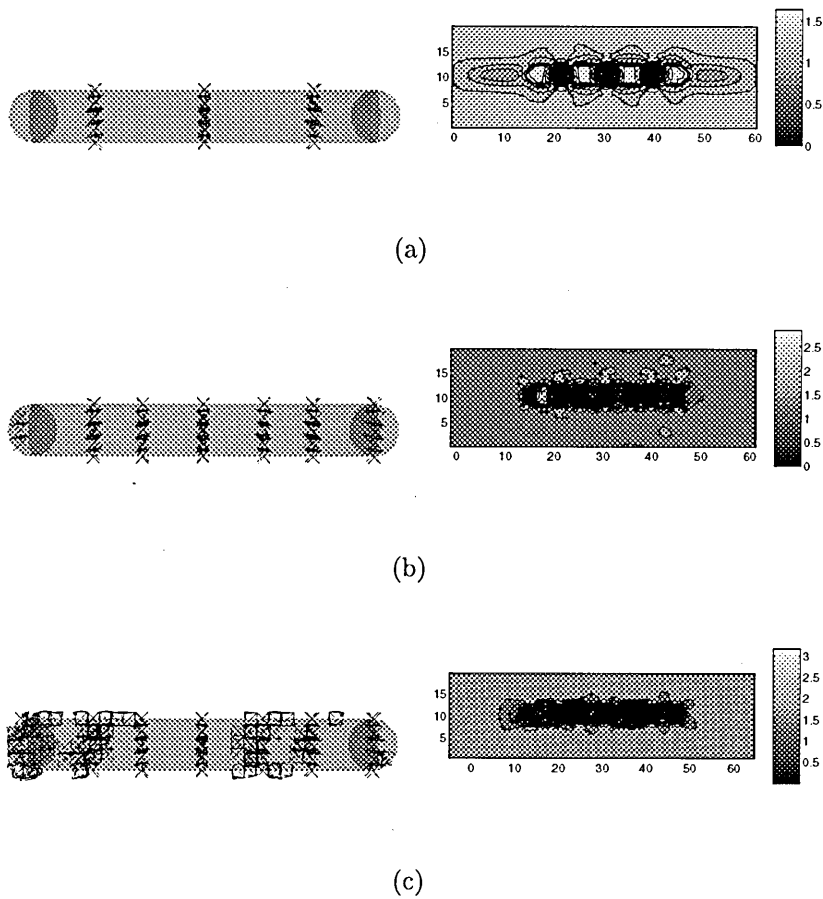
Figure 6.22: The broken bonds (left), and 2D normal stress contours through the centre of the elongated MnS particle (right) are presented for two stages of the simulation; (a) applied stress is $1.2\sigma_y$ and damage is 228, (b) applied stress is $1.4\sigma_y$ and damage is 484, (c) applied stress is $1.7\sigma_y$ and damage is 1368. The particle aspect ratio is eight.

although with increased levels of energy, extensive damage is observed within the particle, about the internal cracks and at the particle-matrix interface.

The energy absorbed prior to catastrophic failure increases with increased aspect ratio, even though the initially higher levels of internal stress cause premature internal particle fracture. The increased number of resultant concentrators (internal cracks) would appear to have less influence on the local deformation fields; this may be a consequence of mutual shielding effects between the internal cracks.

109

6.2.1 Summary.

The initial fracture characteristics have been elucidated for systems containing both Fe3C and MnS particles. The propensity of weakly bonded spherical MnS particles to debond with significantly lower levels of applied stress, than systems considering strongly bonded Fe3C particles, was observed. The Fe3C particle only exhibited partial interfacial decohesion whilst the MnS particle completely debonded. The increased level of applied stress in the Fe3C particulate system, subsequent to void nucleation, indicates a higher strength and ductility in such systems. The transverse cracking of an elongated MnS, orientated parallel with the tensile direction has been successfully replicated in the current model. An investigation into the consequence of varying the particle aspect ratio of elongated particles indicates that the longer particles are substantially less deleterious. In real systems more elongated particles may be expected to have higher levels of internal damage, assosciated with the material processing, and therefore might not display the same characteristics observed here.

6.3 Interactions between two voids.

The effects of orientation and distance between two voids, of radius 2.5 unit lengths, upon the resultant fracture characteristics, are now investigated. The ductile fracture criterion in the current model is the attainment of a critical strain, therefore the strain field is of principle importance in the potential coalescence of voids. Three

orientations of the two voids are considered: parallel, perpendicular and diagonal (45 degrees) alignments with respect to the tensile direction. The inter-void distances considered are 2, 5, and 10 unit lengths; the resulting strength and toughness of the systems are given in figure 6.23. The inter-void distances for the diagonal system do not correspond with the integer values given, as in order to maintain the same discretisation effects, the voids are always centred on lattice nodes. The diagonal inter-void distances correspond to 2.1, 4.9 and 9.1 unit lengths; this difference is assumed to be insignificant to the interpretation of trends. The effect of increas-
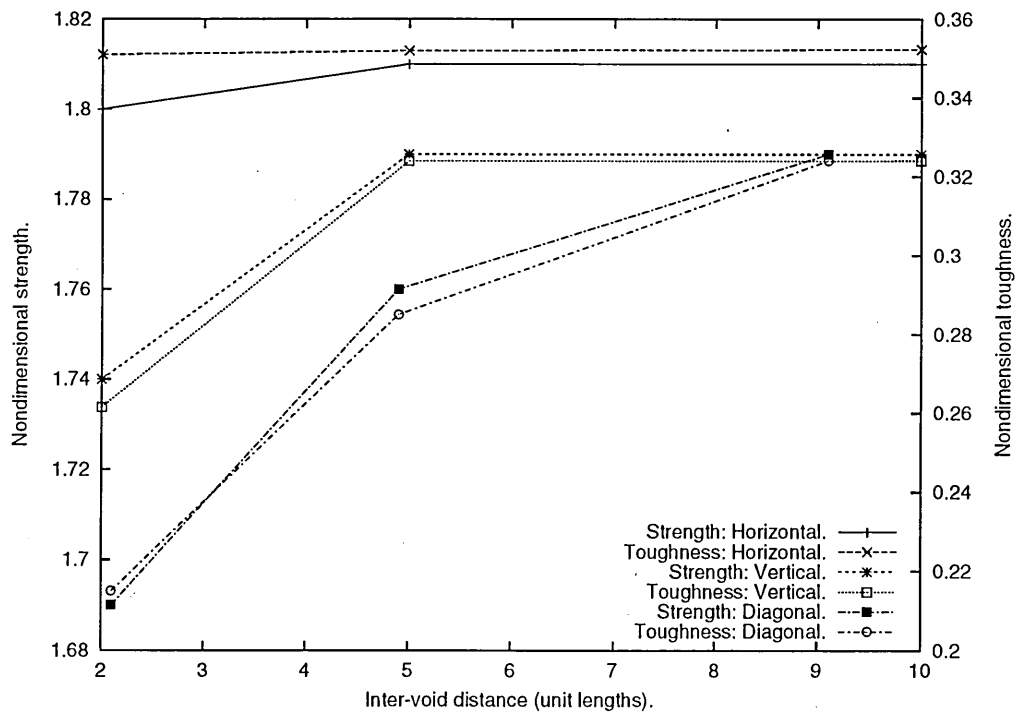

Figure 6.23: The nondimensional strength and toughness, for different void alignments, as a function of void separation. The tensile direction is considered to be horizontal.

ing the separation, between two voids orientated parallel with respect to the tensile direction, upon the normal strain field is shown in figure 6.24. The normal strain fields for void separations of 2 and 10 unit lengths are depicted, and the variation in

separation is seen to have little effect on the strain concentrations in the equatorial plane about the voids. When in close proximity, the voids are found to shield each other, but the resultant strength and toughness is insensitive to the separation.

(a)   (b)
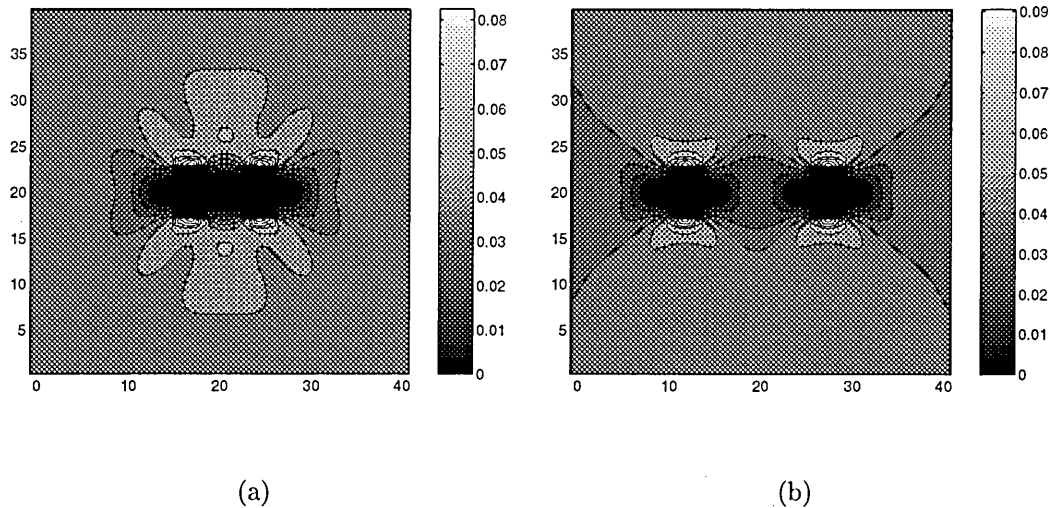
Figure 6.24: 2D Contour plots, taken through the centre of both voids (aligned parallel to tensile direction), of non-dimensional normal strain for void separations of (a) 2 and (b) 10 unit lengths. The applied stress, in the horizontal direction, is $1.4\sigma_y$.

The effects of void separation upon either the crack morphology, or the toughness and strength of the system, is found to be inconsequential. The broken bonds and normal strain fields depicting the growth of one of the voids (separated by 2 unit lengths) are given in figure 6.25; similar results are found for systems of increased void separation. The regions in the equatorial planes of the two voids, in close proximity to the voids, satisfy the critical strain based criterion, and therefore a fracture surface is created, at one of the voids, in such a region. The crack would rather propagate through the extension of this newly formed fracture surface than create new surfaces, either about the void currently growing or the alternative void.

As the void grows the strain concentrations associated with this crack propagation increase, and the effects of the second particle, being initially negligible, become redundant.

The effects of orientating voids perpendicular, with respect to the tensile direction, are now considered. The stress and strain concentrations that exist in the equatorial plane of a void are potentially reinforced, as both voids share their equatorial plane. This is depicted in figure 6.26, where the strain fields for two undamaged systems, containing two voids separated by distances of 2 and 10 unit lengths, are presented. In the case where the voids are in close proximity the strain field exhibits a strong concentration between the two voids.

The subsequent damage, initiated in the system considering the two voids in close proximity, is shown in figure 6.27. The voids coalesce (figure 6.27a), and the growth of the resultant void occurs (figures 6.27b and 6.27c). The plane of fracture remains the equatorial plane of the two voids, and the growth of the single resultant void progresses catastrophically. The initial strain concentration between the two voids has a detrimental effect upon the system, as indicated by the resultant decrease in toughness and strength.

The broken bonds and normal strain field for a system containing two voids orientated perpendicular to the tensile direction, but separated by a distance of 5 unit lengths is condidered in figure 6.28. In figure 6.28a the crack begins to propagate from the upper void down towards the second void. This is not thought to be a consequence of intrinsic void coalescence in the system, as in figure 6.28b the crack can be seen

113
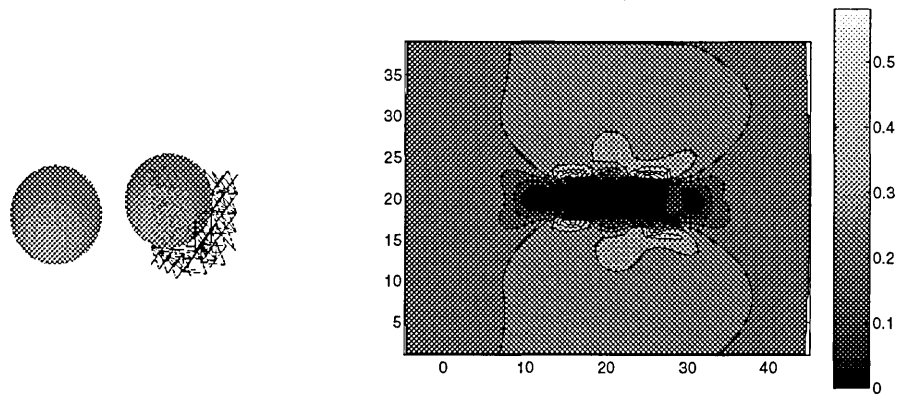
(a)
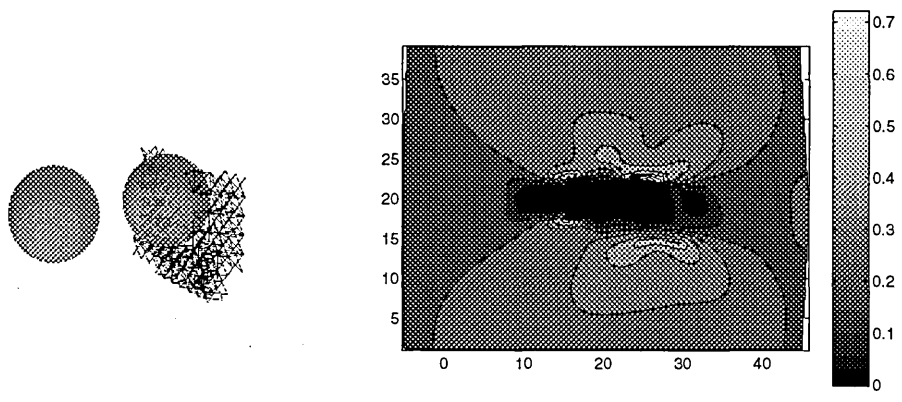
(b)
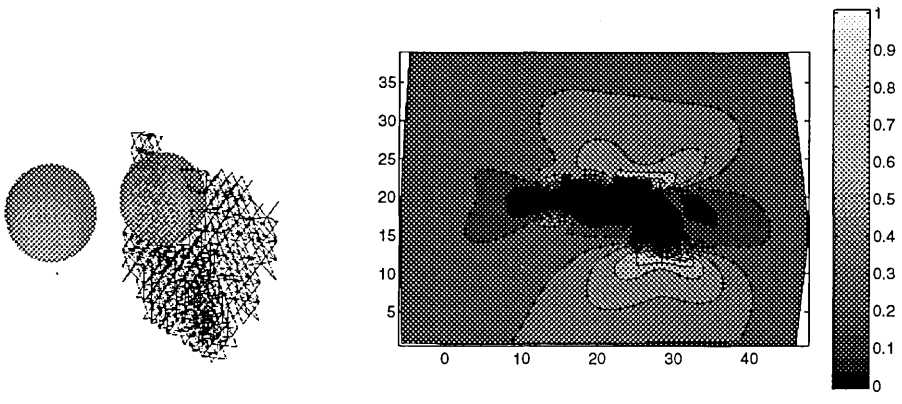
(c)

Figure 6.25: The broken bonds (left), and 2D normal strain contours through the centre of both voids (aligned perpendicular to tensile direction with avoid separation of 2 unit lengths), are presented for three stages of the simulation; applied stress is $1.81\sigma_y$ and damage is (a) 228, (b) 574, and (c) 1268.
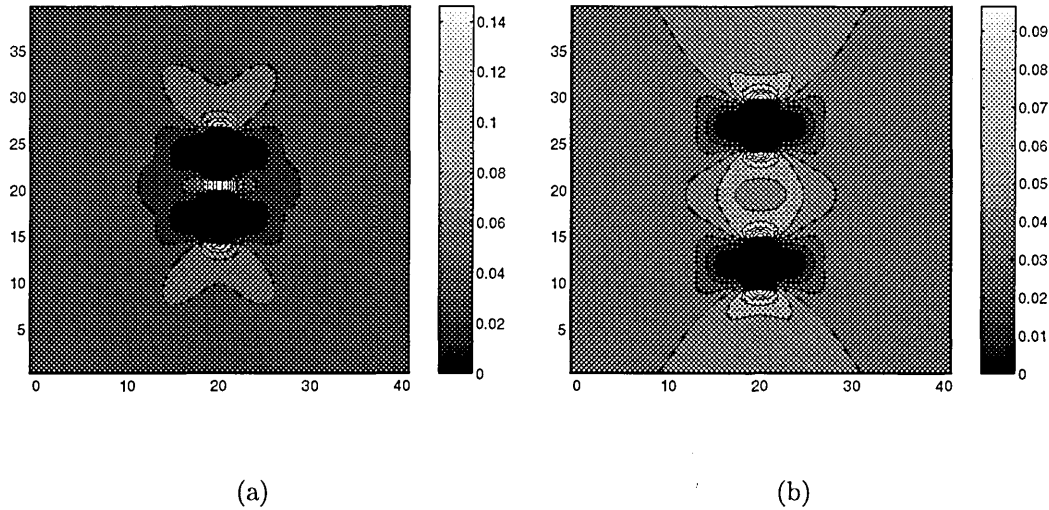
Figure 6.26: 2D Contour plots, taken through the centre of both voids (aligned perpendicular to tensile direction), of non-dimensional normal strain for a void separation of (a) 2 and (b) 10 unit lengths. The applied stress, in the horizontal direction, is $1.4\sigma_y$.

to propagate around the upper void, and propagate equally both towards the second void and away from it. The strain field at this stage of the simulation does show a concentration between the growing upper void and the static lower void. The crack propagating from the upper void now appears to coalesce with the second void, although the crack propagation is already considered to be catastrophic, and therefore it would appear that the presence of two particles within the system has had little detrimental effect. This is also evident from the relative invariance of the strength and toughness for systems containing voids separated by 5 and 10 unit lengths (figure 6.23).

The remaining configurations considered consist of two voids diagonally aligned with respect to the tensile direction. The initial normal strain fields, prior to damage accumulation are given in figure 6.29, which shows systems corresponding to void

(a)

(b)

(c)
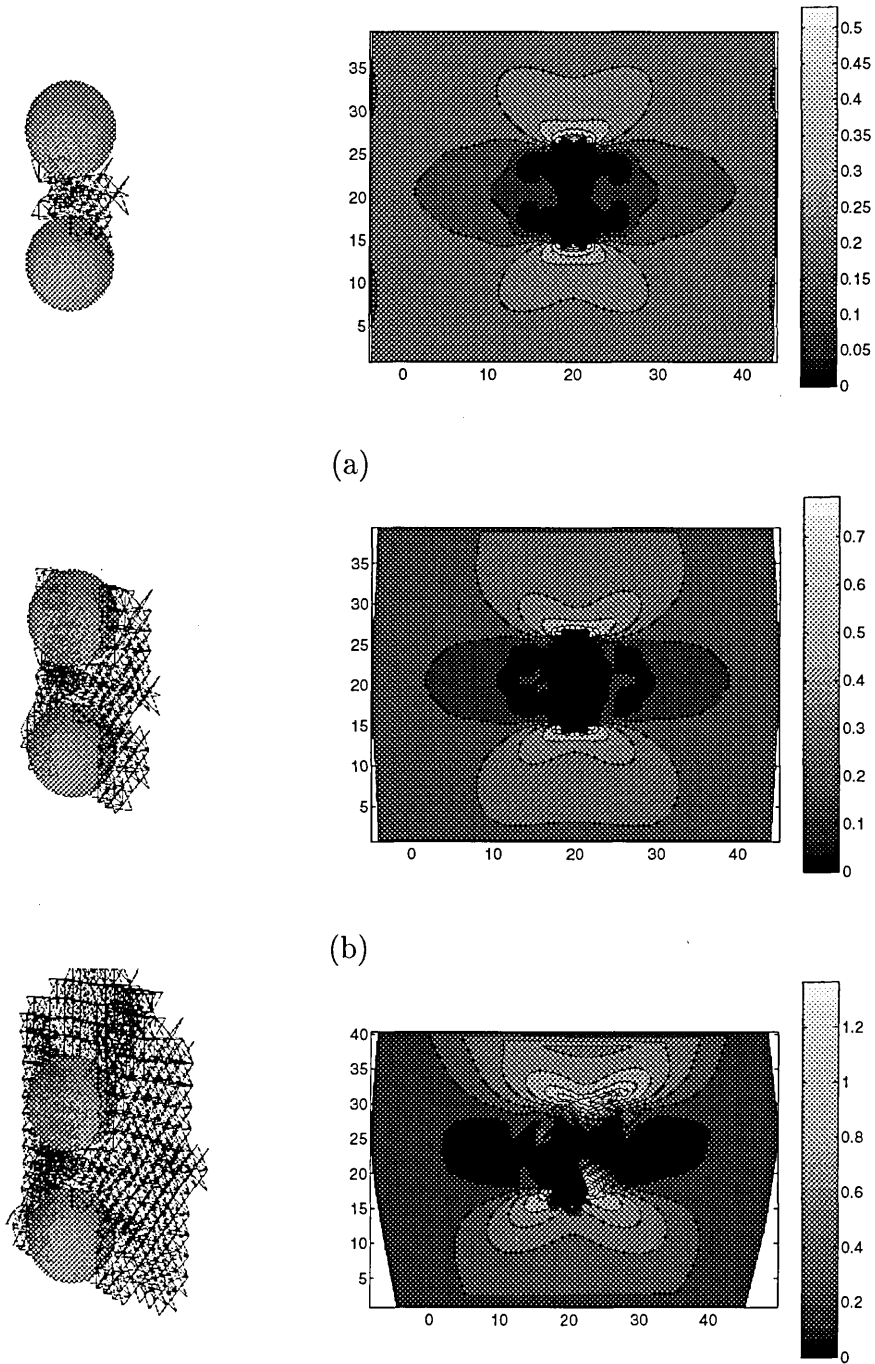
Figure 6.27: The broken bonds (left), and 2D normal strain contours (right) through the centre of both voids (aligned parallel to tensile direction with a void separation of 2 unit lengths), are presented for three stages of the simulation; applied stress is $1.74\sigma_y$ and damage is (a) 222, (b) 971, and (c) 2858.
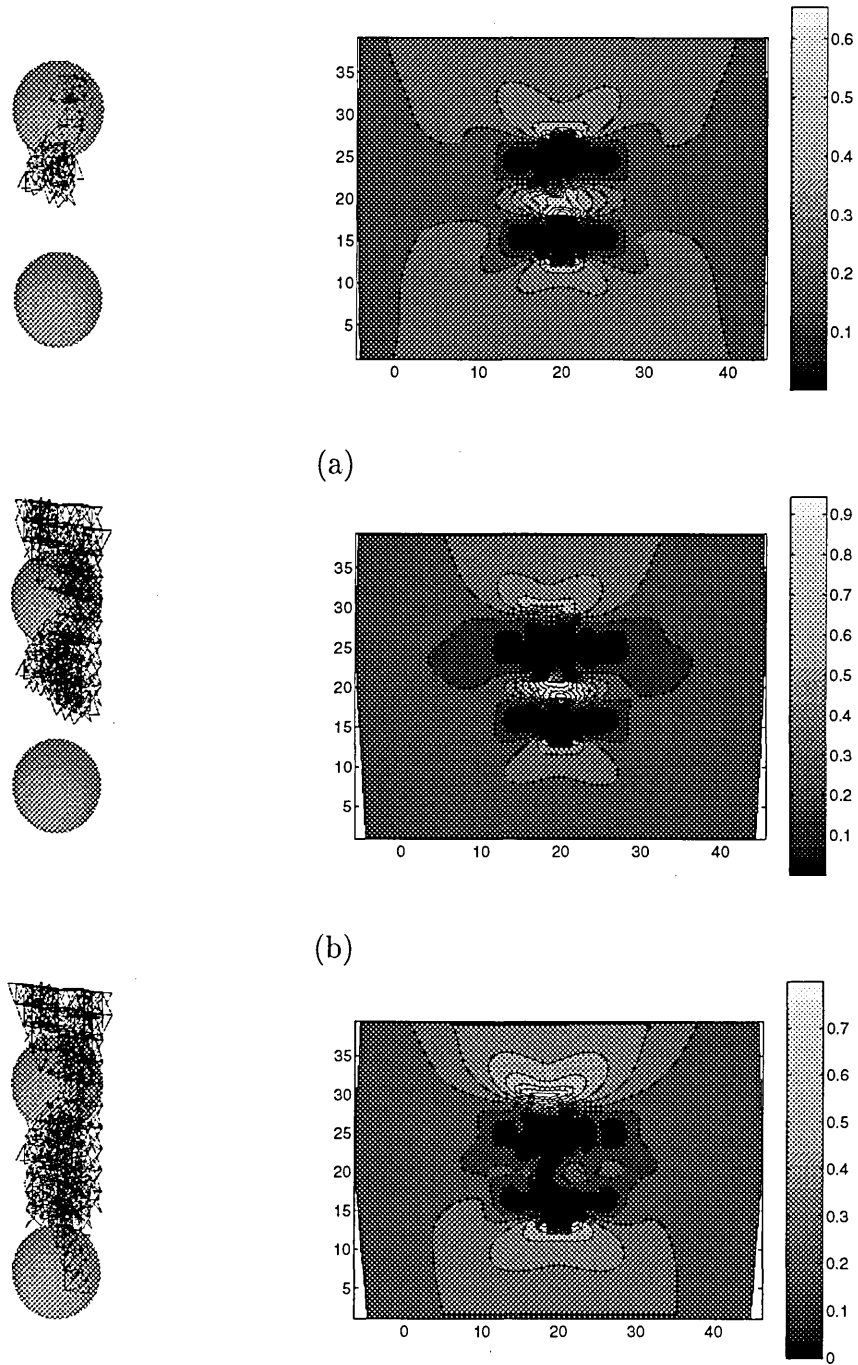
Figure 6.28: The broken bonds (left), and 2D normal strain contours (right) through the centre of both voids (aligned parallel to tensile direction with a void separation of 5 unit lengths), are presented for three stages of the simulation; applied stress is $1.79\sigma_y$ and damage is (a) 187, (b) 858, and (c) 1200.

separations of 2.1 and 9.1 unit lengths. The normal strain range does not exhibit any significant variability between the systems considered, although the fields are calculated using a central difference approximation, whilst the strain based criterion is assessed in a localised region between two nodes. The differences are exhibited by the onset of crack propagation, hence the variations in strength and toughness of the systems, and the resultant crack morphology.


(a)   (b)
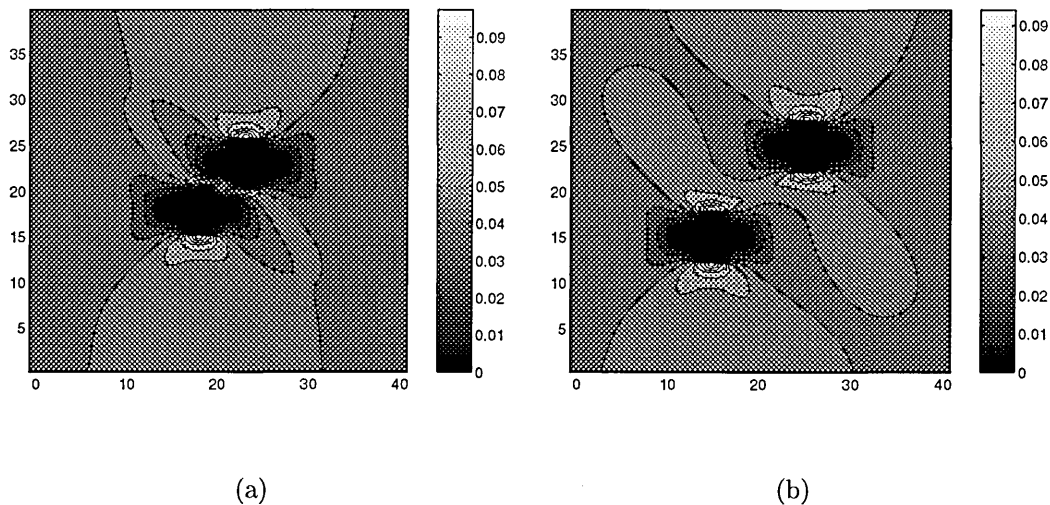
Figure 6.29: 2D Contour plots, taken through the centre of both voids (aligned diagonally to tensile direction), of non-dimensional normal strain for a void separation of (a) 2.1 and (b) 9.1 unit lengths. The applied stress, in the horizontal direction, is $1.4\sigma_y$.

The damage and normal strain fields, displaying void coalescence in the system with a void separation of 2.1, are presented in figure 6.30. The voids coalesce through the diagonal propagation of a crack between them; once the voids have amalgamated, the resultant void grows perpendicular to the tensile direction. This is more evident in the system·which considers a greater void separation of 4.9 unit lengths (figure 6.31); the crack morphology is similar, but the extent of diagonal crack propagation

(a)

(b)
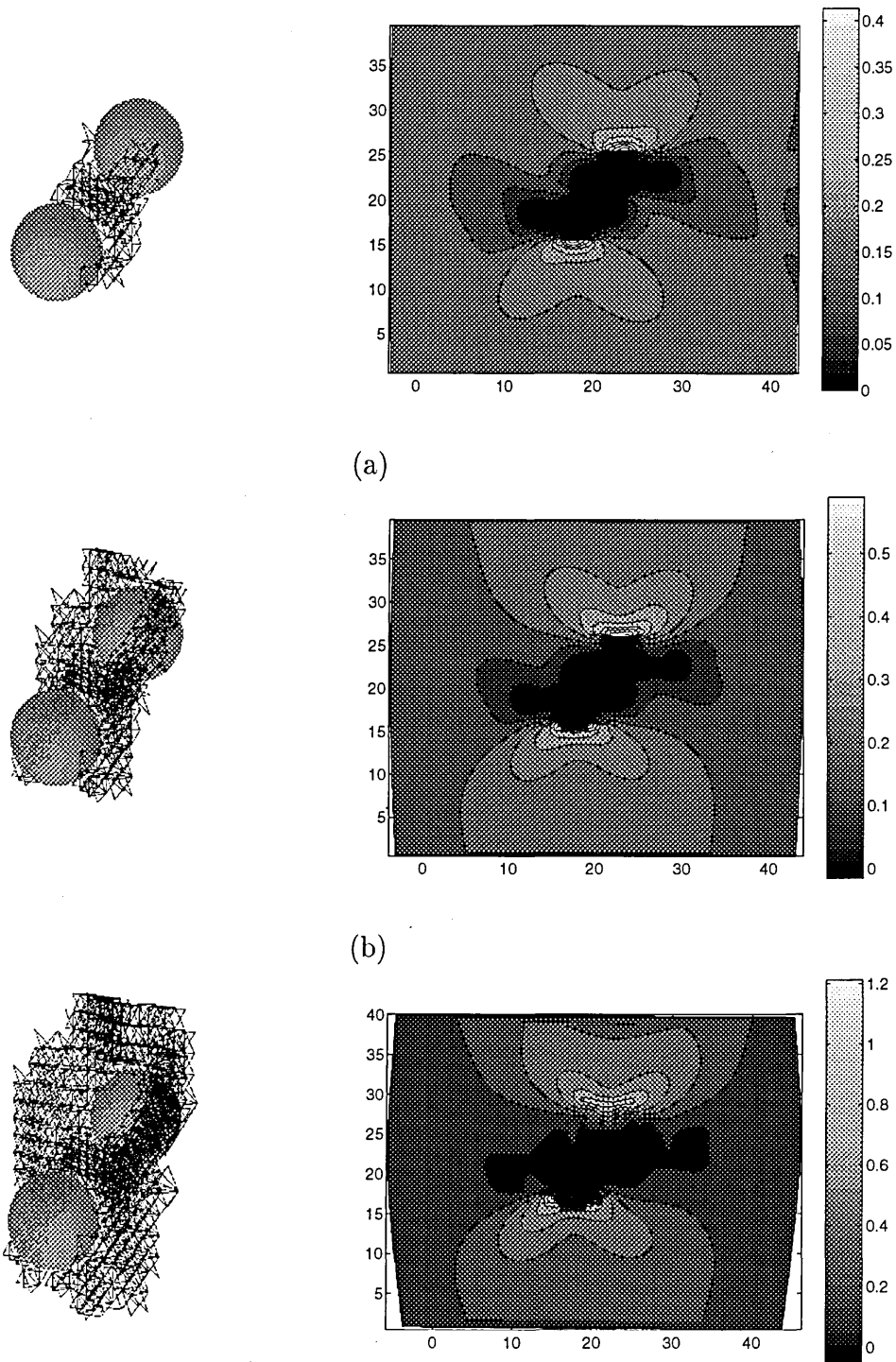
(c)

Figure 6.30: The broken bonds (left), and 2D normal strain contours through the centre of both voids (aligned diagonally to tensile direction with a void separation of 2.1 unit lengths), are presented for three stages of the simulation; applied stress is $1.69\sigma_y$ and damage is (a) 250, (b) 921, and (c) 2273.

119
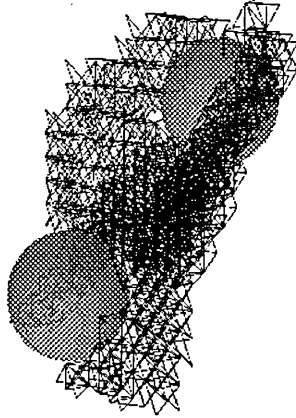
Figure 6.31: The broken bonds for two voids aligned diagonally to tensile direction with a void separation of 4.9 unit lengths; the applied stress is $1.76\sigma_y$ and damage is 2244.

is increased. Extending the void separation to 9.1 unit lengths results in the growth of one of the voids transverse to the tensile direction, exhibiting no propensity for coalescence. This is reflected in the strength and toughness of the systems, where the diagonal orientation with respect to the tensile direction is more detrimental than either the parallel or perpendicular alignments. The effects of reducing the inter-void distance is greater for the diagonal configurations. Similar effects have been observed experimentally, where in ductile fracture the crack has been observed to propagate in a zigzag manner [24], and in void sheet coalescence the secondary population of particles debond in bands of intense shear between voids, created via the decohesion of the primary population of particles, at 45° to the tensile direction [18].

6.3.1 Summary.

Systems consisting of voids aligned parallel with the tensile direction do not exhibit any appreciable depletion in strength or toughness with varying void separation. In contrast, the strength and toughness of systems containing voids, both aligned perpendicular and at 45° with the tensile direction, exhibit a dependence on void separation; voids positioned in close proximity are significantly more detrimental.

6.4 Interactions between two Fe3C particles.

The detrimental effects of alignment and particle separation upon the strength and toughness of a two spherical Fe3C particle system is investigated. The alignments and inter-particle distances are identical to those of the previous section; parallel, perpendicular and diagonal alignments with respect to the tensile direction and particle separations of 2, 5, and 10 unit lengths (2.1, 4.9, and 9.1 unit lengths for diagonally aligned particles) are investigated. The resulting strength and toughness of the systems considered are depicted in figure 6.32, which reveals the consequences of varying both the alignment and particle separation. It is found throughout this section that the resulting crack morphology is very similar to previously considered systems containing voids, although the effects and characteristics of void nucleation can be of importance. As the failure criterion for interfacial decohesion is the attainment of a critical stress, and this is the principle phenomena of interest, the stress field is considered to be of greater relevence.
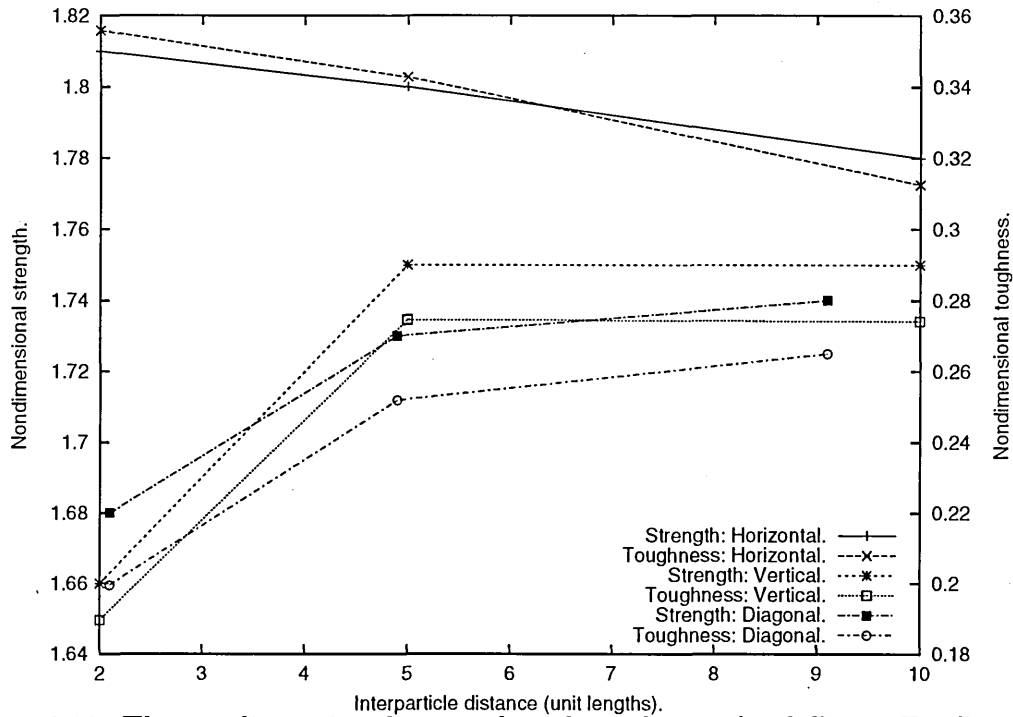
Figure 6.32: The nondimensional strength and toughness, for different Fe3C particle alignments, as a function of particle separation. The tensile direction is considered to be horizontal.

The damage acquired by the system as a function of the energy absorbed (numerical integration of the stress-strain curve) is presented in figure 6.33, for systems of two particles aligned parallel with the tensile direction. Such plots were not considered for voided systems as damage accumulation occurs at the onset of catastrophic failure, whilst in particle systems the processes of particle fracture and decohesion may result in damage accumulation without incurring catastrophic failure. The incremental nature of the relation is due to the spasmodic accumulation of damage within the system, and subsequent arrest of propagating cracks. On three occassions the curves can be observed to plateau: at the approximate damage accumulation of 185, 440, and 670 broken bonds. The resulting phenomena are similar for all three particle separations, and therefore only the case where the particle separation is 2

unit lengths is elaborated. The broken bonds and normal stress contours associated with the three plateaux in the damage-energy curves, for the system considering a particle separation of 2 unit lengths, are given in figure 6.34.
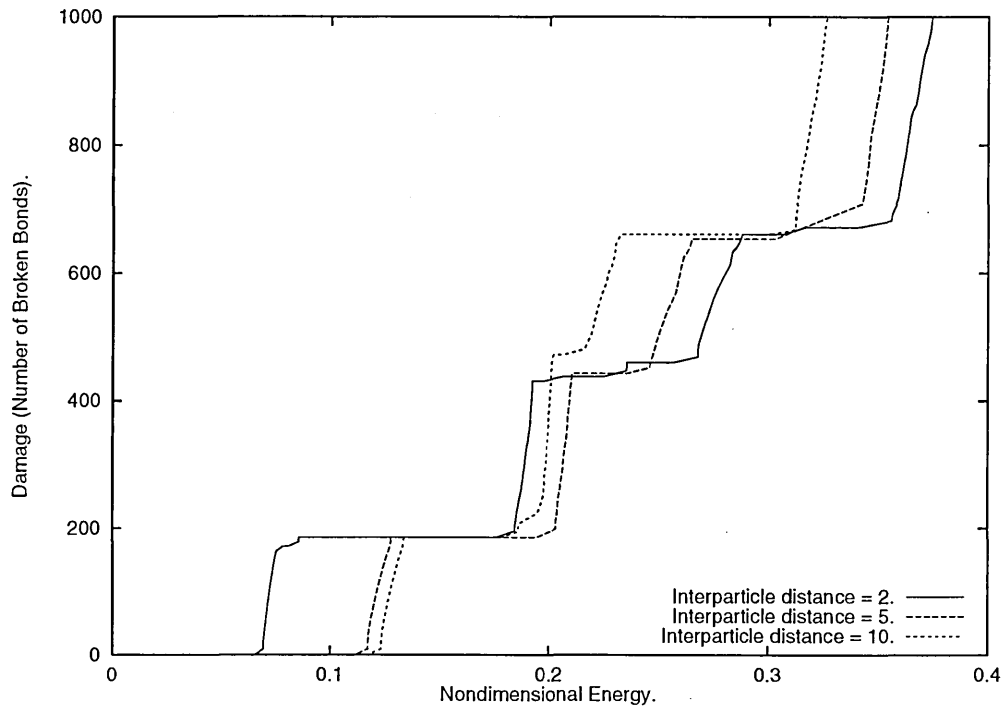
Figure 6.33: The damage accumulated (broken bonds) as a function of the energy absorbed (integration of the stress-strain curve) for various particle separations. The particles are aligned parallel with the tensile direction.

At the first plateau the particle on the left can be observed to have partially debonded, and the propagating crack is arrested at the interfaces with the matrix in the equatorial directions (figure 6.34a). As the energy of the system is further increased (through the increase in applied stress) the particle becomes capable of completely debonding from the matrix. The particle on the right is shielded by the nucleated void on the left, and is therefore incapable of debonding. As the energy of the sytem is again increased the particle on the right attains a sufficient level of stress at the interface for partial debonding to occur; full decohesion of the particle

123
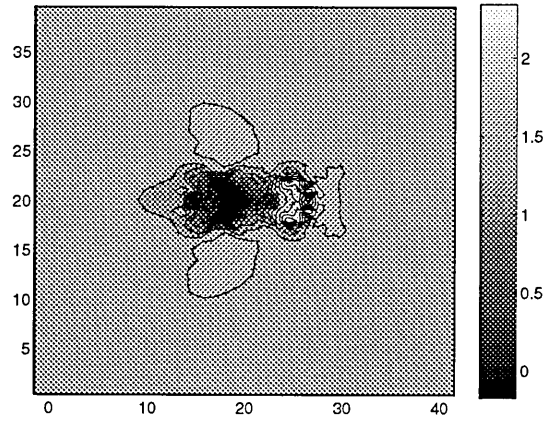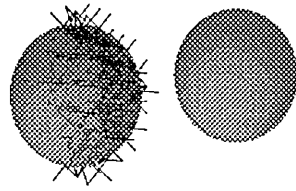
(a)
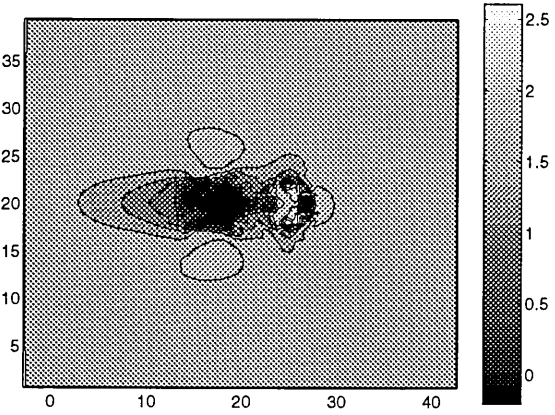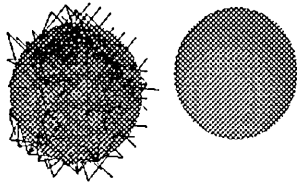
(b)
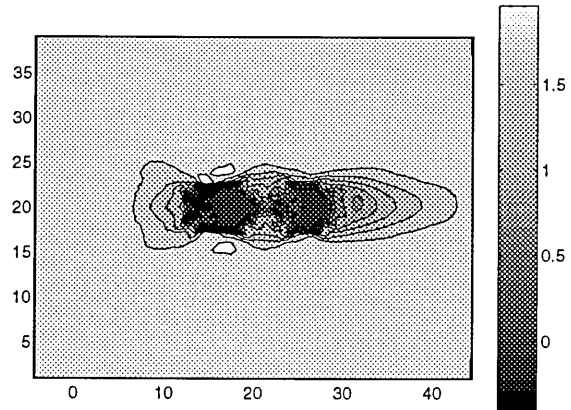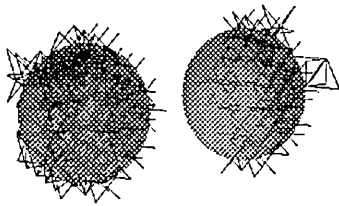
(c)

Figure 6.34: The broken bonds (left), and 2D normal stress contours (right) through the centre of both particles (aligned parallel to the tensile direction with a particle separation of 2 unit lengths), are presented for three stages of the simulation; (a) applied stress is $1.55\sigma_y$ and damage is 185, (b) applied stress is $1.68\sigma_y$ and damage is 431, and (c) applied stress is $1.8\sigma_y$ and damage is 661.

124

is interupted by the catastrophic propagation of fracture into the matrix.

The most intriguing phenomena appears to be the shielding effects as a consequence of the initial debonding of one of the particles (debonding of both particles simultaneously is improbable in this simulation, due to quasi-static aproximation of crack propagation). The effects of the inter-particle distance is profound; the stress and strain concentrations acompanying the deformation of a Fe3C particle have been found to be at the poles of the particle, in the tensile direction, and therefore particles aligned parallel to the tensile direction may experience a concentration in stress. This stress concentration results in premature debonding, when particles are in close proximity, but the subsequent shielding effects are also more pronounced. This is evident in figure 6.33, where a reduction in particle separation, results in void nucleation about the first particle occuring at lower energies, but the decohesion of the second particle, and subsequent catastrophic failure, occuring at higher energies.

The damage accumulation in systems possessing two particles, orientated perpendicular with respect to the tensile direction, are considered in figure 6.37. Decreasing the particle separation has a detrimental effect upon the system; both upon the initial debonding and the onset of catastrophic fracture. The process of debonding varies with the inter-particle distance, as indicated by the different plateau levels in the simulations.
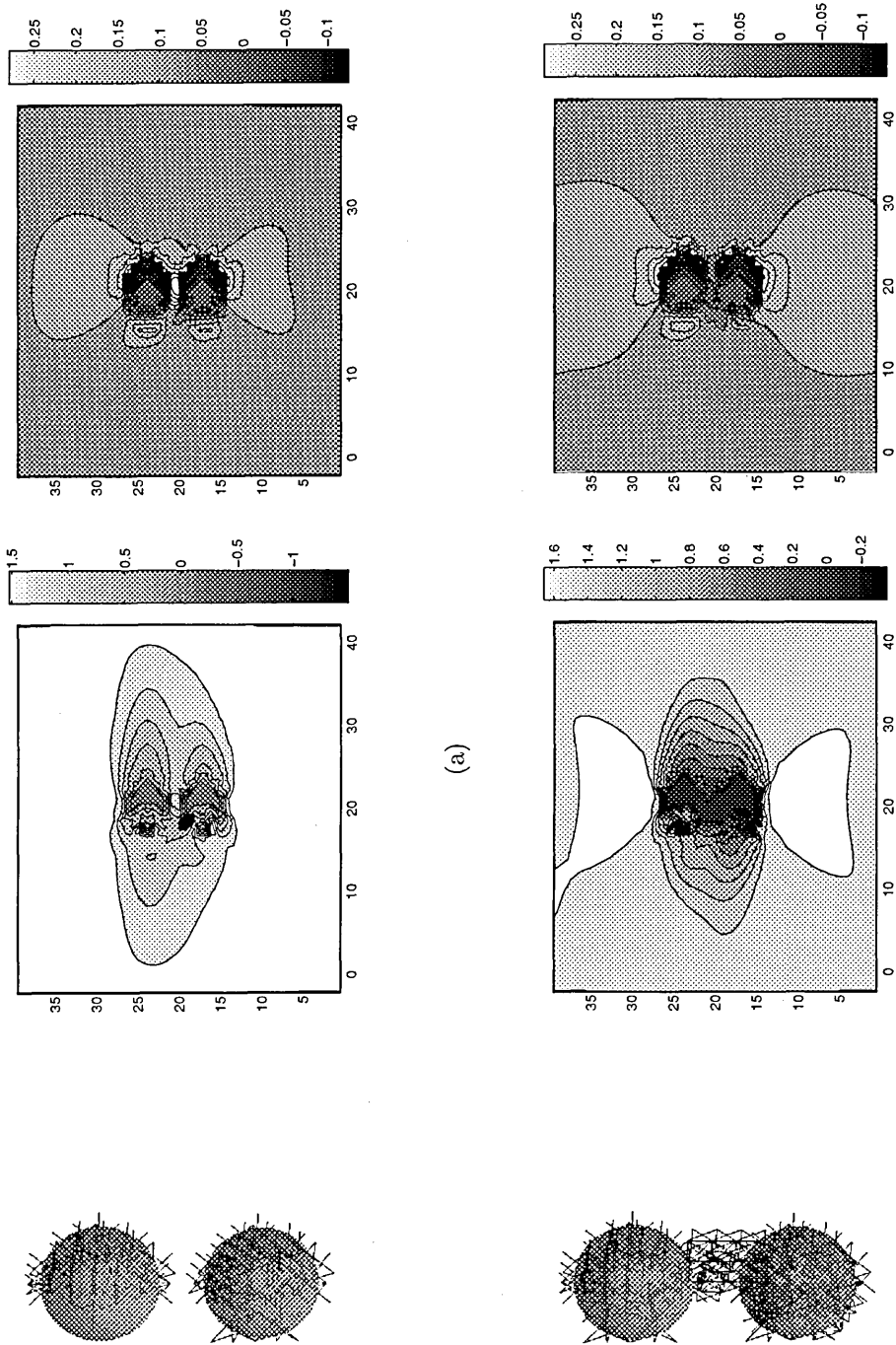
Figure 6.35: The broken bonds (left), 2D normal stress contours (centre), and 2D normal strain contours (right) through the centre of both particles (aligned perpendicular to the tensile direction with a particle separation of 2 unit lengths), are presented for two stages of the simulation; (a) applied stress is $1.61\sigma_y$ and damage is 445, and (b) applied stress is $1.63\sigma_y$ and damage is 810.
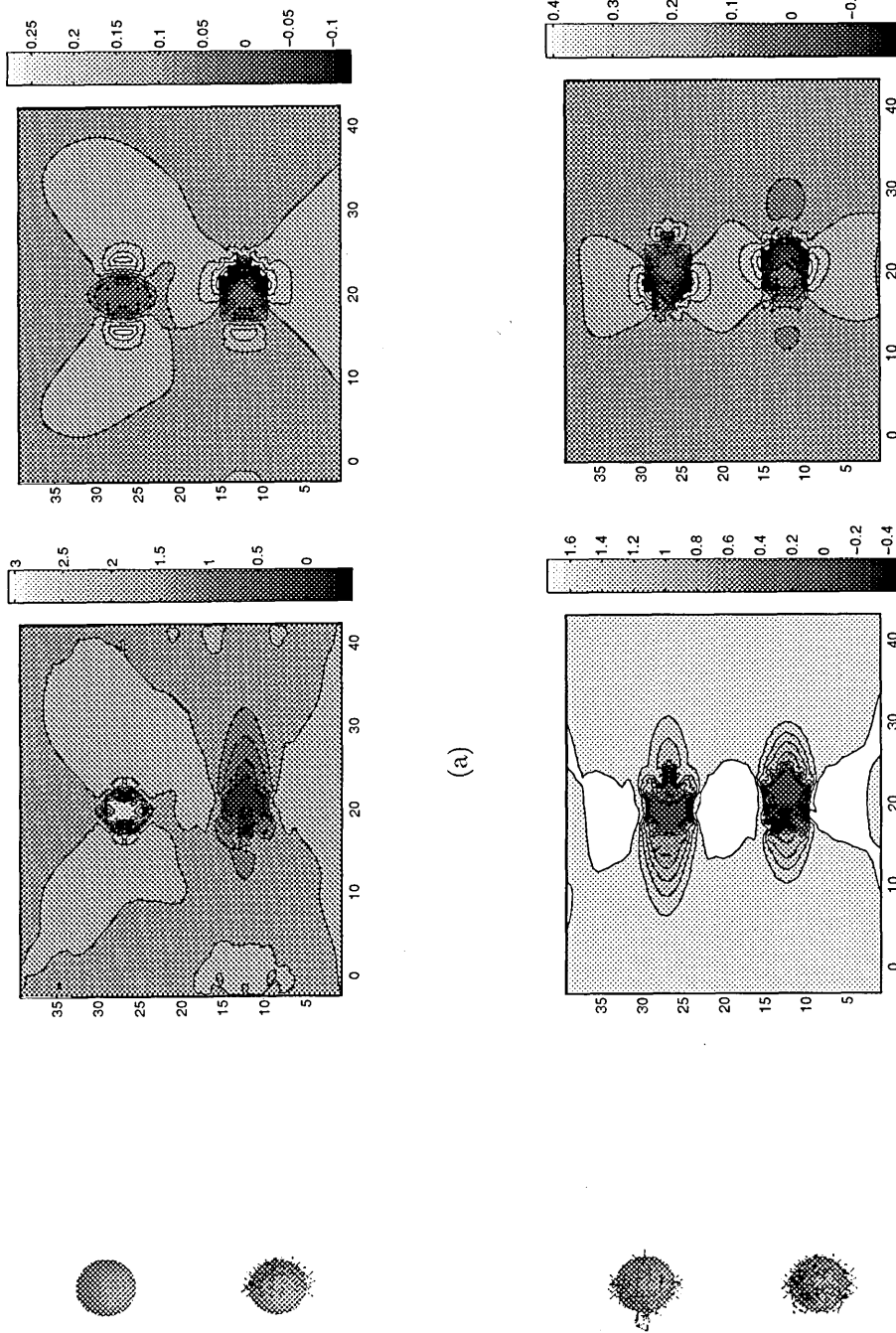
Figure 6.36: The broken bonds (left), 2D normal stress contours (centre), and 2D normal strain contours (right) through the centre of both particles (aligned perpendicular to the tensile direction with a particle separation of 10 unit lengths), are presented for two stages of the simulation; (a) applied stress is $1.65\sigma_y$ and damage is 185, and (b) applied stress is $1.72\sigma_y$ and damage is 641.
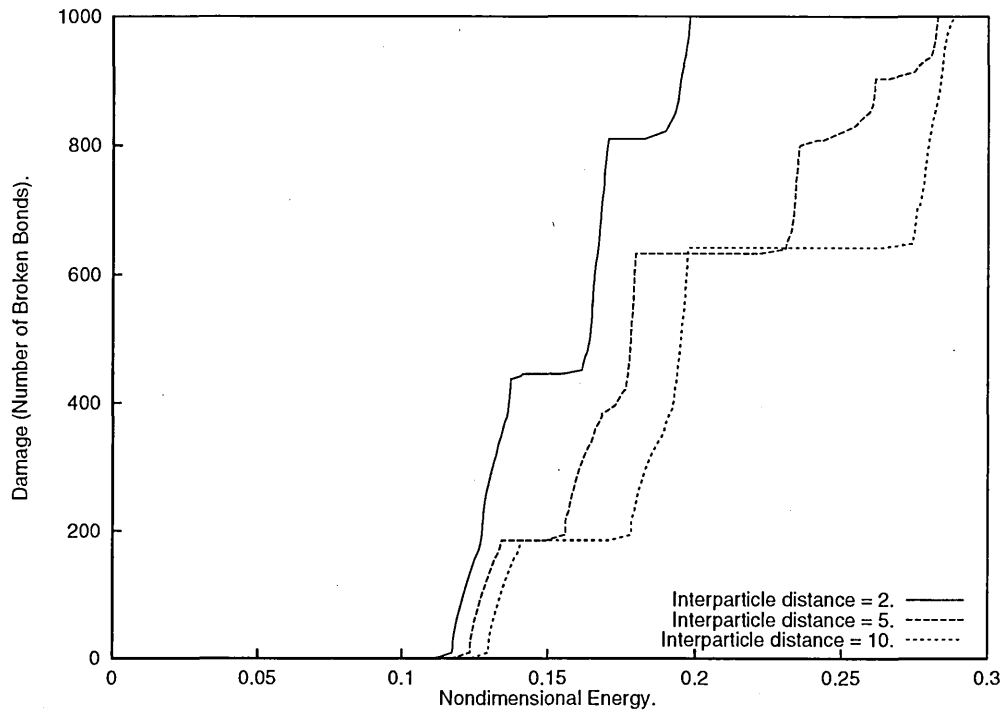
Figure 6.37: The damage accumulated (broken bonds) as a function of the energy absorbed (integration of the stress-strain curve) for various particle separations. The particles are aligned perpendicular with the tensile direction.

The broken bonds, normal stress contours and normal strain contours associated with the two plateaux in the damage-energy curves, for the system considering a particle separation of 2 unit lengths, are given in figure 6.35. The first plateau occurs subsequent to the partial debonding of both particles; the damage to which occurs on the same side. The fracture arrests prior to complete debonding and the energy in the system is incremented, until the ductile fracture of the intermediate region occurs and the two voids initially coalesce (figure 6.35b). The fracture arrests at this stage, incapable of progressing further, since the region of high deformation inbetween the partially debonded particles was highly localised. Further increments in the system energy result in the eventual growth of the resultant void into the matrix, and catastrophic fracture.

The plateaux, for the system considering a particle separation of 10 unit lengths, occur at different regions of the damage-energy curve, and the broken bonds, normal stress contours and normal strain contours for these two regions are given in figure 6.36. The first plateau occurs after the partial debonding of one of the particles; the resultant stress and strain concentrations, in the equatorial plane of the nucleated void, do not appear initially to affect the second particle. The energy within the system is incremented further until the second particle begins to debond, and is capable of complete decohesion prior to the arrest of damage accumulation, at the second plateau. Catastrophic failure eventually occurs with the attainment of sufficient energy in the system for void growth; through crack propagation from one of the voids into the matrix.

The final configurations to be investigated consider the particles to be aligned diagonally, at 45° with respect to the tensile direction. The interfacial decohesion occurs in a similar manner for all three inter-particle distances considered; although the final crack morphology follows that of the voided system (coalescence associated with particle separations of 2.1 and 4.9 unit lengths, and the independent growth of one of the nucleated voids for a particle separation of 9.1 unit lengths). The damage-energy curves for the systems considered are given in figure 6.39. There are two plateaux, which exist at roughly the same level of damage, for all three systems.
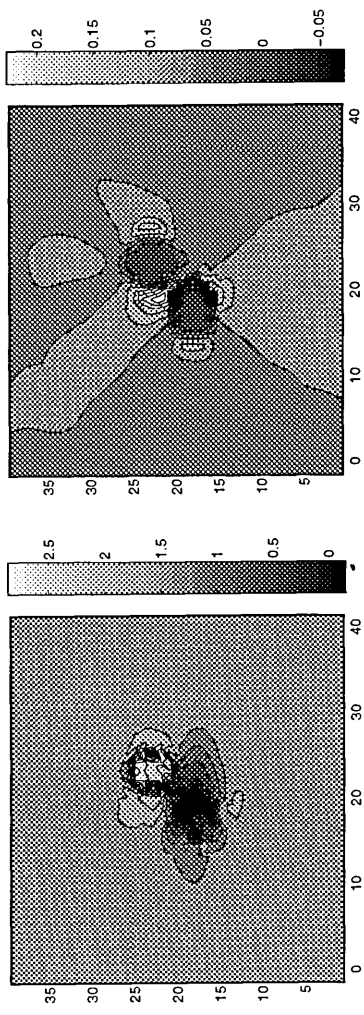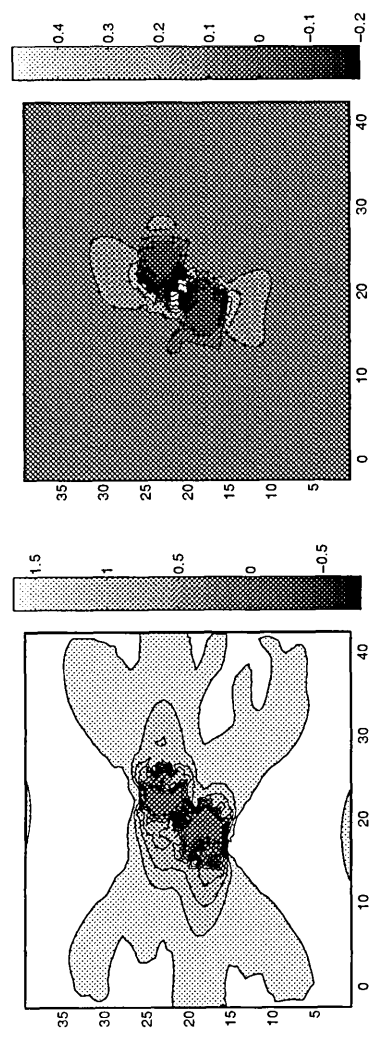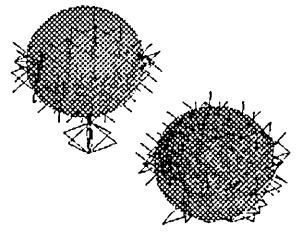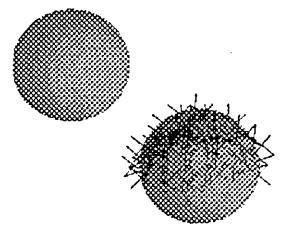
Figure 6.38: The broken bonds (left), 2D normal stress contours (centre), and 2D normal strain contours (right) through the centre of both particles (aligned diagonally with respect to the tensile direction with a particle separation of 2 unit lengths), are presented for two stages of the simulation; (a) applied stress is $1.55\sigma_y$ and damage is 185, and (b) applied stress is $1.65\sigma_y$ and damage is 594.
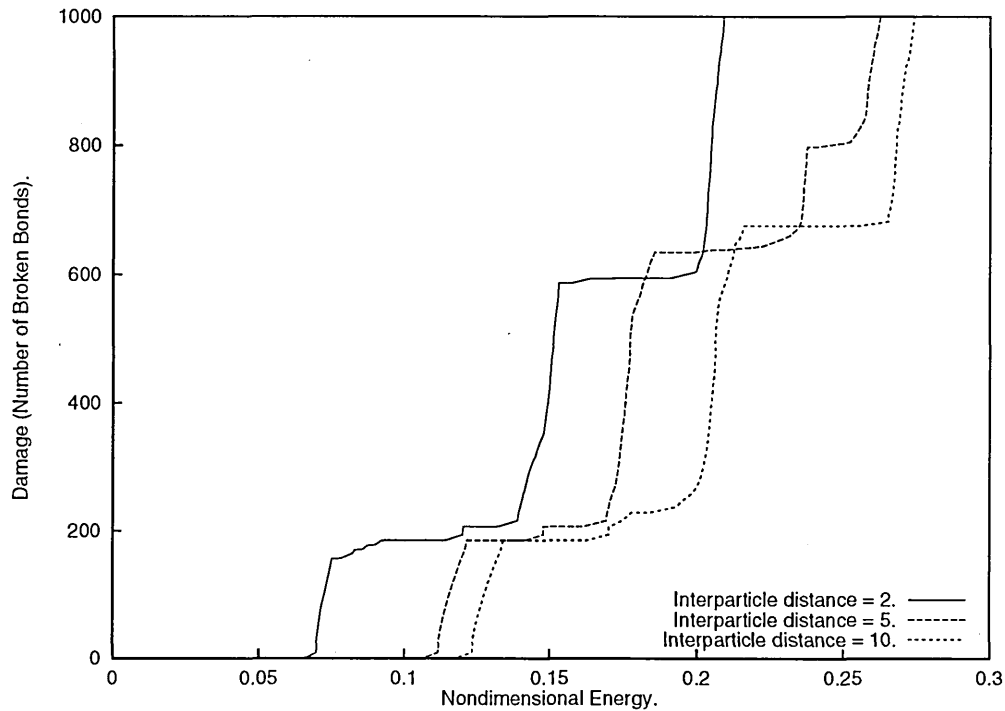
Figure 6.39: The damage accumulated (broken bonds) as a function of the energy absorbed (integration of the stress-strain curve) for various particle separations. The particles are aligned diagonally with respect to the tensile direction.

The system containing particles separated by a distance of 2.1 unit lengths is investigated; the broken bonds and both normal stress and normal strain contours are presented in figure 6.38, corresponding to the same stages in the simulation as the plateaux. The first plateau occurs after the partial decohesion of one of the particles, the crack propagates along the particle-matrix interface and is arrested, in the equatorial plane, at the matrix. Following subsequent increase in the energy of the system, the other particle attains the capability to debond completely, as indicated by the sudden rise in damage accumulated. At this stage of the simulation, the system possesses insufficient energy for void growth, but with increasing the system energy, crack growth occurs between the two particles before catastrophically continuing into the matrix.

131

6.4.1 Summary.

The systems considering the interaction of Fe3C particles elucidate the complex interactions between void nucleation and subsequent void growth. When particles are orientated parallel to the tensile direction the stress concentrations, between particles in close proximity, result in premature decohesion, whilst the resultant nucleated voids show evidence of a shielding effect. The more detrimental configurations, consisting of particles orientated both perpendicular and diagonally with the tensile direction, can result in complicated phenomena (such as partial particle decohesion) occurring.

The effects of diagonally orientating particles would appear more detrimental at separations of ≈ 5 unit lengths, than in systems where the particles are orientated perpendicular to the tensile direction. This trend does not continue with reduced separation, where the perpendicularly orientated particles are found to be more deleterious. The discretisation effects, although limited through the consideration of constant particle size, may exhibit a variable influence in different directions, and the effects upon particle decohesion, in the diagonal directions, may differ from those in directions along the lattice.

6.5 Conclusions.

In this chapter the deformation fields, and the preliminary onset of fracture, have been investigated for an austenitic steel particulate system. The deformation fields,

in the presence of plastic deformation, have been explored, and the regions of stress and strain concentrations (pertinent to fracture initiation) have been identified. The irregularity of the stress field within the particles, as a consequence of plastic deformation, presents a key deviation from the previously considered elastic behaviour.

The preliminary decohesion of spherical Fe3C and MnS particles would appear consistent with experimental expectations; MnS particles debond at lower stress levels, as indicated by the lower interfacial strength, and completely debond prior to void growth. The Fe3C particle, in contrast, debonds much later, at higher stress levels, at which point the deformation fields are sufficiently large to enable the nucleated void (partially debonded particle) to spread into the matrix.

The simulation of an elongated MnS particle appropriately predicted the characteristic particle fracture, as observed experimentally. The effects of varying the aspect ratio of an elongated MnS inclusion where two fold: firstly the stress concentration in the centre of the particle increases with the aspect ratio, resulting in internal fracture at lower stresses, and secondly the strength and toughness of the material increases with the particle aspect ratio. Whether the increase in strength and toughness is a consequence of the mutual shielding of the voids, nucleated through internal fracture, or an artifact of the model, is unknown.

The interaction between two inclusions in a uniaxially deformed system were investigated and it was found that generally when diagonally orientated inclusions, with respect to the tensile direction are considered, the system exhibits a detrimental reduction in both strength and toughness; although in the particulate sys-

133

tem, considering particles in close proximity, this does not appear to be the case. The strength and toughness of systems initially containing voids (and therefore not including particle decohesion) are consistently higher than corresponding systems containing particles, indicating that void nucleation has a detrimental effect.

Chapter 7

The Random Dispersion of

Inclusions.

The size and positioning, of particle inclusions, appreciably influence the strength and toughness of steels; the scatter in material properties is thought to be a consequence of the random distribution of particles. In order to investigate the effects of particle dispersion, and volume fraction of inclusions, the lattice spring model is applied to the simulation of random heterogeneous systems.

In order to effectively analyse the ability of LSM's to describe macroscopic phenomena through the simulation of microstructural features the probability of finding a maximum stress intensity for a given system size is investigated. The probability of a given level of maximum stress occurring in a given volume depends upon the statistical distribution of constituents. The larger the system considered the more void

interactions that may occur, and hence the greater the probability of a maximum stress level occurring. An effective method of analysing the statistics of extreme events is the Weibull distribution; the distribution is best fitted using the maximum likelihood method

The variation of the average volume fraction of voids between different distributions is also expected to result in variations in the extreme levels of deformation fields. In section 7.2 the initial crack propagation is considered, and the strength and toughness of the systems investigated.

The material under investigation is an austenitic weld steel, and the inclusions are assumed to be debonded; the simulation of voids is therefore undertaken. The distributions of spherical particle sizes and the number of inclusions found in a $100\mu m^2$ sectioned area are given in the following tables (obtained from Rolls-Royce Associates).

Spherical size distribution	Probability
$< 0.5\mu m$	52.4%
$0.5 \rightarrow 1\mu m$	36.6%
$1 \rightarrow 1.5\mu m$	8.4%
$1.5 \rightarrow 2\mu m$	1.6%
$> 2\mu m$	1.0%

Number of Inclusions (per $100\mu m^2$)	Probability
< 100	2%
$100 \rightarrow 150$	25%
$150 \rightarrow 200$	45%
$200 \rightarrow 250$	25%
$250 \rightarrow 300$	3 %

The voids are randomly placed within the simulation according to the same statistical distributions as found experimentally. The positioning of voids in close proximity

to a boundary, such that the separation between the void and the simulation boundary is less than the voids radius, are rejected. This can bias the system as larger voids do not occur near the boundaries, although the statistical distribution favours smaller voids, and therefore this is not considered significant. The distance between voids is given a lower bound of two unit lengths; void overlap is therefore forbidden and plastic deformation is allowed for in the intermediate region.

In a system of 41^3 nodes the average number of voids is chosen to be 8; enough voids to enable the investigation of void interactions to occur, whilst allowing sufficient void sizes (in unit lengths) to capture the necessary field disturbances. The average number of particles observed in a sectioned area of $100\mu m^2$ is 175, and the average particle radius (R^{ave}) is $\frac{1}{2}\mu m$, therefore 175 particles were detected in an volume of $100\mu m^2 \times 2 \times \frac{1}{2}\mu m = 100\mu m^3$. The non-dimensional volume over which particles are positioned corresponds to the effective length, $L_*^{eff} = L_* - 2R_*^{ave}$, as particles positioned less than the particle radius from the boundary are prohibited. Note that non-dimensional quantities are denoted by a star. The length of a {100} bond in the model corresponds with a distance, $d = \frac{L}{L_*^{eff}}$, as the non-dimensional length of a {100} bond is unity. The dimensional size of the simulation is given by $L^3 = 8 \times \frac{100\mu m^3}{175} \therefore L = 7.7\mu$. In a system of size $L_* = 40$ the effective non-dimensional system size, $L_*^{eff} = 35.4$, the average non-dimensional radius, $R_*^{ave} = 2.3$, and the length of a {100} bond, $d = 0.22\mu m$. It should be noted that the simulations are independent of the absolute dimensions of the system, as the behaviour is governed by continuum mechanics.

The empirical cumulative distribution functions, corresponding to the statistical properties of the non-dimensional particle sizes and the number of particles in a system of size $L_* = 40$, are given in figure 7.1. The random numbers generated, in dictating the void population and sizes, are governed by these functions. The corresponding experimental data is also presented, in histogrammatic form, and it should be noted that particle sizes in the range $< 0.5 \mu m$ are interpreted as $0.25 \rightarrow 0.5 \mu m$ within the simulation. This is to restrict the radius of particles to a lower bound of $0.25 \mu m$, or 1.15 unit lengths, as adequate simulation of smaller voids is considered impractical. The statistical evaluation of the number of particles is also biased, as zero or single particle systems are considered profitless and therefore rejected; the probability of such an occurrence is small. Results from the simulation of voided systems, obeying the correct statistical properties associated with real heterogeneous systems, are now presented.

7.1   System size dependence.

The various system sizes considered, along with the average number of particles expected, is given in the following table.

System size (unit lengths)	Average number of particles
30	2.96
35	5
40	8
45	11.9
50	16.9
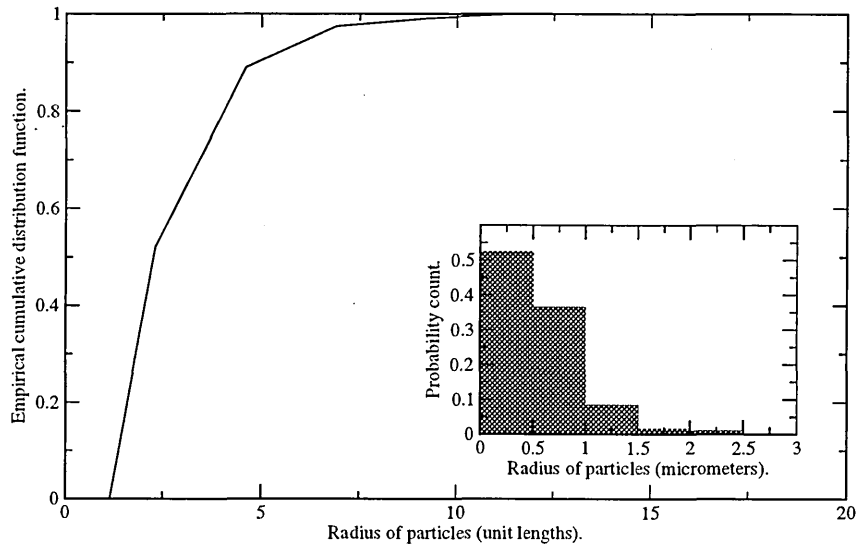
(a)
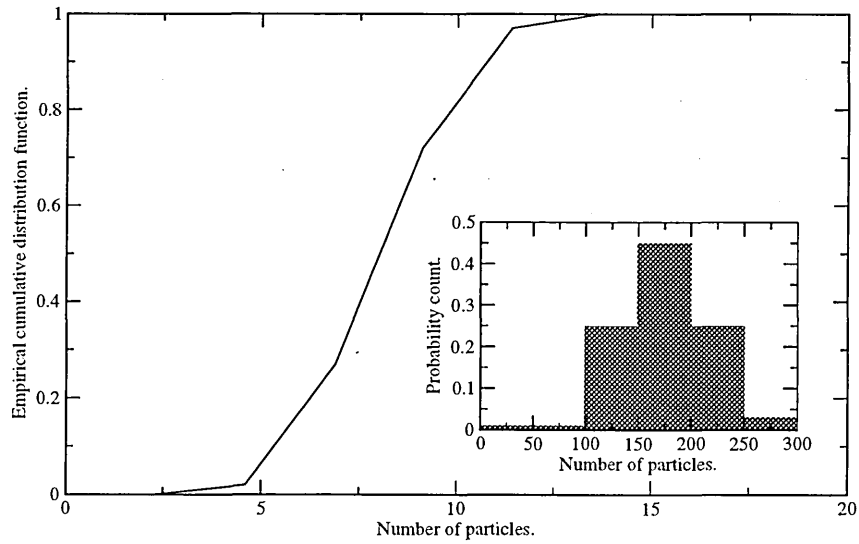
(b)

Figure 7.1: The empirical cumulative distribution functions, corresponding to the particle size distribution and the number of particles ($L_* = 40$). Experimental data, in histogrammatic form, is also presented.

The extreme levels of the deformation fields are considered relevent to the fracture process and therefore the maximum stress field in the system is investigated, as a function of applied stress.

Sets of twenty simulations are conducted for each size and the distributions of applied stresses corresponding to levels of maximum stress are obtained; as fracture is associated with the extreme values of the deformation fields, the question is: what is the probability of a given level of maximum stress occuring for a given applied stress?

The size effect on failures in solids has been investigated by Weibull [11], through the introduction of weakest link statistics; based upon the proposition that a chain as a whole has failed if any of its parts has failed. The cumulative distribution function is of the form

$$c(x) = 1 - \exp\left[-n\left(\frac{x-a}{b}\right)^m\right] \tag{7.1}$$

which upon differentiation results in the following probability density function

$$p(x) = \frac{mn}{b}\left(\frac{x-a}{b}\right)^{m-1}\exp\left[-n\left(\frac{x-a}{b}\right)^m\right] \tag{7.2}$$

where b is the scale parameter, m is the Weibull modulus, a is the location parameter and n is the number of links (volumetric variation). The dependence of the Weibull distribution function on the system size can be interpreted as a size dependency within the scale parameter, therefore $\frac{b^m}{n}$ becomes b_j^m, where the suffix j denotes size dependence.

The distribution is commonly fitted to experimental data via the following relationship

$$\ln \left[\ln \left(\frac{1}{1 - c(x)} \right) \right] = m \ln(x - a) - m \ln b_j \tag{7.3}$$

where a straight line fit of $\ln(x - a)$ against $\ln \ln \left(\frac{1}{1-c(x)} \right)$ produces a gradient of m, and an intercept of $-m \ln b_j$. In order for the least-square estimator to be unbiased, the errors in one observation should be uncorrelated with those from other observations, and errors should be normally distributed with zero mean and constant variance [151]. This is not the case in the Weibull distribution function, and therefore the method of maximum-likelihood estimation is adopted.

The method of maximum likelihood consists in taking as the estimators those values of the parameters which maximise the likelihood of the observations [152]. The likelihood of a single observation is given by $p(x_{ij})$, where x_{ij} is the ith observation in a system whose size is indicated by j, and with the likelihood of a series of observation being given by $\Lambda = \prod_{<i,j>} p(x_{ij})$. Computationally, it is more convenient for the logarithm of the likelihood to be considered; since $\ln \Lambda$ is an increasing function of Λ they will both possess a maximum at the same parameter values. The maximum is obtained through the differentiation of $\ln \Lambda$ with respect to the parameters. The three parameter Weibull distribution is computationally difficult to solve directly (systems consisting of more than one nonlinear equation are particularly difficult to solve numerically [153]).

The two-parameter Weibull distribution is obtained through the substitution of $t_{ij} = x_{ij} - a$, therefore removing the functional dependence upon the location parameter;
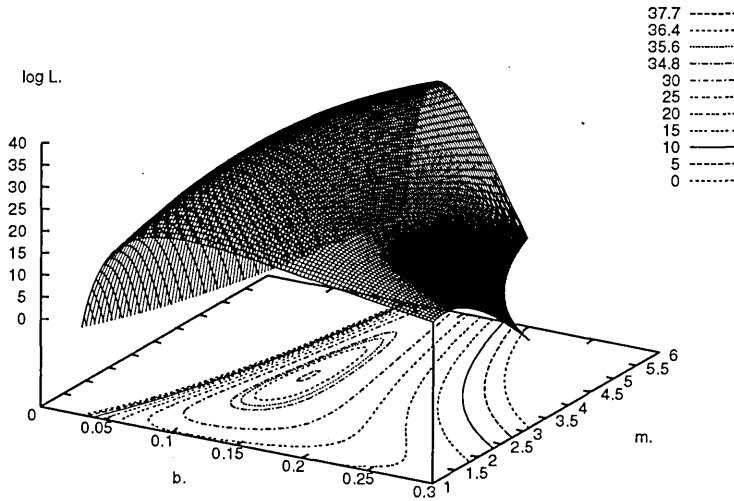
Figure 7.2: The variation of the logarithm of the likelihood, for a single sytem size as a function of b and m. Contours corresponding to 95% confidence ($\ln \Lambda = 34.8$), 90% confidence ($\ln \Lambda = 35.6$), and 80% confidence ($\ln \Lambda = 36.4$) are displayed; the maximum corresponds with $\ln \Lambda = 37.8$

the subsequent solution is consequently a function of the initial value of a. The logarithm of the likelihood is of the form

$$\ln \Lambda = \sum_{<j>} \left[\zeta \ln \left(\frac{m}{b_j} \right) \right] + \sum_{<i,j>} \left[(m-1) \left(\ln t_{ij} - \ln b_j \right) \right] + \sum_{<i,j>} \left[- \left(\frac{t_{ij}}{b_j} \right)^m \right] \quad (7.4)$$

where ζ is the number of observation, per system size (currently twenty). The variation of the logarithm of the likelihood, for a single sytem size as a function of b and m is given in figure 7.2. The differentiations, with respect to the parameters m and b_j, are given

$$\frac{\partial \ln \Lambda}{\partial m} = \frac{N}{m} + \sum_{<i,j>} \left(\ln t_{ij} - \ln b_j \right) - \sum_{<i,j>} \left[\left(\frac{t_{ij}}{b_j} \right)^m \ln \left(\frac{t_{ij}}{b_j} \right) \right] \quad (7.5)$$

$$\frac{\partial \ln \Lambda}{\partial b_j} = -\frac{\zeta m}{b_j} + \frac{m}{b_j} \sum_{<i>} \left[\left(\frac{t_{ij}}{b_j} \right)^m \right] \quad (7.6)$$

where N is the number of observations, regardless of system size (currently one hundred). Maximisation is obtained by setting the above equations to zero; the

142

following relations ensue [151]

$$F(m) = \frac{N}{m} + \sum_{<i,j>} \ln t_{ij} - N\frac{\sum_{<i,j>}\left(t_{ij}^m \ln t_{ij}\right)}{\sum_{<i,j>} t_{ij}^m} = 0 \qquad (7.7)$$

$$\frac{d\,F(m)}{d\,m} = -\frac{N}{m^2} - N\frac{\left[\sum_{<i,j>} t_{ij}^m\right]\left[\sum_{<i,j>} t_{ij}^m \left(\ln t_{ij}\right)^2\right] - \left[\sum_{<i,j>}\left(t_{ij}^m \ln t_{ij}\right)\right]^2}{\left[\sum_{<i,j>} t_{ij}^m\right]^2} \qquad (7.8)$$

The size dependency within b_j is no longer present, and therefore m is solved for all sizes simultaneously. The Newton-Raphson method is utilised to obtain the optimum estimator of m (for which both the function and its derivative are required [153]), which upon substitution into equation 7.6, gives the estimates of the size dependent quantities b_j. The constants m and b_j are therefore obtainable, as a function of a, and therefore the estimation of a can be performed using the bisection method.

In order to estimate the location parameter, the following derivative is considered

$$\frac{\partial \ln \Lambda}{\partial a} = -(m-1)\sum_{<i,j>} \frac{1}{x_{ij} - a} + \sum_{<i,j>} \frac{m}{b_j}\left(\frac{x_{ij} - a}{b_j}\right)^{m-1} \qquad (7.9)$$

upon setting to zero, this equation can be solved through the bisection method [153], as the parameters m and b_j can be obtained as functions of a. In order to solve the above expression the upper and lower bounds of a must be determined. As the parameter a represents the lowest value of stress in the distribution curve, the value must be positive (zero probability of attaining a given stress in the system if no stress is applied) and less than the minimum observed value (probability of an observation occuring must be non-zero). The necessary bounds are therefore zero, and the minimum observed value.

The empirical cumulative distribution function is obtained by considering the data in ascending order and assigning cumulative probabilities as $c(x) = \frac{i}{n+1}$, where i is

the rank of the specimen in order of increasing measured value of x [151]. The data corresponding to the attainments of a maximum stress (maximum stresses of 0.5, 1, 1.5, and 2 are considered) are given in figures 7.3 and 7.4, along with the numerical fits using the technique described above. The four figures correspond to the same systems, but for different levels of stress, and are therefore similar.

The data reveals an expected shift of the curves towards the left with increasing system size; the data corresponding with system sizes of 45 and 50 unit lengths, do not adhere to this trend, although the fitted curves are very close, and the raw data exhibits appreciable scatter. The small sample size is thought to be responsible for this scatter.

The size dependence of b_j, assigned earlier, dictates that the variation of b_j^m with the inverse of the volume should be linear and possess no intercept. The volume considered here is not the volume of the system, but the active volume over which interactions between voids may occur; defined as $(L_* - 4R_*^{ave})^3$.

The confidence in b_j^m is obtained from the confidence levels of the parameters b and m, with the use of partial differentials, from the relation

$$\left(\Delta b_j^m \right)^2 = \left(\frac{\partial (b_j^m)}{\partial b_j} \right)^2 \Delta b_j^2 + \left(\frac{\partial (b_j^m)}{\partial m} \right)^2 \Delta m^2 \qquad (7.10)$$

The confidence levels in the parameters b and m can be estimated by following similar arguements to those in the sequential probability ratio test [154]. The test is based upon the comparison between two hypotheses, in order to ascertain within a given confidence which hypothesis is true. In the current case the two hypotheses
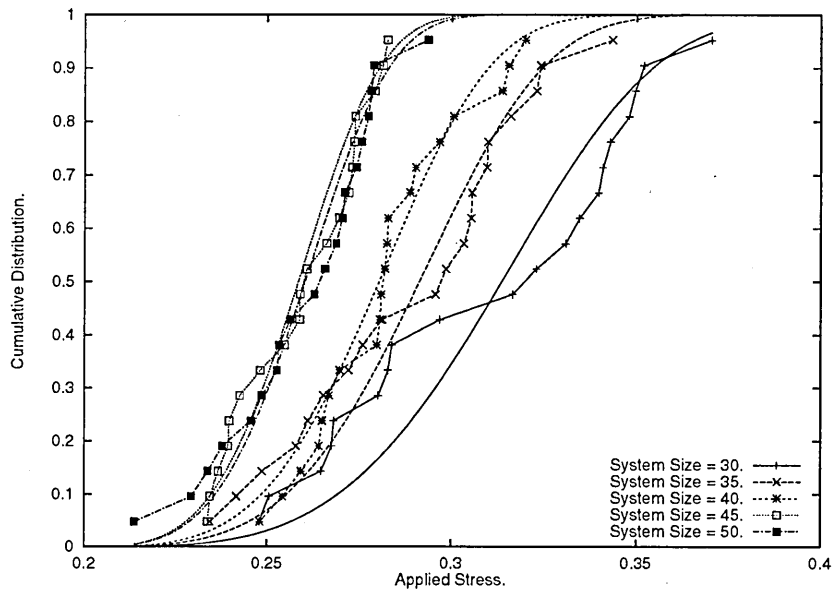
(a)
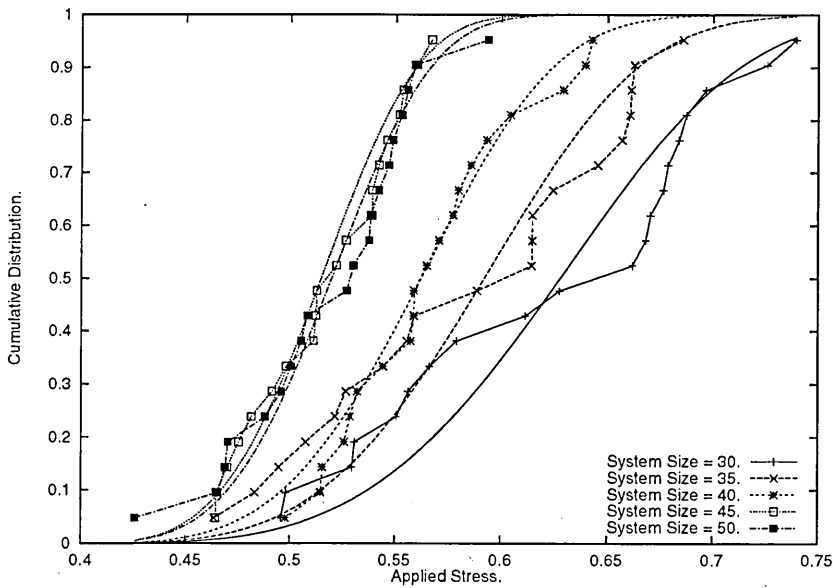
(b)

Figure 7.3: The empirical cumulative distribution functions from simulation data corresponding to the attainment of a maximum normal stress of (a) 0.5 and (b) 1.0, and the estimated functional forms obtained via the maximum likelihood method.

145
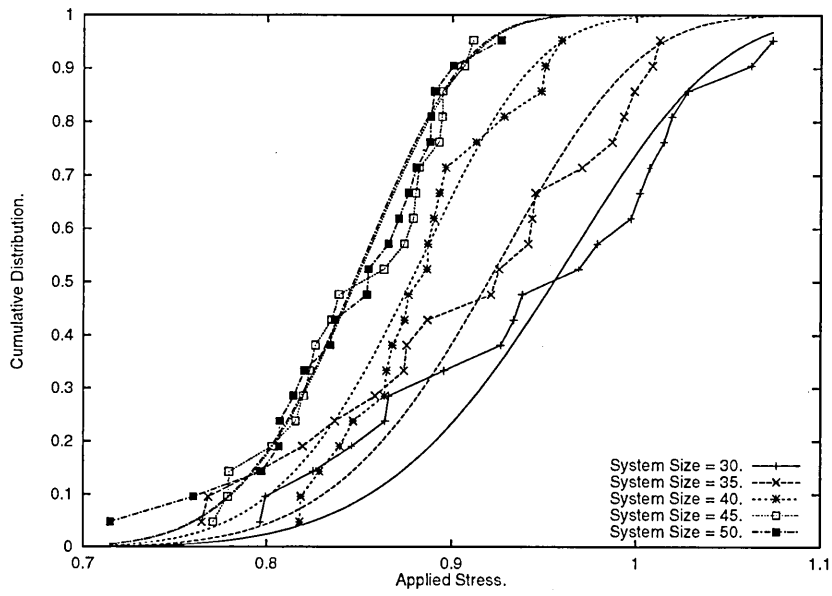
(a)
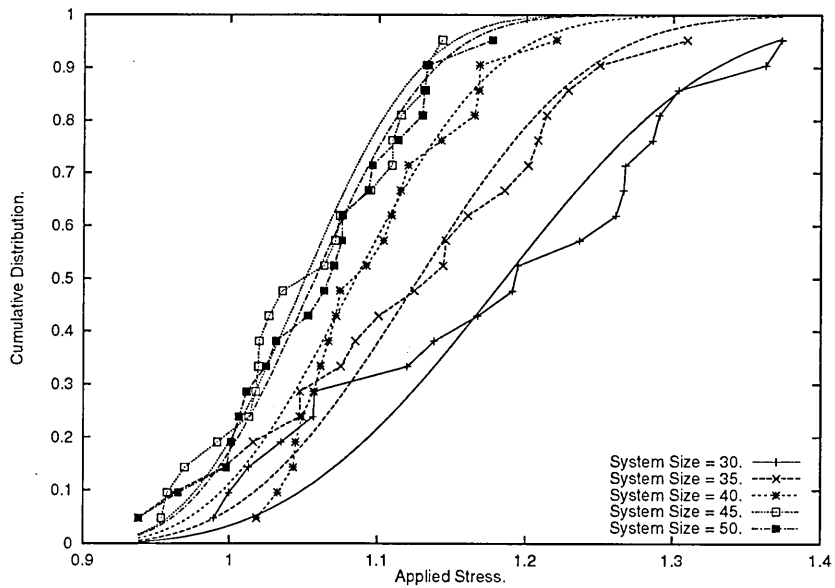
(b)

Figure 7.4: The empirical cumulative distribution functions from simulation data corresponding to the attainment of a maximum normal stress of (a) 1.5 and (b) 2.0, and the estimated functional forms obtained via the maximum likelihood method.

are:

- $H1$:- the hypothesis to be accepted, within various confidences, is that the estimators arrived at through the maximisation of the likelihood function are true.

- $H2$:- the hypothesis to be rejected considers the estimators to be true, except for the estimation of one parameter, which is varied.

The test is based upon the ratio of two likelihoods (corresponding to the two hypotheses) being less than a given constant, A. The constant is estimated from the relation $A \approx \frac{1-\beta}{\alpha}$, where α is the prescribed strength (for 95% confidence $\alpha = 0.05$) of $H1$ being accepted when $H2$ is true, and β is the prescribed strength of $H2$ being accepted when $H1$ is true (both α and β are assumed to be the same). The value of the logarithm of the likelihood, at which a given confidence is estimated, lies on the contour $\ln \Lambda = \ln \Lambda_{max} - \ln \left(\frac{1-\alpha}{\alpha} \right)$. In figure 7.2 contours corresponding to 95% confidence ($\ln \Lambda = 34.8$), 90% confidence ($\ln \Lambda = 35.6$), and 80% confidence ($\ln \Lambda = 36.4$) are estimated; the maximum $\ln \Lambda_{max} = 37.8$.

In order to obtain confidence levels, for a given parameter, the value of the paramter is increased, or decreased, until the logarithm of the likelihood is found to cross the contour of prescribed confidence (this is achieved via the bisection method). In this manner positive and negative confidence levels of all parameters are obtained, and therefore the positive and negative confidence levels of b_j^m.

The variation of b_j^m with the inverse of the volume is shown in figures 7.5 and 7.6, and the error bars correspond with estimated confidence levels of 95%, 90% and 80%. A straight line fit, with zero intercept (independent of confidence levels), is included. The general trend does appear linear, although the data points corresponding with system sizes 45 and 50 unit lengths deviate from this trend. The error bars are substantial, due to the small sample sizes considered and the resultant scatter in the data. That said, the results are in reasonable agreement, and the effects of system size upon the system would appear to be in line with theoretical expectations.

7.2 Volume fraction variation.

The effects upon varying the volume fraction of voids are investigated. The systems considered, are of size $L^* = 40$, and consist of voids belonging to the same size distribution as depicted in figure 7.1a. The number of particles are drawn from four distributions, proportionally related to the distribution considered in figure 7.1b, but possessing an average number of voids of 4, 8, 16, and 32. The distribution of strength and toughness in the systems is investigated and an estimate of the lower bound is obtained. The effects of volume fraction upon the strength and toughness are ascertained. Twenty systems are considered for each volume fraction distribution, therefore eigthy simulations were conducted altogether.

The statistical likelihood of large voids occurring, whilst small, is not insignificant and as larger void volume fractions are considered this can result in statistical bias-

148
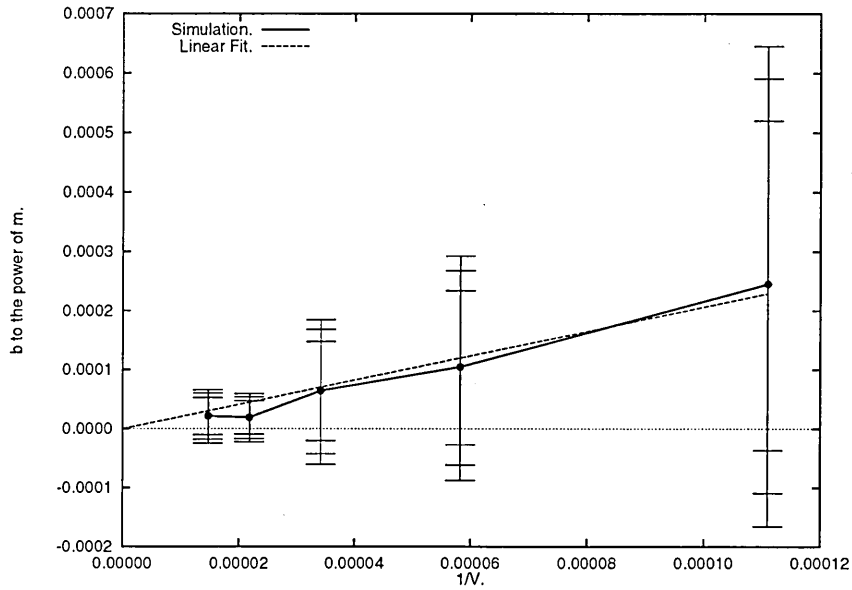
(a)
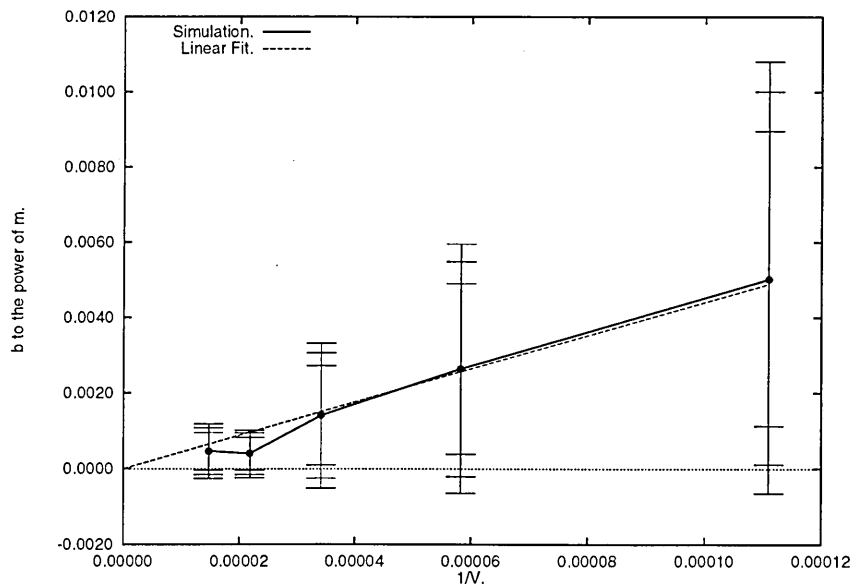
(b)

Figure 7.5: The variation of the estimated system size dependence (b^m) with the inverse of the volume from simulation data corresponding to the attainment of a maximum stress of (a) 0.5 and (b) 1.0. The error bars correspond with estimated confidence levels of 95%, 90% and 80%. A straight line fit, with zero intercept (independent of confidence levels), is included.

149
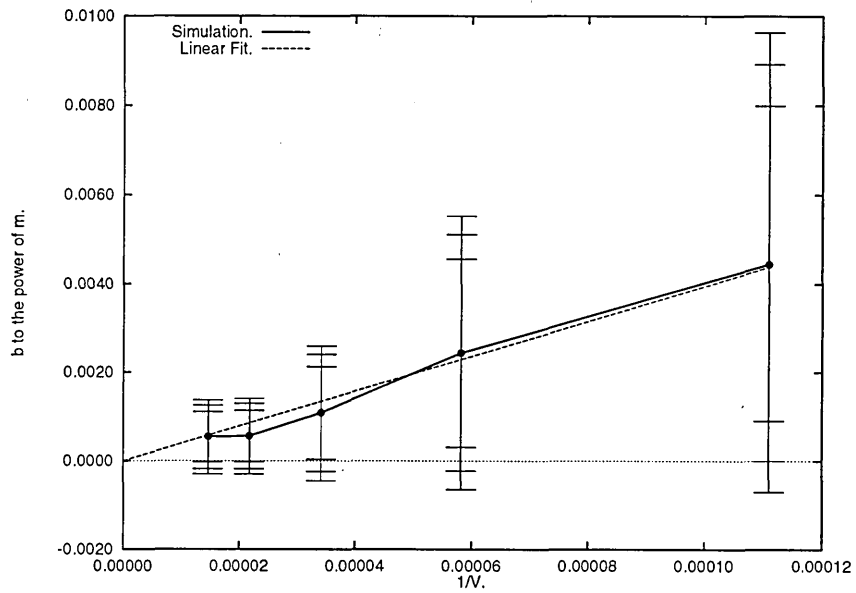
(a)
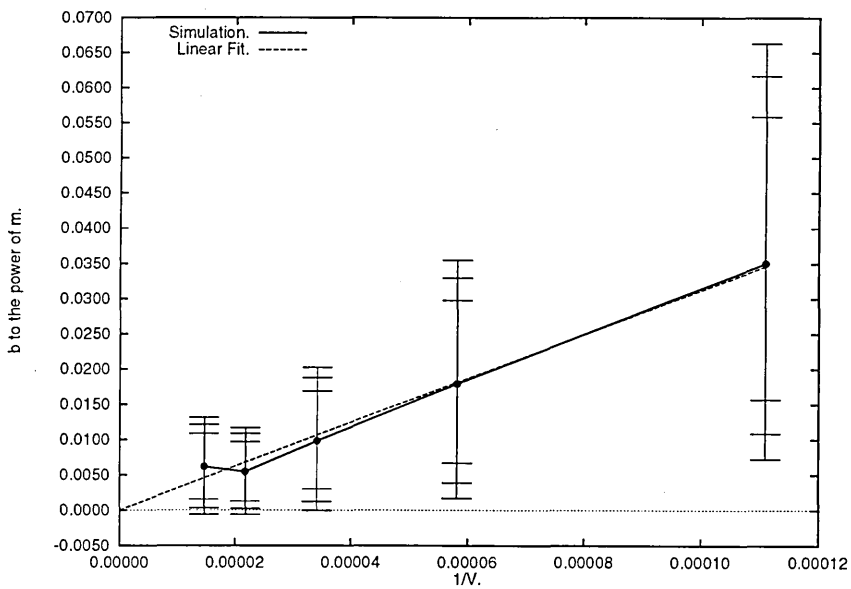
(b)

Figure 7.6: The variation of the estimated system size dependence (b^m) with the inverse of the volume from simulation data corresponding to the attainment of a maximum stress of (a) 1.5 and (b) 2.0. The error bars correspond with estimated confidence levels of 95%, 90% and 80%. A straight line fit, with zero intercept (independent of confidence levels), is included.

ing. In order confidently to simulate the inclusion of voids, a minimum separation between voids is presumed in order to exclude void overlap, whilst voids are precluded from the perimeter of the simulation to minimise surface effects. As the quantity of voids considered is increased, it is not necessarily possible to include multiple voids of larger dimensions. This can bias the statistical evaluation of the volume fraction; whilst at low volume fractions a single large void can occur, in more dense systems the numbers of large voids are limited. This effect could be reduced by considering increased system sizes.

In the previous section the size effects of the simulation were theoretically predicted to only modify the scale parameter of the Weibull function (responsible for dispersion effects), whilst the Weibull modulus (responsible for shape effects) is invariant with system size. This is no longer necessarily the case, with systems considering different distributions in the number of voids. The location parameter provides a minimum value of the distribution (a lower bound) and, assuming that this is a consequence of unfavourable void interactions, is therefore the same in all systems.

The natural logarithm of the likelihood function is now given by

$$\ln \Lambda = \sum_{<j>} \left[n \ln \left(\frac{m_j}{b_j} \right) \right] + \sum_{<i,j>} \left[(m_j - 1) \left(\ln t_{ij} - \ln b_j \right) \right] + \sum_{<i,j>} \left[- \left(\frac{t_{ij}}{b_j} \right)^{m_j} \right] \quad (7.11)$$

where j now represents the distribution dependence; the Newton-Raphson method is employed to maximise the likelihood function, with respect to the scale parameters and the Weibull moduli, whilst the bisection method is subsequently applied to obtain the location parameter. It should be noted that the Newton-raphson method is applied four times, for each of the distribution dependent sets, but maximising of

the likelihood of each of these sets results in an overall maximisation of the likelihood function.

The empirical cumulative distribution function, of both the strength and toughness from the simulations, and the estimated cumulative distribution function, obtained via the maximum likelihood method, are presented in figures 7.7. The different distributions correspond to the average number of voids in the system: A) 4 voids, B) 8 voids, C) 16 voids, and D) 32 voids. The resultant form of the distributions are varied (a consequence of allowing variations in the Weibull moduli), whilst the scale parameter decreases with increasing volume fraction, indicating lower dispersions.

The lower bound strength and toughness are given by the location parameters. The estimator of the location parameter for the strength distributions is 1.29, and for the toughness distributions is 0.067; these correspond, in dimensional quantities, to 677MPa and 35MPa respectively.

The detrimental effects of increasing the volume fraction of voids is depicted in figures 7.8, which exhibit the variantions in strength and toughness. The variations in volume fraction for the four distributions considered are presented and, despite considerable scatter, the detrimental trends in both strength and toughness, with respect to increasing volume fractions, are discernable.
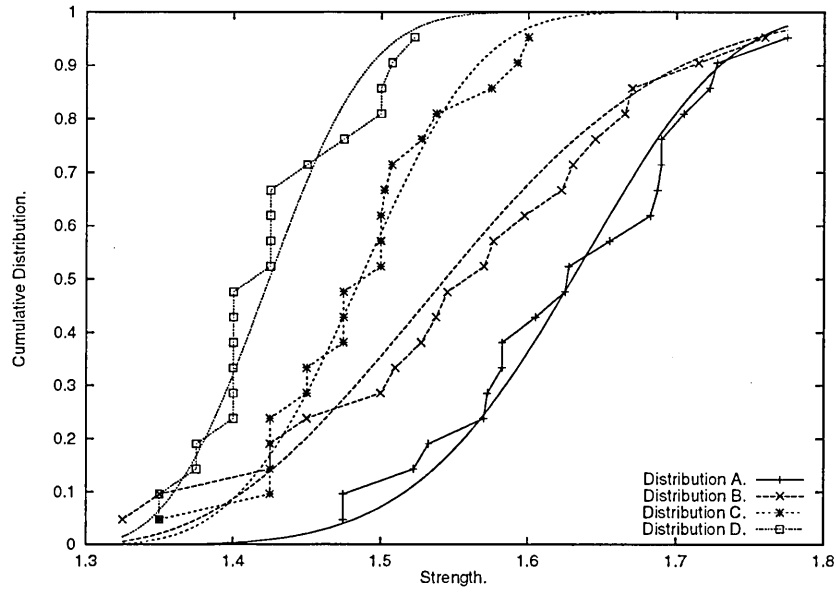
(a)
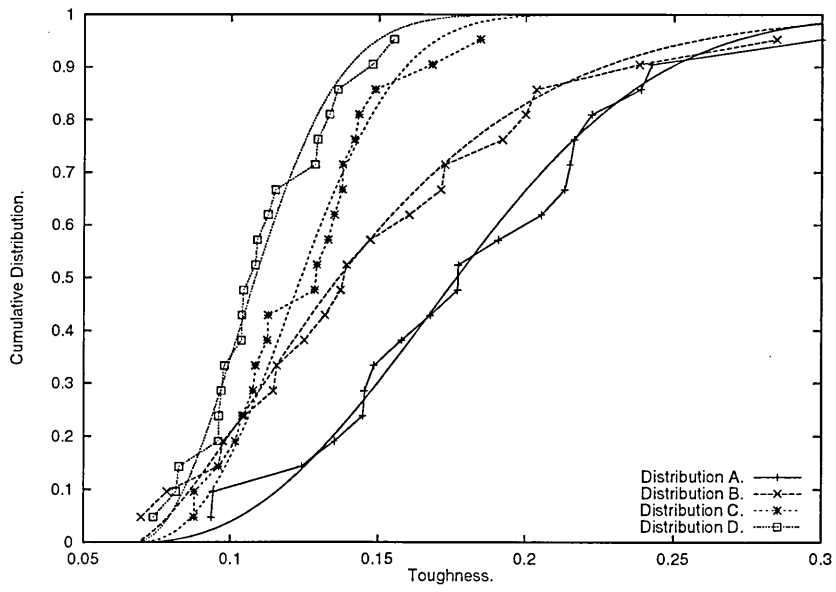
(b)

Figure 7.7: The empirical cumulative distribution functions from simulation data corresponding to the (a) strength and (b) toughness of systems with different distributions of voids, and the estimated functional forms obtained via the maximum likelihood method. The Distributions correspond to the average number of particles: A) 4 voids, B) 8 voids, C) 16 voids, and D) 32 voids.

153
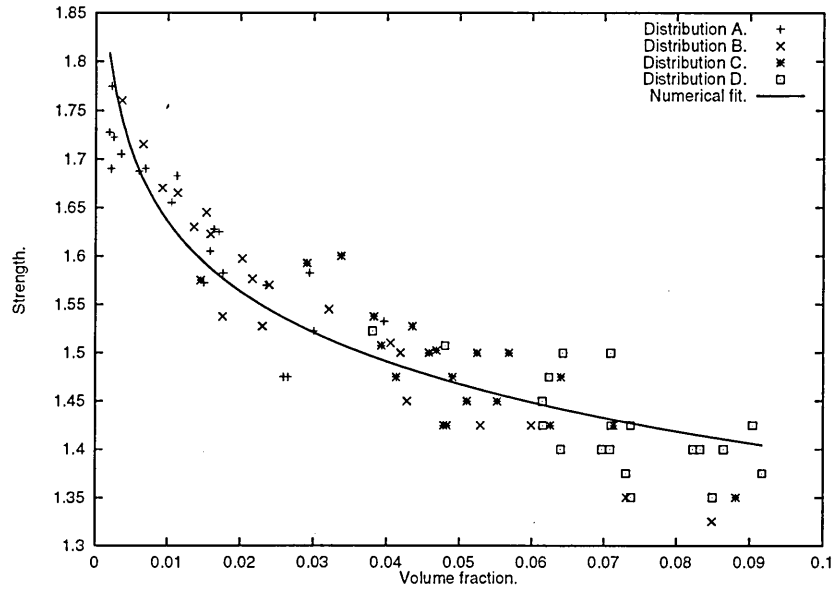
(a)
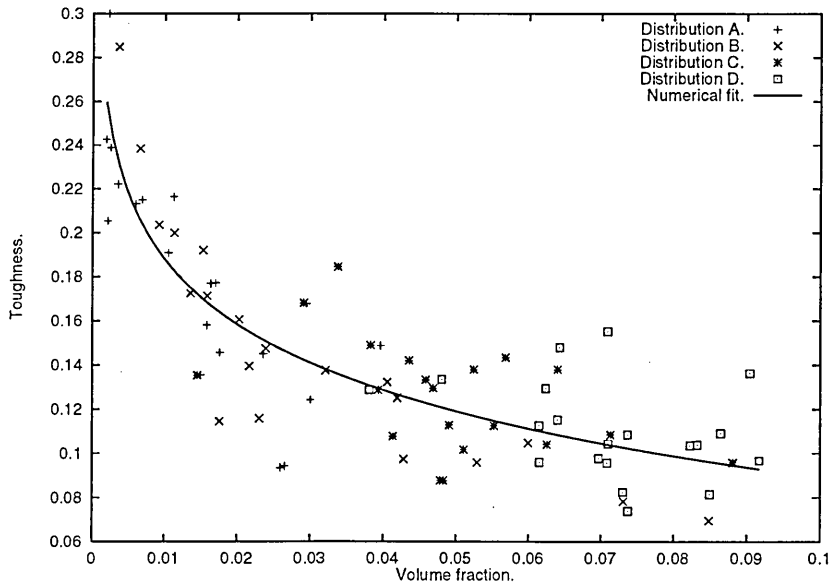
(b)

Figure 7.8: The variation of (a) strength and (b) toughness of systems with different distributions of voids, as a function of the void volume fraction. The Distributions correspond to the average number of particles: A) 4 voids, B) 8 voids, C) 16 voids, and D) 32 voids.

154

7.3 Conclusions

A lattice spring model reflecting the statistical nature of the microstructural defects (voids in this case) has been implemented in order to elucidate macroscopic trends. The probability of finding a given stress intensity in systems of varying size, as a function of applied stress, have been investigated. The size dependency was found to be within reasonable agreement with theoretical expectations, despite considerable scatter. Statistical trends in the simulation data are therefore distinguishable when small sample sizes are considered.

The effects upon varying the volume fraction of voids in an austenitic steel have been investigated; the consequence of void nucleation, and the resultant degradation that may ensue, have not been considered. Assuming a critical normal strain of 60% in the matrix, the material specific lower bound strength and toughness where ascertained. The deleterious effect upon increasing the void volume fraction was elucidated, although as a consequence of small system size and tensile nonlinearity the scatter in toughness data is considerable.

The potential for employing a LSM in modelling statistically variable macroscopic parameters, such as the strength and toughness of a given material, has been successfully established. The method could be used for the large scale study of the effects of voids or particles, although particulate systems are more computationally expensive as extensive damage is accumulated prior to catastrophic failure.

Chapter 8

Conclusions and future work.

8.1 Conclusion.

A three-dimensional model of the deformation and quasi-static fracture of hetero-geneous systems has been presented within this thesis. The model is governed by continuum mechanics and is therefore size independent, unless directly related to the dimensional quantities of a real material. The results are, consequently, applicable to many classes of materials.

8.1.1 Inhomogeniety problem.

The ability of the model to replicate the elastic deformation fields of a single particle system have been validated with respect to the analytical results of Eshelby. A comparison was made between results from a discrete approximation to a spherical

156

particle and the theoretical results which assume a perfectly spherical particle. It was found that the model predicts the correct stress and strain fields with reasonable accord, but is sensitive to the size of the particle. The agreement of the model with theoretical expectations is also dependent upon the ratio of particle to matrix elastic moduli. The development of incipient plastic deformation fields in the matrix about a single inclusion have compared well with alternative numerical results which were obtained from the literature, principally those of Wilner [1].

8.1.2   Simulation of inclusions in austenitic steel.

The model has been applied to the investigation of the ductile fracture of particle systems, typical of those found in austenitic steels. The deformation fields were investigated around three spherical inclusions: a Fe3C particle (stiffer than matrix), a MnS particle (initially softer than the matrix, but subsequent to plastic deformation, becomes stiffer) and a void (softer than matrix). Interesting non-uniform stress fields within the stiffer particles, subsequent to plastic deformation in the surrounding matrix, were observed. The concentration of the normal stress field in the centre of the particle, and the reduction in the tensile direction towards the particle-matrix interface has been remarked upon in the literature. The concentrations in the equatorial plane have not been mentioned, and therefore it is unknown if this effect is an artefact of the simulation technique, or is a genuine phenomenon. A discrepancy between the concentration of stress within the particles simulated here, and those simulated by Xu et al [58], was accounted for through the simulation of

a harder particle (corresponding to the ratio of elastic moduli of Al to SiC) and imposing a linear hardening regime upon the plastic flow relation of the matrix; the choice of the constitutive relation was found to have a profound effect on the stress concentration factor.

The observed decohesion of spherical Fe3C and MnS particles, and internal fracture of elongated MnS particles, were found to be concordant with experimental observations, whilst providing unique insights into both, via processes of damage accumulation and the accompanying deformation fields. The spherical MnS particle was observed to debond at a lower applied stress than the Fe3C particle, and then continued to debond completely; in contrast the Fe3C particle only underwent partial decohesion prior to crack propagation into the steel matrix.

The simulation of internal fracture within elongated MnS particles revealed that the governing phenomenon was the stress concentration in the centre of the particle. Particles possessing larger aspect ratios were observed to fracture at lower levels of applied stress, as expected, but result in stronger and tougher materials. This mechanism, in which internal fracture creates a series of voids which shield each other, could be relevent to real materials. The damage accumulation about the internal cracks in the particle, subsequent to particle bifurcation and preceding crack propagation into the matrix, may also be influential. The fracture criterion employed in the current model is based upon critical normal stress and strain fields perpendicular to the fracture surface being formed. If shearing forces (or an energy based criterion) were to be considered, once the internal fracture of the particle reached

the interface, damage may not be further accumulated in the particle. The shearing forces at the interface may alternatively enable decohesion of the particle from the matrix in the regions surrounding the internal cracks. This could have the effect of dissipating the stress and strain concentrations in a different manner. It should also be noted that potential damage of the particle or the interface prior to deformation, as a consequence of material processing, has not been accounted for.

The interaction between two inclusions was investigated; systems contained either two voids or two Fe3C particles. Orientating the inclusions at 45 degrees to the tensile direction was generally observed to have a detrimental effect upon both the stress fields and toughnesses of the systems considered. The system containing two Fe3C particles in close proximity proved the only exception to this: here, particles orientated normal to the tensile direction appeared to be more deleterious. In order to minimise discretisation effects within the simulations of systems containing two inclusions, the inclusions were always centred on a node and were of consistent size, but it should be noted that the discretisation of the inclusions along the axis of the simulation ({100} directions) will be different from the discretisation in a diagonal direction ({110} directions).

The voids do not possess interfacial properties, unlike the particles which possess properties interpolated between the particle and matrix characteristics, and are therefore slightly larger. Despite this difference in size, the systems containing particles are consistently observed to possess lower strength and toughness. It is therefore concluded that the void nucleation process of particle decohesion is signif-

icant; regional variations in stress and strain concentrations may be the influential factor.

8.1.3   Simulation of random microstructures.

Random microstructures have been considered which correspond to those found experimentally in austenitic weld steels; the inclusions are assumed to be voids. It is generally considered that inclusions, whose size are of the order of a micron, are the smallest that can be modelled with continuum theory. The voids that have been considered here range upwards from around half a micron, but this is not believed to be significant.

The system sizes were varied and the level of maximum stress in a number of randomly generated microstructures, were considered as a function of applied stress. The probability of a maximum level of stress occurring in the simulation, for a given applied stress, was investigated through the application of Weibull statistics. The system size dependence is in good agreement with theoretical expectations, despite only twenty samples being considered and the resulting uncertainty, associated with the estimation of the size dependent parameters, being significantly large.

The effects of varying the average number of particles whilst maintaining the same system size allowed the effects of void volume fraction to be studied. The system is deformed until catastrophic fracture occurs; as the system only consists of voids, and crack tip blunting is not considered, only relatively small levels of fracture are

required. A detrimental effect, upon the strength and toughness of a material, was generally observed as the volume fraction of voids was increased.

The volume fractions were limited due to the size of the system considered. In order to correctly model the plastic deformation between inclusions a minimum separation of a unit length must be imposed; the plastic deformation between two matrix nodes must be permitted. As the system size is increased, either the number of voids considered or the accuracy with which the system is simulated may be increased. Increasing the number of particles will also allow larger particles (although statistically less likely than smaller particles) to occur more often. Currently the probability of two large voids occurring does not appear to be twice the probability of a single large void occurring in the system, as it is logistically difficult to fit multiple large inclusions in the simulation.

In order to gain statistical data from particulate systems, such as strength and toughness, the damage accumulation preceding catastrophic failure must be simulated. The simulation of particle debonding or fracture will increase the computational expenditure, but not prohibitively.

8.2 Future work.

The plastic deformation employed within the current study is isotropic, but not volume conserving. Whilst this may prove adequate for incipient plastic deformation, the large levels of plastic deformation simulated in the current study requires

161

a Poisson's ratio greater than a quarter. It may be possible to include such effects by removing the inherent symmetry of the model, and therefore the isotropic conditions that are imposed; for example, making bonds orientated perpendicular to the local principle stress vector softer than bonds which are orientated parallel. Alternatively multi-body potentials could be considered, although this would increase the computational expense of the technique.

The plasticity algorithm upon unloading assumes a linear response, the elastic moduli corresponding to the current stress level divided by the maximum deformation previously experienced. Whilst this is adequate for gradual unloading, during large plastic deformation in the matrix this can result in negative spikes in the deformation fields subsequent to bond removal. Although this affects the wake of the crack, and does not appear to influence the propagation of fracture (currently propagation into the matrix is invariably catastrophic) it may be possible to identify such areas and treat them separately; presumably through treating the area as a boundary and imposing constant relative displacements.

The deformation at the crack tip is limited in resolution to the spacing of the underlying lattice, and therefore crack tip blunting is a difficult effect to incorporate. It may be possible to modify the fracture criteria, possibly through the incorporation of the derivatives of the displacement fields, to replicate crack tip blunting effects. This is an area which may benefit from information gained through simulations at smaller length scales, using alternative modelling techniques.

The fracture criteria used in this thesis were based on either a critical normal strain

(ductile matrix) or a critical normal stress (brittle particle and interface). As mentioned above, the criteria could be extended to include shearing components of the deformation fields. Although alternative fracture criteria may be considered in the future; for example, the nonlinear interfacial property described by Needleman [61] could be adopted.

The simulation is currently driven through the iterative application of constant forces at the system boundaries. In order to vary the boundary conditions to allow the system to be driven by strain increments, the conjugate gradient solver currently employed would have to be modified to solve the resulting asymmetric matrix, which describes the system; this would consequently enable the extension of the boundary conditions to introduce periodicity. The boundary conditions could potentially be interpolated from a region within another simulation, which models the macroscopic fields of a notched specimen.

In summary, the continuum mechanical bahaviour of an austenitic steel has been represented by a lattice model, where nonlinear deformation and fracture have been considered, whilst maintaining the linearity of the model. Reasonable agreement between both theoretical and experimental expectations, and the results obtained from LSM simulations, have been observed in the modelling of heterogeneous systems. The computational efficiency of the Lattice Spring Model is considered to be the principal advantage over alternative numerical methods.

Bibliography

[1] B.Wilner, *J. Mech. Phys. Solids*, **36:2**, 141-165 (1988).

[2] J.D.Eshelby, *Proc. Roy. Soc. A*, **241**, 376-396 (1957).

[3] J.D.Eshelby, *Proc. Roy. Soc. A*, **252**, 561-569 (1959).

[4] J.D.Eshelby, *Prog. Solid Mech.*, **2**, 88-139 (1961).

[5] E.Orowan, *Reports Prog. Phys.*, **12**, 185 (1949).

[6] R.H.Van Stone, T.B.Cox, J.R.Low Jr and J.A.Psioda, *Int. Met. Rev.*, **30:4**, 157-179 (1985).

[7] W.M.Garrison Jr and N.R.Moody, *J. Phys. Chem. Solids*, **48:11**, 1035-1074 (1987).

[8] F.Erdogan, *Int. J. Solids Structures*, **37:1-2**, 171-183 (2000).

[9] A.A.Griffith, *Phil. Trans. Roy. Soc. London*, **A221**, 163-198 (1921).

[10] C.J.McMahon and M.Cohen, *Acta Met.*, **13**, 591-604 (1965).

[11] W.Weibull, *J. Applied Mech.*, **18**, 293-297 (1951).

[12] R.O.Ritchie, J.F.Knott, and J.R.Rice, *J. Mech. Phys. Solids*, **21**, 395-410 (1973).

[13] P.F.Thomason, *Ductile Fracture of Metals*, Pergamon Press (1990).

[14] S.H.Goods and L.M.Brown, *Acta Metall.*, **27**, 1-15 (1979).

[15] A.S.Argon and J.Im, *Met. Trans. A*, **6A**, 825-838 (1975).

[16] K.Tanaka, T.Mori, and T.Nakamura, *Philos. Mag.*, **21**, 267-279 (1970).

[17] M.F.Ashby, *Phil. Mag.*, **14**, 1157-1178 (1966).

[18] T.B.Cox and J.R.Low Jr, *Met. Trans.*, **5**, 1457-1470 (1974).

[19] F.A.McClintock, *J. Appl. Mech.*, 363-371 (1963).

[20] J.R.Rice and D.M.Tracey, *J. Mech. Phys. Solids*, **17**, 201-217 (1969).

[21] W.Roberts, B.Lehtinen, and K.E.Easterling, *Acta Metall.*, **24**, 745-758 (1976).

[22] A.R.Rosenfield, *Met. rev.*, **13:121**, 29-40 (1968).

[23] C.D.Beachem, *Trans. Amer. Soc. Metals*, **56**, 318-326 (1963).

[24] C.D.Beachem and G.R.Yoder, *Met. Trans.*, **4**, 1145-1153 (1973).

[25] M.Isacsson and T.Narstrom, *Mat. Sci. Eng.*, **A241**, 169-178 (1998).

[26] J.P.Bandstra, D.M.Goto, and D.A.Koss, *Mat. Sci. Eng.*, **A249**, 46-54 (1998).

[27] Higgins R.A, *Properties of Engineering Materials (Second Edition)*, Edward Arnold (1994).

[28] D.Brooksbank and K.W.Andrews, *J. Iron Steel Inst.*, 595-599 (1968).

[29] S.Jun, D.Zengjie, L.Zhonghua, and T.Mingjing, *Int. J. Fracture*, **42**, R39-R42 (1990).

[30] S.Jun, *Int. J. Fracture*, **44**, R51-R56 (1990).

[31] D.Kwon, S.Lee, and K.M.Cho, *Mat. Sci. Eng.*, **A159**, 151-157 (1992).

[32] L.E.Wood and L.H.Van Vlack, *Trans. Amer. Soc. Metals*, **56**, 770-772 (1963).

[33] B.R.Butcher and P.L.Allen, *Metal Science*, 462-471 (1977).

[34] D.I.Swan, *Personal correspondance.*

[35] M.Shibata and K.Ono, *Acta Metall.*, **26**, 921-932 (1978).

[36] D.Jaffrey, *Metals Forum*, **5:4**, 217-227 (1982).

[37] F.M.Beremin, *Met. Trans. A*, **12A**, 723-731 (1981).

[38] O.N.Mryasov and A.J.Freeman, *Mat. Sci. Eng.*, **A260**, 80-93 (1999).

[39] F.F.Abraham, D.Brodbeck, W.E.Rudge, J.Q.Broughton, D.Schnieder, B.Land, D.Lifka, J.Gerner, M.Rosenkrantz, and J.Skovira, *Modelling Simul. Mater. Sci. Eng.*, **6**, 639-670 (1998).

[40] W.T.Ashurst and W.G.Hoover, *Phys. Rev. B*, **14:4**, 1465-1473 (1976).

[41] J.E.Lennard-Jones, *Proc. Roy. Soc. London A*, **106**, 463 (1924).

[42] M.Born and K.Huang, *Dynamical Theory of Crystal Lattices*, Oxford University Press (1954).

[43] M.Mullins, *Int. J. Fracture*, **24**, 189-196 (1984).

[44] R.A.Johnson, *Phys. Rev. B*, **6:6**, 2094-2099 (1972).

[45] M.S.Daw and M.I.Baskes, *Phys. Rev. Lett.*, **50:17**, 1285-1288 (1983).

[46] M.S.Daw and M.I.Baskes, *Phys. Rev. B*, **29:12**, 6443-6453 (1984).

[47] M.I.Baskes, *Mater. Chem. Phys.*, **50**, 152-158 (1997).

[48] R.Pérez and P.Gumbsch, *Acta Mater.*, **48**, 4517-4530 (2000).

[49] F.F.Abraham, J.Q.Broughton, N.Bernstein, and E.Kaxiras, *Europhys. Lett.*, **44:6**, 783-787 (1998).

[50] J.C.H.Spence, *Acta Mater.*, **47**, 4153-4159 (1999).

[51] S.J.Zhou, P.S.Lomdahl, A.F.Voter, and B.L.Holian, *Engng. Fract. Mech.*, **61**, 173-187 (1998).

[52] P.J.Withers, W.M.Stobbs, and O.B.Pedersen, *Acta Metall.*, **37:11**, 3061-3084 (1989).

[53] W.C.Johnson and J.K.Lee, *J. Appl. Mech.*, **49**, 312-318 (1982).

[54] A.Roatta, P.A.Turner, M.A.Bertinetti, and R.E.Bolmaro, *Mater. Sci. Eng.*, **A229**, 203-218 (1997).

[55] T.Christman, A.Needleman, and S.Suresh, *Acta Metall.*, **37:11**, 3029-3050 (1989).

[56] J.Llorca, A.Needleman, and S.Suresh, *Acta Met. et Mater.*, **39:10**, 2317-2334 (1991).

[57] C.L.Hom and R.M.McMeeking, *Int. J. Plasticity*, **7**, 255-274 (1991).

[58] X.Q.Xu and D.F.Watt, *Acta Mater.*, **44:2**, 801-811 (1996).

[59] D.F.Watt, X.Q.Xu, and D.J.Lloyd, *Acta Mater.*, **44:2**, 789-799 (1996).

[60] C.I.A.Thomson, M.J.Worswick, A.K.Pilkey, D.J.Lloyd, and G.Burger, *J. Mech. Phys. Solids*, **47**, 1-26 (1999).

[61] A.Needleman, *J. Appl. Mech.*, **54**, 525-531 (1987).

[62] A.A.Gusev, *J. Mech. Phys. Solids*, **45:9**, 1449-1459 (1997).

[63] H.J.Böhm and W.Han, *Modelling Simul. Mater. Sci. Eng.*, **9**, 47-65 (2001).

[64] L.Mishnaevsky Jr, M.Dong, S.Honle, and S.Schmauder, *Comp. Mater. Sci.*, **16**, 133-143 (1999).

[65] J.Wulf, Th.Steinkopff, and H.F.Fischmeister, *Acta Mater.*, **44:5**, 1765-1779 (1996).

[66] A.L.Gurson, *J. Engng. Mater. Tech.*, **99**, 2-14 (1977).

[67] V.Tvergaard and A.Needleman, *Acta Metall.*, **32:1**, 157-169 (1984).

[68] L.Xia and F.C.Shih, *J. Mech. Phys. Solids*, **43:2**, 233-259 (1995).

[69] J.Lemaitre, *Engng. Fract. Mech.*, **25:5/6**, 523-537 (1986).

[70] S.Renevey, S.Carassou, B.Marini, C.Eripret, and A.Pineau, *J. de Physique IV*, **6**, 343-351 (1996).

[71] S.Ghosh and S.Moorthy, *Acta Mater.*, **46:3**, 965-982 (1998).

[72] L.I.Slepyan, *Sov. Phys. Dokl*, **26:5**, 538-540 (1981).

[73] A.Hrennikoff, *J. of Appl. Mech*, **12**, A169 (1941).

[74] B.Khang, G.G.Batrouni, S.Redner, L.de Arcangelis, and H.J.Herrmann, *Phys. Rev. B*, **37:13**, 7625-7637 (1988).

[75] M.C.Stephens and M.Sahimi, *Phys. Rev. B*, **36:16**, 8656-8659 (1987).

[76] J.Schmittbuhl and S.Roux, *Modelling Simul. Mater. Sci. Eng*, **2**, 21-52 (1994).

[77] A.Delaplace, G.Pijaudier-Cabot, and S.Roux, *J. Mech. Phys. Solids*, **44:1**, 99-136 (1996).

[78] S.Zapperi, A.Vespignani, and H.E.Stanley, *Nature*, **388:14**, 658-660 (1997).

[79] L. de Arcangelis and H.J.Herrmann, *Phys. Rev. B*, **39:4**, 2678-2684 (1989).

[80] G.G.Batrouni and A.Hansen, *Phys. Rev. Lett.*, **80:2**, 325-328 (1998).

[81] M.Ostoja-Starzewski, P.Y.Sheng, and I.Jasuik, *J. Eng. Mater. Tech.*, **116**, 384-391 (1994).

[82] G.N.Hassold and D.J.Srolovitz, *Phys. Rev. B*, **39:13**, 9273-9281 (1989).

[83] P.D.Beale and D.J.Srolovitz, *Phys. Rev. B*, **37:10**, 5500-5507 (1988).

[84] M.Sahimi and J.D.Goddard, *Phys. Rev. B*, **33:11**, 7848-7851 (1986).

[85] P.Meakin, G.Li, L.M.Sander, E.Louis, and F.Guinea, *J.Phys. A: Math. Gen.*, **22**, 1393-1403 (1989).

[86] O.Pla, R.Garcia-Molina, F.Guinea, and E.Louis, *Phys. Rev. B*, **41:16**, 11449-11456 (1990).

[87] A.R.Day, K.A.Snyder, E.J.Garoczi, and M.F.Thorpe, *J. Mech. Phys. Solids*, **40:5**, 1031-1051 (1992).

[88] K.A.Snyder, E.J.Garoczi, and A.R.Day, *J. Appl. Phys.*, **72:12**, 5948-5955 (1992).

[89] D.J.Srolovitz, *J.Am. Ceram. Soc.*, **71:5**, 362-369 (1988).

[90] S.P.Chen, R.LeSar, and A.D.Rollet, *Scripta Metall. et Mater.*, **28**, 1393-1398 (1993).

[91] A.J.C.Ladd, J.H.Kinney, and T.M.Breunig, *Phys. Rev. E*, **55:3**, 3271-3275 (1997).

[92] A.J.C.Ladd and J.H.Kinney, *Physica A*, **240**, 349-360 (1997).

[93] L.Monette and M.P.Anderson, *Modelling Simul. Mater. Sci. Eng*, **2**, 53-66 (1994).

[94] P.N.Sen and M.F.Thorpe, *Phys. Rev. B*, **15:8**, 4030-4038 (1977).

[95] H.Yan, G.Li, and L.M.Sander, *Europhys. Lett.*, **10:1**, 7-13 (1989).

[96] M.J.Calloway, D.J.Cleaver, and C.M.Care, *Internal report*, 1998, Sheffield Hallam University.

[97] G.Caldarelli, C.Castellano, and A.Petri, *Physica A*, **270**, 15-20 (1999).

[98] A.Parisi, G.Caldarelli, and L.Pietronero, *Physica A*, **280**, 161 (2000).

[99] P.N.Keating, *Phys. Rev.*, **145:2**, 637-645 (1966).

[100] J.G.Kirkwood, *J. Chem. Phys.*, **7**, 506-509 (1939).

[101] L.M.Schwartz, S.Feng, M.F.Thorpe, and P.N.Sen, *Phys. Rev. B*, **32:7**, 4607-4617 (1985).

[102] M.Ostoja-Starzewski, P.Y.Sheng and K.Alzebdeh, *Comp. Mater. Sci*, **7**, 82-93 (1996).

[103] M.Sahimi and S.Arbabi, *Phys. Rev. Lett.*, **68:5**, 608-611 (1992).

[104] L.Monette, M.P.Anderson, S.Ling, and G.S.Grest, *J. Mater. Sci*, **27**, 4393-4405 (1992).

[105] P.M.Duxbury and P.L.Leath, *Phys. Rev. B*, **49:18**, 12676-12687 (1994).

[106] S.Arbabi and M.Sahimi, *J.Phys. A: Math. Gen.*, **23**, 2211-2216 (1990).

[107] S.Arbabi and M.Sahimi, *Phys. Rev. B*, **41:1**, 772-775 (1990).

[108] J.W.Chung, A.Roos, and J.Th.M.De Hosson, *Phys. Rev. B*, **54:21**, 15094-15100 (1996).

[109] E.Schlangen and E.J.Garboczi, *Engng. Fract. Mech.*, **57:2-3**, 319-332 (1997).

[110] J.G.M.Van Mier, B.M.Chiaia and A.Vervuurt, *Comput. Methods Appl. Mech. Engng.*, **142**, 189-201 (1997).

[111] B.Chiaia, A.Vervuurt, and J.G.M. Van Mier, *Engng. Fract. Mech.*, **57:2-3**, 301-318 (1997).

[112] J.G.M. Van Mier and M.R.A. Van Vliet, *Construction and Building Materials*, **13**, 3-14 (1999).

[113] J.E.Bolander Jr and S.Saito, *Engng. Fract. Mech.*, **61**, 569-591 (1998).

[114] J.E.Bolander Jr and B.D.Le, *Construction and Building Materials*, **13**, 23-31 (1999).

[115] P.Meakin, *Science*, **252**, 226-233 (1991).

[116] T.Walmann and A.Malthe-Sorenssen, *Phys. Rev. Lett.*, **77:27**, 5393-5396 (1996).

[117] A.Malthe-Sorenssen, T.Walmann, J.Feder, T.Jossang, P.Meakin, and H.H.Hardy, *Phys. Rev. E*, **58:5**, 5548-5564 (1998).

[118] A.Gabrielli, R.Cafiero, and G.Caldarelli, *Europhys. Lett.*, **45:1**, 13-19 (1999).

[119] A.Jagota and S.J.Bennison, *Modelling Simul. Mater. Sci. Eng.*, **3**, 485-501 (1995).

[120] M.Vujosevic and D.Krajcinovic, *Int. J. Solids Structures*, **34:9**, 1105-1122 (1997).

[121] Y.Termonia and D.J. Walsh, *J. Mater. Sci.*, **24**, 247-251 (1989).

[122] A.Sauron, *Computer Modelling of Crack Growth in Rubber-Toughened Polymers*, SHU, Ph.D. Thesis (1997).

[123] W.A.Curtin, M.Pamel, and H.Scher, *Phys. Rev. B*, **55:18**, 12038-12060 (1997).

[124] Y.S.Li and P.M.Duxbury, *Phys. Rev. B*, **38:13**, 9257-9260 (1988).

[125] V.I.Raisanen, M.J.Alava, and R.M.Nieminen, *J. Appl Phys*, **82:8**, 3747-3753 (1997).

[126] M.Ostoja-Starzewski, *Int. J. Fracture*, **75**, R51-R57 (1996).

[127] L.Monette and M.P.Anderson, *Scripta Metall. et Mater.*, **28:9**, 1095-1100 (1993).

[128] M.P.Lopez-Sancho, F.Guinea, and E.Louis, *J. Phys. A: Math. Gen.*, **21**, L1079-L1083 (1988).

[129] S.Roux and A.Hansen, *J.Phys II France*, **2**, 1007-1021 (1992).

[130] M.J.Alava, M.E.J.Karttunen, and K.J.Niskanen, *Europhys. Lett.*, **32:2**, 143-148 (1995).

[131] M.J.Korteoja, A.Lukkarinen, K.Kaski, and K.J.Niskanen, *Phys. Rev. E*, **51:2**, 1055-1058 (1995).

[132] L.Monette, M.P.Anderson, and G.S.Grest, *J. Appl. Phys*, **75:2**, 1155-1170 (1994).

[133] K.A.Snyder, E.J.Garoczi, and A.R.Day, *J. Appl. Phys.*, **72:12**, 5948-5955 (1992).

[134] L.Monette and M.P.Anderson, *Scripta Metall. et Mater.*, **28:9**, 1095-1100 (1993).

[135] L.Monette, M.P.Anderson, and G.S.Grest, *J. Appl. Phys*, **75:2**, 1155-1170 (1994).

[136] M.Ostoja-Starzewski, P.Y.Sheng, and I.Jasuik, *Engng. Fract. Mech.*, **58:5-6**, 581-606 (1997).

[137] K.Alzebdeh, A.Al-Ostaz, I.Jasuik, and M.Ostoja-Starzewski, *Int. J. Solids Structures*, **35:19**, 2537-2566 (1998).

[138] L.Monette, M.P.Anderson, S.Ling, and G.S.Grest, *J. Mater. Sci*, **27**, 4393-4405 (1992).

[139] L.Monette and M.P.Anderson, *Modelling Simul. Mater. Sci. Eng*, **2**, 53-66 (1994).

[140] A.Sauron, *Computer Modelling of Crack Growth in Rubber-Toughened Polymers*, Sheffield hallam university, Ph.D. Thesis (1997).

[141] M.Ostoja-Starzewski, P.Y.Sheng, and I.Jasuik, *J. Engng. Mater. Tech.*, **116**, 384-391 (1994).

[142] Y.Mori, K.Kaneko, and M.Wadati, *J. Phys. Soc. Japan*, **60:5**, 1591-1599 (1991).

[143] P.Heino and K.Kaski, *Phys. Rev. B*, **54:9**, 6152-6154 (1996).

[144] P.K.Bannerjee and D.P.Henry, *Int. J. Solids Structures*, **29:20**, 2423-2440 (1992).

[145] T.Belytschko, Y.Y.Lu, and L.Gu, *Engng. Fract. Mech.*, **51:2**, 295-315 (1995).

[146] H.Liebowitz, J.S.Sandhu, J.D.Lee, and F.C.M.Menandro, *Engng. Fract. Mech.*, **50:5/6**, 653-670 (1995).

[147] L.D.Landau and E.M.Lifshitz, *Theory of Elasticity*, Peragmon Press (1970).

[148] J.Lemaitre and J-L.Chaboche, *Mechanics of Solid Materials*, Cambridge U.P. (1990).

[149] P.F.Thomason, *Ductile Fracture of Metals*, Pergamon Press (1990).

[150] R.D.Thompson and J.W.Hancock, *Int. J. Fracture*, **24**, 209-228 (1984).

[151] A.Ghosh, *Computers and Geoscience*, **25**, 729-738 (1999).

[152] J.A.Rice, *Mathematical Statistics and Data Analysis*, Wadsworth and Brooks/Cole. (1988).

[153] W.H.Press, B.P.Flannery, S.A.Teukolsky, and W.T.Vetterling, *Numerical Recipes in C: The Art of Scientific Computing*, Cambridge University Press (1988).

[154] A.Wald, *Sequential Analysis*, John Wiley and Sons, Inc. (1947).